Quantum Metrology of Newton's Constant with Levitated Mechanical Systems

Dissertation
der Mathematisch-Naturwissenschaftlichen Fakultät
der Eberhard Karls Universität Tübingen
zur Erlangung des Grades eines
Doktors der Naturwissenschaften
(Dr. rer. nat.)

vorgelegt von
Francis Headley
aus Chichester/Vereinigtes Königreich

Tübingen
2025

Gedruckt mit Genehmigung der Mathematisch-Naturwissenschaftlichen Fakultät der Eberhard Karls Universität Tübingen.

Tag der mündlichen Qualifikation:	14.11.2025
Dekan:	Prof. Dr. Thilo Stehle
1. Berichterstatter/-in:	Professor Daniel Braun
2. Berichterstatter/-in:	Professor Angelo Bassi

Abstract

Levitated mechanical systems are emerging as powerful tools in precision sensing and tests of fundamental physics. By trapping small particles in near vacuum using optical or superconducting techniques, these systems provide a highly stable environment that enables force sensitivities at the atto-Newton scale. Their low dissipation, long coherence times, and compatibility with quantum state preparation make them promising candidates for probing weak forces at short length scales and for testing the interface between quantum mechanics and gravitation. In particular, they have been proposed for next-generation measurements of Newton's gravitational constant G, which remains the least precisely known fundamental constant.

This thesis investigates how magnetically levitated systems in superconducting traps can be used for quantum-enhanced estimation of G, for studying gravitationally induced entanglement between mesoscopic objects, and for improving our understanding of the magnetic trapping potentials employed in these setups. We present a quantum metrological scheme in which two magnetically levitated ferromagnetic spheres oscillate harmonically in superconducting traps and interact only via their mutual gravitational potential. From the effective Hamiltonian we show that the gravitational interaction produces a phase shift in the system's normal modes, giving rise to a mechanical interferometer whose phase encodes information about G. Using tools from Gaussian quantum information, we compute both the quantum and classical Fisher information to quantify the sensitivity with which G can be estimated. We consider projective and continuous general-dyne measurement strategies and include realistic noise sources such as mechanical damping, thermal fluctuations, and Casimir interactions. Under experimentally motivated parameters, our results indicate that the relative uncertainty $\delta G/G$ can in principle be reduced by up to four orders of magnitude relative to current CODATA values, with around a two-day measurement time.

We additionally analyse entanglement generated by gravitational coupling in this system using logarithmic negativity as a quantifier, and study how gravitationally induced correlations depend on the initial Gaussian states, damping, temperature, and measurement strategy. Upper bounds on achievable entanglement are identified for coherent and squeezed initial states, and these bounds are extended to continuous measurement schemes. This analysis clarifies which regimes of gravitationally mediated entanglement are likely to be experimentally accessible in the near term and informs the feasibility of proposed tabletop probes of quantum aspects of gravity.

Finally, we derive an exact analytic expression for the magnetic potential experienced by a point dipole trapped between two infinite superconducting plates by summing an infinite series of image dipoles to satisfy the Meissner boundary conditions. The closed-form potential agrees with finite-element simulations in the near-infinite-plate geometry and provides a convenient benchmark for simulating more realistic trap geometries. The analytic potential exhibits a double-well structure that is relevant for orientational tunnelling studies and for trap design in experiments aimed at dark-matter detection, quantum tunnelling, and ultra-sensitive force sensing.

Zusammenfassung

Mechanische Systeme mit Schwebeelementen entwickeln sich zu leistungsfähigen Instrumenten für die Präzisionsmessung und für Tests in der Grundlagenphysik. Durch das Einfangen kleiner Teilchen im Vakuum mit Hilfe elektromagnetischer oder supraleitender Techniken bieten diese Systeme eine ultraisolierte Umgebung, die eine Kraftempfindlichkeit auf der Atto-Newton-Skala ermöglicht. Die geringe Verlustleistung, die langen Kohärenzzeiten und die Kompatibilität mit der Vorbereitung von Quantenzuständen machen sie zu vielversprechenden Kandidaten für die Untersuchung schwacher Kräfte - wie der Gravitation - auf kleinen Längenskalen und für die Prüfung der Schnittstelle zwischen Quantenmechanik und allgemeiner Relativitätstheorie. Insbesondere wurden sie für die nächste Generation von Messungen der Newtonschen Gravitationskonstante G vorgeschlagen, die nach wie vor die am wenigsten genau bekannte fundamentale Konstante ist.

In dieser Arbeit wird untersucht, wie magnetisch levitierte Systeme in supraleitenden Fallen zur quantengestützten Abschätzung von G, zur Untersuchung der gravitationsinduzierten Verschränkung zwischen mesoskopischen Objekten und zum besseren Verständnis der magnetischen Fallenpotentiale in diesen Anordnungen verwendet werden können. Die Arbeit gliedert sich in drei Hauptbeiträge. Erstens stellen wir ein quantenmetrologisches Schema vor, in dem zwei magnetisch levitierte ferromagnetische Kugeln in supraleitenden harmonischen Fallen oszillieren und nur über ihr gegenseitiges Gravitationspotential wechselwirken. Wir leiten den effektiven Hamiltonian ab, der das System steuert, und zeigen, wie die Gravitationswechselwirkung eine Phasendifferenz in den Normalmoden des Systems hervorruft. Unter Verwendung von Werkzeugen aus der Gaußschen Quanteninformation berechnen wir die Quanten- und klassische Fisher-Information, um die Empfindlichkeit zu quantifizieren, mit der G geschätzt werden kann. Wir betrachten sowohl projektive als auch kontinuierliche General-Dyne-Messungen, einschließlich realistischer Rauschquellen wie Dämpfung, thermische Fluktuationen und Casimir-Hintergründe. Unsere Ergebnisse zeigen, dass die relative Unsicherheit von G bei geeigneten Parametern um bis zu vier Größenordnungen gegenüber den aktuellen CODATA-Werten reduziert werden kann, und zwar innerhalb eines Tages.

Zweitens analysieren wir die Verschränkung, die in diesem System durch Gravitationskopplung erzeugt werden kann. Unter Verwendung der logarithmischen Negativität als Verschränkungsmaß untersuchen wir, wie gravitationsbedingte Korrelationen von den Gaußschen Ausgangszuständen, der Dämpfung, der Temperatur und der Messstrategie abhängen. Wir ermitteln obere Schranken für die erreichbare Verschränkung sowohl in kohärenten als auch in Squeezed-State-Protokollen, aufbauend auf früheren Ergebnissen im Bereich der gravitativen Verschränkungsbeobachtung, und erweitern diese auf kontinuierliche Messverfahren. Diese Analyse hilft zu klären, welche Regime der gravitationsvermittelten Verschränkung in naher Zukunft experimentell zugänglich sein könnten. Drittens leiten wir einen exakten analytischen Ausdruck für das magnetische Potential ab, das ein Punktdipol erfährt, der zwischen zwei unendlichen supraleitenden Platten gefangen ist. Dieses Modell umfasst eine unendliche Reihe von Bilddipolen und berücksichtigt die Meissner-Randbedingungen, wodurch eine geschlossene Lösung für die Potenziallandschaft entsteht. Wir zeigen, dass dieses Potenzial mit numerischen Ergebnissen übereinstimmt, die mit Finite-Elemente-Methoden erzielt wurden, und als Maßstab für die Simulation realistischerer Fallengeometrien dienen kann. Dieses Ergebnis ist von direkter Bedeutung für den Entwurf stabiler, symmetrischer Fallen für schwebende Magnete und lässt sich auf verschiedene vorgeschlagene Experimente zum Nachweis dunkler Materie, zum Quantentunneln und zur Kraftmessung anwenden.

Zusammengenommen zeigen diese Ergebnisse, dass magnetisch schwebende mechanische Systeme in supraleitenden Umgebungen eine praktikable und vielversprechende Plattform für quantengestützte Messungen der Schwerkraft darstellen. Sie bieten einen konkreten Weg zur Verbesserung unseres Wissens über G und tragen gleichzeitig zu den breiteren Bemühungen bei, Quantenaspekte der Schwerkraft in Tabletop-Experimenten zu erforschen.

List of publications and personal contribution

List of publications

1. Francis J. Headley, Alessio Belenchia, Mauro Paternostro, and Daniel Braun. *Quantum Metrology of Newton's constant with Levitated Mechanical Systems,* arXiv:2503.16215
2. Francis J Headley *Magnetic Dipole Trapping Potential between Infinite Superconducting Plates,* Phys. Scr. 100 085905

Personal contribution of the candidate

No.	Scientific ideas	Data generation	Analysis and interpretation	Paper writing	Status
1	50%	100%	70%	70%	In review
2	100%	100%	100%	100%	Published

Acknowledgements

A list of those to whom I owe thanks will be forever incomplete. I owe my sincerest gratitude to many whose names I forgot a very long time ago. With this in mind, I have tried my best here to mention by name those that have helped me reach this point.

There are many who cared for me during my adolescence to whom I owe my deepest thanks. The first of which being Sean McMorrow, my old physics teacher, who believed in me when I needed it the most, and for showing me gentleness when it was the thing I understood the least. I hope to one day be half the example he set for me when I was younger.

I thank the social workers from the foster home in Worthing, who took me in when I had nowhere else to go. I was very sad to leave, but was fortunate to live with Chrissy and John, my foster parents for a time, who took amazing care of me and made me feel safe and supported. I owe a tremendous debt to the support and work of Duncan Young and Jody Lomas, who treated me with kindness and dignity during one of the most difficult times of my life, helping me find stability in a very unstable world, and helping me learn to accept help when I needed it most. Without them I would've never been able to come this far. Furthermore, I would like to thank the staff of the Littlehampton food bank, for their support during the same time.

Due to the finer details of life I didn't finish secondary school, however I was glad to get the opportunity to attend Aberystwyth University with a foundation year. Without this opportunity I would have never had the ability to pursue my dreams of higher education, and I am thankful to all the staff there who supported me during my education.

The greatest blessings in my life are my friends, who have had to put up with me over all these years. First and foremost I would like to thank Ned, he is a remarkable and brilliant light shining throughout the world, constantly reminding me that the future is hopeful and that the world is, and always will be, worth being a part of. I owe a thousand thanks to Rhys, the closest thing I have to a second brother, for keeping me grounded and never letting me forget where I came from. I also thank his parents Dawn and Paul for letting me stay in the summer house. I must also extend my sincerest gratitude to my friend Joe, who taught me that not everything can be boiled down to a science, and that often times there is so much more to understanding the world than weights and measures. I must also thank his family, for their openness and support.

Keeping me sane this whole time were the Spice Boys - James, Adam, Joe R and Jamie - whose kind love and fraternity were immeasurable resources for many years. Also the Banter Squad - Isak, Jens, Lauri, Melker, and Xander - for supporting me as I turned from one type of Gravity Analyst into another. I must thank Emily, Christian, and Josh for many amazing years in the best city in the world. I could not forget to thank Ben and Jona, two of the most creative and open people I have ever met, for helping me see the world from a different viewpoint. I'd also like to thank Sophie, for all her support while I wrote this thesis and for bringing me to Germany in the first place.

From my group, I am very thankful to my supervisor Daniel Braun, for supervising me over the past three years. I am deeply indebted to Alessio Belenchia and Emre Köse, who provided me with invaluable support. Of course, I thank Jirawat, Mahdi, Fabian, Matthias H, Riccardo, Giovanni, Erik and Adriano for their camaraderie and many wonderful evenings.

I also thank the members of the Morgengang, who adopted me as one of their own. In particular I'd like to thank Wilson, Albert, Paulinho, Mathias, Francesco, Marc, Andoni, Chiara, Alba et al. I'm probably forgetting some of you, but I will never forget the time we spent with each-other.

I owe my deepest gratitude to Annika, for her kindness, companionship, and support through many wonderful years of my life. She knows very well that I would never have gotten this far without her.

From my family, I owe so much to the endless love from my sister Jess, whose joy and positivity I could not live without. Not a day goes by where I don't think about my late Grandad, whose unconditional support and advice allowed me to achieve all that I have.

But above all, I thank my brother Charlie.

Contents

1 Introduction 1

2 Overview of Set-up 7

3 Quantum Parameter Estimation 13

3.1 Classical Estimation Theory 13

3.2 Quantum Estimation Theory 17

4 Gaussian States and Evolution 20

4.1 Gaussian States 20

4.2 General Evolution 23

4.3 Quantum Fisher Information - Covariance Matrix Formulation 25

4.4 Fisher information for time-continuous measurements 27

4.5 Logarithmic Negativity 29

5 The Meissner Effect and Magnetic Trapping 32

5.1 The Meissner Effect 32

5.2 Image Dipoles and Trapping Potentials 33

5.3 Finite element method 36

6 Results 40

6.1 Analytic trapping potential 41

6.2 Quantum Fisher Information - Projective measurements 44

6.3 Quantum Fisher Information - Continuous measurements 50

6.4 Additional Sources of Noise 51

6.5 Entanglement Generation 53

7 Conclusion and Outlook 58

Appendix: publications 61

7.1 First publication 61

7.2 Second publication 72

Bibliography 86

Chapter 1

Introduction

Despite our best intentions, we still do not understand the nature and origin of the gravitational force. In the 16th century, Galileo Galilei showed that, when friction and air resistance are taken into account, all objects experience the same gravitational acceleration. This finding, which had remained remarkably untested up until then, challenged prevailing Aristotelian view on the nature of falling masses and laid a foundational principle for classical mechanics. Around the same time, Johannes Kepler, building on the precise astronomical observations of Tycho Brahe, composed three laws which described the elliptical orbits of planets and provided a framework for understanding celestial mechanics. Kepler's laws offered a critical empirical foundation, enabling a shift from geocentric models to a heliocentric understanding of the solar system. On the 5th of July 1687 Isaac Newton published his work in which he generalised Kepler's laws of planetary motion in the *Law of Universal Gravitation* [1]. Newton's formulation posited that every pair of massive objects attract each other with a force proportional to the product of their masses and inversely proportional to the square of the distance between their centres of mass.

$$F = G\frac{m_1 m_2}{r^2} \tag{1.1}$$

where m_1 and m_2 are the masses of the two objects and r is the distance between the two objects centres of mass. The constant of proportionality in this expression G, which we refer to as Newton's constant [1]. It's approximately $G = 6.67 \times 10^{-11}\,\mathrm{m}^3\,\mathrm{kg}^{-1}\,\mathrm{s}^{-2}$. It is

---

[1] Or 'Big G' to its friends.

important to note, this is outstandingly small among physical constants. Indeed, gravity is the weakest of the fundamental forces, being approximately 10^{36} times weaker than the electromagnetic force. This extreme weakness poses significant challenges for experimental studies, as gravitational effects are often overshadowed by other fundamental interactions. As such, exact measurement of the gravitational constant has proven to be of exceeding difficulty. The first known successful attempt at a measurement of gravity was conducted in 1797 by Henry Cavendish [2]. Cavendish's experiment involved suspending lead spheres on rods on a fine wire, suspended from the ceiling of his shed. He measured the minute angular deflection in the wire which was caused by the gravitational attraction between the spheres and two additional masses. The intent of the experiment was to 'weigh the world', where he sought to estimate the relative density of the earth with some reasonable precision. Whilst he achieved this to incredible accuracy, measuring the density of the earth to be $5.48\,\mathrm{g/cm^3}$, with current accepted value $5.514\,\mathrm{g/cm^3}$, he had also inadvertently measured Newton's constant. By reformulating his findings, it can be found that he measured Newton's constant to be $G = 6.674 \times 10^{-11}\,\mathrm{m^3\,kg^{-1}\,s^{-2}}$, which differs by less than 1% from the current standard value of CODATA [3]

$$G = 6.67430 \times 10^{-11}\,\mathrm{m^3\,kg^{-1}\,s^{-2}} \tag{1.2}$$

where the CODATA relative standard uncertainty is $\delta G/G = 2.2 \times 10^{-5}$. This remarkable precision, achieved with 18th-century technology, underscores the ingenuity of Cavendish's approach, yet modern experiments continue to grapple with similar challenges in improving accuracy.

Due to the weakness of the gravitational force, improving our knowledge of the exact value of G requires significant improvement in the sensitivity of our experimental set-ups. The challenge of measuring G is persistent even to this day, as evidenced by discrepancies [4]. Indeed, even though the *precision* of our measurements is increasing, the experimentally measured values of G do not seem to be converging to the same value [4,5]. Such inconsistencies suggest potential systematic effects, or undiscovered aspects of gravitational interactions, which are present in modern experimental set-ups, which we are as of yet unable to account for. These challenges motivate the ongoing research into novel measurement techniques that can mitigate environmental noise and systematic errors, potentially revealing new insights into gravitational physics.

There are several hurdles which appear when trying to measure Newton's constant. In particular, unlike the electromagnetic force, there is no known way to shield an experiment from an external gravitational fields. In principle, one must always have to account for the building which the experiment is conducted in, the space time curvature of bodies which surround the experimental set-up, or the gravitational field of the bus that drives past the building every morning. Furthermore, the mass of the objects we need to use to measure gravity are, in general, very large and in themselves have a significant uncertainty in the mass. These challenges necessitate advanced techniques for isolating gravitational signals, such as ultra-low noise environments and precise mass calibration methods. One such solution to these static effects is to try to convert the gravitational effect into a dynamical signal which we can observe, such as the phase accumulated by oscillating test masses, which allow for measurement set-ups which can suppress additional static noise sources.

Noting the difficulty in measuring a gravitational signal, it is also important to highlight gravity's unique status among the fundamental forces: unlike electromagnetism, as well as the strong and weak nuclear forces, each well-described by quantum theory, gravity's quantum nature is still unknown. Indeed one of the longest standing questions in theoretical physics is on the quantisation of gravity, whilst it is possible to formulate a somewhat satisfactory theory of quantum gravity by linearising the field in QFT, yielding a massless spin 2 field [6], this theory does not hold up for larger curvatures and direct observation of a hypothetical "graviton" would require particle accelerators far beyond current technological capabilities [7]. Consequently, alternative experimental paradigms are needed to probe the quantum aspects of gravity.

One of the earliest conceptual arguments for the necessity of quantising gravity was given by Feynman at the 1957 Chapel Hill Conference on the Role of Gravitation in Physics [8]. He considered a thought experiment in which a particle is placed in a spatial superposition and allowed to interact gravitationally with a nearby test mass. If gravity were fundamentally classical, the gravitational field would not become entangled with the particle's position, and the system would evolve inconsistently with the predictions of quantum mechanics. To preserve unitarity and the validity of quantum superposition, Feynman concluded that gravity must itself be capable of existing in a quantum superposition — i.e. it must be a quantum field. This idea, though qualitative, laid the conceptual foundation for modern proposals which aim to test whether gravity can act as a quantum mediator by observing entanglement generation between spatially separated masses.

One notable proposal, the Bose-Marston-Vedral (BMV) experiment [9, 10] suggests testing quantum gravity through entanglement generated by gravitational interactions between quantum systems. In the proposed experiment, two particles are placed in spatial superpositions, and the gravitational field induces a relative phase shift that can generate entanglement. Detecting this entanglement serves as indirect evidence for the quantisation of gravity. Since entanglement cannot be created via local operations and classical communication (LOCC), its observation implies that gravity must transmit quantum information. Such approaches motivate the development of novel experimental platforms, such as levitated mechanical systems, which offer high sensitivity and isolation from environmental noise [11–15]. In the past few years these levitated mechanical systems, (e.g. particles suspended in electromagnetic, optical, or acoustic fields) have been suggested as a promising experimental platform which can address some of these challenges [11,16–23]. In particular, magnetic levitation has been seen to offer unprecedented isolation from non-gravitational environmental disturbances [17] as well as long-lived coherent oscillations, [12–14], these properties are essential for stable experimental setups which are capable of high-precision measurements [24, 25]. These set-ups have been shown to achieve atto-newton force measurements [13]. Moreover, as magnetic levitation allows for stable trapping of Planck-scale masses, this suggests that this platform may be able to perform high-precision measurements of the gravitational field at sub-millimetric distances and, perhaps in the future, the detection of the gravitational field of quantum sources [21, 25–27]. This is the primary motivation of this work, while other non-levitated mesoscopic tests of gravity [25] have shown coupling of masses of the order of milligrams, it does not seem possible to use such a set-up to create a *quantum* source of gravity, as levitated magnets are purported to have low decoherence rates and high coherence times, they seem a likely candidate to generate such phenomena on a measurable energy scale to probe the quantum nature of gravity. The potential of these systems to probe quantum gravity underscores their importance in addressing fundamental questions about the nature of spacetime and its interaction with quantum systems.

In this work, we develop and analyse a quantum-metrological framework for measuring Newton's gravitational constant G using two magnetically levitated dipoles in superconducting traps, coupled via their mutual gravitational interaction. Utilising techniques from quantum optics, condensed-matter physics, and quantum metrology, we show that, under realistic conditions including damping, thermal fluctuations, and Casimir effects [28], the achievable relative uncertainty $\delta G/G$ can in principle surpass current CODATA values by four orders of magnitude within a measurement time of approximately one day. In addition, we quantify the maximum gravitationally mediated entanglement attainable in this system, extending the work of Krisnanda *et al.* [29] to include damping effects and optimisation over Gaussian input states. Finally, we derive and validate an analytic expression for the magnetic trapping potential of a dipole between superconducting plates [30], providing a benchmark for future experiments and simulations relevant to quantum tunnelling, ultrasensitive force sensing [13–15], dark-matter detection [31, 32], and fundamental tests of quantum mechanics [18, 32].

We position magnetically levitated mechanical systems as a unified platform for both quantum-enhanced gravitational metrology and the study of gravity-induced quantum correlations. By combining a Gaussian-state Quantum Fisher Information analysis tailored to a realistic superconducting-trap architecture with a quantitative comparison of experimentally accessible measurement schemes, we establish concrete sensitivity benchmarks for G-measurement protocols. In parallel, we extend the same formalism to predict entanglement generation under gravitational coupling, thereby linking precision metrology and quantum-gravity tests within a single theoretical framework. Supporting these analyses is the closed-form derivation of the magnetic trapping potential for a dipole between superconducting plates, validated with finite-element simulations, which provides a reusable modelling tool for levitated-sensor design. Together, these results set experimentally relevant targets, supply analytic resources, and clarify the trade-offs that will define the near-term prospects for probing gravity with mesoscopic quantum systems.

This thesis makes three primary contributions. First, it introduces and analyses a quantum-metrological protocol for estimating G using two magnetically levitated oscillators in a superconducting trap, deriving the effective quadratic Hamiltonian and computing the Quantum Fisher Information for the interferometric phase that encodes G. Second, it evaluates measurement strategies and practical limitations, comparing projective and continuous general-dyne measurements, quantifying the effects of dissipation, thermal noise, and measurement back-action, and identifying which realistic schemes can approach the quantum Cramér–Rao bound. Third, it provides supporting modelling by deriving an exact analytic magnetic trapping potential for a dipole between superconducting plates and validating it against finite-element simulations. The thesis is organised as follows. Chapter 2 introduces the physical set-up and derives the coupled-oscillator Hamiltonian and explains the parameter set which was used in the numerics. Chapter 3 reviews classical and quantum estimation theory and presents the covariance-matrix formalism for computing the QFI. Chapter 4 applies this formalism to the levitated interferometer, deriving analytic QFI expressions and analysing the influence of squeezing and measurement choice. Chapter 5 outlines the derivation and validation of the magnetic trapping potential. Chapter 6 compiles the main results: the analytic trapping potential, its numerical validation, sensitivity estimates, measurement comparisons and entanglement analysis. Chapter 7 summarises the findings and outlines future directions.

Chapter 2

Overview of Set-up

In this chapter we present the model which was used in Manuscript 7.1 to probe the sensitivity of gravitationally coupled levitated magnets in measuring Newton's constants. This approach builds on recent proposals for using magnetically levitated systems to probe gravitational interactions in a mesoscopic mass regime [11, 13, 17, 33, 34]. The set-up consists of two magnets levitated in superconducting traps, coupled solely through their non-relativistic gravitational potential, which can be modelled in such a way that their evolution remains Gaussian. To begin, each uncoupled levitated magnet is treated as a one-dimensional harmonic oscillator with free Hamiltonian

$$H_0 = \sum_{i=1,2} \left(\frac{p_i^2}{2m} + \frac{1}{2} m \omega_0^2 x_i^2 \right) . \tag{2.1}$$

In what follows, we take both oscillators to have the same mass m and trapping frequency ω_0. In general, the trapping frequency will depend on the geometry of the trap and the parameters governing the magnet itself, for example the width of the trap and the magnetisation of the particle. We assume that the superconducting traps are shielded from each-other in some way, for example with a Faraday shield, such that the oscillators can only interact via the gravitational field. For the non-relativistic regime, the interaction between two masses m with distance r between their centres of mass can be expressed as

$$U(r) = -G \frac{m^2}{r} , \tag{2.2}$$

where G denotes Newton's constant. The assumption that the oscillators are harmonic oscillators, that is to say that the potential does not contain any higher order terms, is valid only as long as the oscillatory amplitudes x_1, x_2 of the particles about their equilibrium positions is indeed small compared to the separation of equilibrium positions d, as well as the trap width. Writing $r = |d - x_1 + x_2|$ and expanding to quadratic order in $x_1, x_2 \ll d$, the gravitational potential can be expressed

$$H_G = -\frac{Gm^2}{d}\left(1 + \frac{(x_1 - x_2)}{d} + \frac{(x_1 - x_2)^2}{d^2} + \dots\right). \tag{2.3}$$

As is typical x_i, p_i can be rewritten in terms f the oscillator length, $x_i \to \sqrt{\hbar/m\omega_0}x_i$, $p_i \to \sqrt{\hbar m\omega_0}p_i$, such that they are dimensionless. We have expanded the potential to quadratic order (that is to say, the Hamiltonian is Gaussian) due to the fact that in practical experiments, levitated particles are harmonically trapped - provided that the oscillatory amplitudes remain small enough to avoid non-linearities in the trapping potential. Because of this the dynamics of the system remain analytically solvable and remain Gaussian throughout. The details of Gaussian states evolution will be explored more in Section 3. The full Hamiltonian is then

$$H/\hbar = \sum_{i=1,2}\frac{1}{2}\omega_0\left(p_i^2 + \left(1 - \frac{2Gm}{d^3\omega_0^2}\right)x_i^2\right) + \frac{Gm^2}{\sqrt{d^4\hbar m\omega_0}}(x_2 - x_1) + \frac{2Gm}{d^3\omega_0}x_1x_2. \tag{2.4}$$

We see that the gravitational potential (2.3) introduces a shift in the oscillatory frequencies, a linear shift in the equilibrium positions, and the final term in (2.4) couples the modes. To deal with this coupling term, we translate our Hamiltonian (2.4) into the normal mode coordinate basis

$$x_\pm = \frac{1}{\sqrt{2}}(x_2 \pm x_1), \qquad p_\pm = \frac{1}{\sqrt{2}}(p_2 \pm p_1). \tag{2.5}$$

with corresponding creation and annihilation operators

$$a_\pm = \frac{1}{\sqrt{2}}(x_\pm + ip_\pm). \tag{2.6}$$

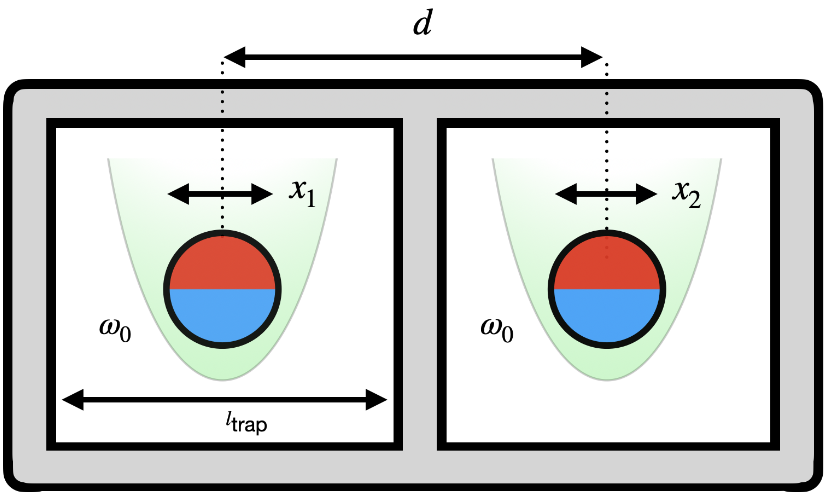

Figure 2.1: Sketch of the set-up: Two masses m, separated by a distance d and coupled solely via their mutual gravitational attraction, are confined in harmonic potentials of frequency ω_0. Such traps may, for instance, be realised by levitating small ferromagnetic particles inside superconducting boxes. The coordinates $x_{1,2}$ denote the displacements of each mass from its equilibrium position.

The position and momentum operators appearing in Eq. (2.4) can be written in terms of the corresponding creation and annihilation operators using the standard expressions:

$$x_\pm = \frac{1}{\sqrt{2}}(a_\pm + a_\pm^\dagger), \quad p_\pm = -\frac{i}{\sqrt{2}}(a_\pm - a_\pm^\dagger). \tag{2.7}$$

Rewriting the Hamiltonian (2.4) in this normal mode basis, we see that the Hamiltonian diagonalises, where only a linear term which remains:

$$H/\hbar = \frac{1}{2}\omega_0(p_+^2 + x_+^2 + p_-^2 + (1-2\eta)x_-^2) + \sqrt{2}\nu x_-, \tag{2.8}$$

where we have introduced the constants $\eta = 2Gm/d^3\omega_0^2$ and $\nu = Gm^2/\sqrt{\hbar m\omega_0 d^4}$. We note here that both η and ν encode information about G into the state as it evolves. By rewriting Eq.(2.8) in terms of the creation and annihilation operators associated with the normal modes, as defined in Eq. (2.7), we obtain

$$H/\hbar = \frac{1}{2}\omega_0\Big[(a_+^\dagger a_+ + a_+ a_+^\dagger) + (1-\eta)(a_-^\dagger a_- + a_- a_-^\dagger) - \eta(a_-^2 + (a_-^\dagger)^2)\Big] + \nu(a_- + a_-^\dagger). \tag{2.9}$$

We assume that the gravitational interaction is sufficiently weak, i.e. $Gm/(d^3\omega^2) \ll 1$, an assumption that will be substantiated later using realistic parameter choices. Under this condition, one may neglect the a^2 and $(a^\dagger)^2$ contributions. Moving to the corotating frame reveals that these terms oscillate rapidly and thus have negligible influence on the dynamics. This approximation is further supported *a posteriori* through comparison with the exact quantum Fisher information, as discussed in Manuscript 7.1. Implementing this simplification yields the Hamiltonian:

$$H/\hbar \approx \omega_0 a_+^\dagger a_+ + \omega_0(1-\eta)a_-^\dagger a_- + \nu(a_- + a_-^\dagger). \tag{2.10}$$

We note, however, that the shift in the equilibrium position of the centres of motion of each particle present in (2.4) is difficult to measure directly, as to measure this requires access to the uncoupled modes. As we are unable to shield gravitational interaction between the oscillators, we are only able to study the evolution of the modes when they are already coupled via their gravitational interaction. As such we disregard this term. Doing so means we neglect the term in (2.10) linear in ν, which originates from the linear shift. The resulting Hamiltonian is then

$$H/\hbar \simeq \omega_0 a_+^\dagger a_+ + \omega_0(1-\eta)a_-^\dagger a_- \,. \tag{2.11}$$

Here we see that all of the accessible information about G is encoded in the evolution of the a_- mode. In Manuscript 7.1, we studied the dynamics and sensitivity of this set-up in the measurement of G. In said work, we noted that the Hamiltonian (2.11) allows us to treat the system as being analogous to a mechanical beam-splitter, whereby the information about the parameter we wish to estimate is encoded onto one arm of the evolution. This analogy to a beam-splitter highlights the interferometric nature of the setup, where the gravitational interaction induces a measurable phase difference between the normal modes. To justify this, we note that since the Hamiltonian (2.11) is only quadratic in the quadratures, the Gaussianity of the evolution is preserved. Starting from an initial state prepared at $t = 0$, the two harmonic oscillators evolve within their respective traps, interacting exclusively through their mutual gravitational potential. Changing basis from the $a_{1,2}$ operators to the $a_\pm$ combinations is equivalent to applying a beam-splitter transformation, such that a_+ and a_- represent the two interferometer arms. In this picture, we see that only the a_- mode acquires a G-dependent phase. At the final time $t = t_f$, the interferometer is 'closed' by carrying out local projective Gaussian measurements on the physical oscillator modes $a_{1,2}$. This set-up, wherein two freely evolving modes with a G-dependent phase shift between them, contrasts with conventional approaches in which a test mass evolves freely while the source mass is either driven [35, 36] or displaced by external forces [2, 37]. This interferometric approach enhances sensitivity by exploiting the relative phase evolution between the two modes, offering a distinct advantage over traditional gravitational measurement techniques.

Parameters

To evaluate the sensitivity of the proposed interferometric scheme for estimating Newton's constant G, we adopt a set of experimentally motivated parameters based on current capabilities in levitated mechanics and superconducting trap design.

Name	**Symbol**	**Value**
Mass of each particle	m	$1 \times 10^{-4}\,\mathrm{kg}$
Particle density	ϱ	$7430\,\mathrm{kg/m^3}$
Trap frequency	ω_0	$100\,\mathrm{rad/s}$
Trap width	l_{trap}	$4.9 \times 10^{-3}\,\mathrm{m}$
Centre-of-mass separation	d	$5.0 \times 10^{-3}\,\mathrm{m}$
Coherent amplitude	α_1	3.374×10^{12}
Squeezing parameter	s	$[-1.8, 1.8]$
Thermal occupation number	$\bar{n}$	Variable (e.g., $\bar{n} = 0 - 1\,\mathrm{mK}$)
Quality factor	Q	$10^5 - 10^7$
Gravitational coupling	η	1.068×10^{-11}

Table 2.1: Summary of physical parameters used in the estimation protocol.

The system consists of two identical spherical test masses, where the choice of identical masses simplifies the theoretical analysis and ensures symmetry in the gravitational interaction. In the case of a levitated magnet in a superconducting trap, the most commonly used magnetic material is Neodymium, with a density of $\varrho = 7430\,\mathrm{kg\ m^{-3}}$ and an remnant magnetisation in the range of $R_m = 1 - 1.4\,\mathrm{T}$. Each magnet has a radius of approximately $r = 1.48\,\mathrm{mm}$, giving a mass of $m = 1 \times 10^{-4}\,\mathrm{kg}$. Both particles are harmonically trapped with equal frequencies, set to $\omega_0 = 100\,\mathrm{rad/s}$, a value within the experimentally accessible range for magnetically levitated particles [11–15]. These magnets are normally levitated in lead or tantalum traps, which are generally of order of millimetres in scale. The trap size is taken to be $l_{\mathrm{trap}} = 4.9 \times 10^{-3}\,\mathrm{m}$, with a centre-of-mass separation between the oscillators of $d = 5.0 \times 10^{-3}\,\mathrm{m}$. This configuration allows for gravitational coupling while remaining within the harmonic approximation. To initialise the system, we use coherent, thermal, and squeezed Gaussian states. The initial displacement of the first oscillator is set to $\langle x_1(0)\rangle = l_{\mathrm{trap}}/10$, corresponding to a dimensionless coherent amplitude $\alpha_1 \approx 3.374 \times 10^{12}$. This choice ensures the gravitational potential can be accurately expanded to second order in position, with higher-order terms contributing less than 0.1% . We explore squeezing of the first mode with a squeezing parameter $s \in [-1.8, 1.8]$, equivalent to roughly $\pm 15\,\mathrm{dB}$, which is approximately the current record for squeezing [38,39]. Squeezing in the momentum or position quadrature has opposite effects on sensitivity depending on the initial state orientation, as demonstrated in Manuscript 7.1. The thermal temperature of the system is expressed via a thermal occupation number $\bar{n} = \left(\exp\left[\hbar\omega_0/k_B T\right] - 1\right)^{-1}$. We will see that sensitivity degrades with increasing temperature. Damping is introduced via a phenomenological quality factor $Q = \omega_0/\gamma$, with realistic values in the range $Q = 10^5$ to $Q = 10^7$. High quality factors are essential for maintaining long coherence times, which are necessary for precise phase measurements in the interferometric setup, and the chosen values reflect currently achievable coherence times in superconducting magnetic traps [12, 13]. The gravitational coupling strength for these parameters $\eta = \frac{2Gm}{d^3\omega_0^2} \approx 1.068 \times 10^{-11}$. For a trap size $l_{\mathrm{trap}} = 4.9 \times 10^{-3}$ m, and initial displacement $\langle x_1(0)\rangle = l_{\mathrm{trap}}/10$, the coherent amplitude is

$$\alpha_1 = \sqrt{\frac{m\omega_0}{2\hbar}}\langle x_1(0)\rangle \approx 3.374 \times 10^{12}, \tag{2.12}$$

with $m = 10^{-4}$ kg, $d = 5 \times 10^{-3}$ m, and $\omega_0 = 100$ rad/s, the gravitational coupling is $\eta = 1.068 \times 10^{-11}$. A summary of these parameters can be seen in Table 2.1.

Chapter 3

Quantum Parameter Estimation

In this chapter, we introduce the foundational concepts of estimation theory that will underpin the analysis of sensitivity in levitated quantum systems used to probe the gravitational constant G. We begin by reviewing the classical Fisher information, which quantifies the amount accessible information that probability distribution contains about a parameter. This framework provides a natural bound on the precision of unbiased estimators through the classical Cramér–Rao inequality. We then extend this framework into the quantum regime, introducing the quantum Fisher information, which generalizes the classical notion by accounting for the full statistical structure of quantum states. The QFI sets the ultimate precision limit achievable in parameter estimation, as governed by the quantum Cramér–Rao bound, and plays a central role in identifying optimal measurements and probe states. These tools will later be applied to analyse the sensitivity of quantum optomechanical systems, specifically levitated nanoparticles, as potential probes for detecting weak gravitational interactions.

3.1 Classical Estimation Theory

The natural sciences are predicated on our ability to predict and measure physical phenomena. One could argue that the ability to estimate the likelihood of future events is what has defined the success in the human species. This interdependency of statistics and inference have a tremendous effect on our lives, and although in modern times we see the realization of these statistics in more frivolous endeavours such as stock market predictions or better yet, slot machines, the presence of statistics and the parameters upon which they depend are an integral part of the natural world.

A fundamental object in probability theory is the probability distribution, which is a function which the describes the probabilities of a set of events which exist in a sample space. To define this we must first define a random variable X, which is a map from the sample space Ω to the real numbers $X : \Omega \to \mathbb{R}$. In the case where out the possible outcomes are discrete, such as in a coin flip or a dice roll, the random variable takes X takes on certain values (e.g. $X \in [1, 2, 3, 4, 5, 6]$ in a dice roll). The probabilities of such outcomes are described by the probability mass function

$$\mathbb{P}(X = x_i) \in [0, 1], \quad \sum_i P(X = x_i) = 1 \tag{3.1}$$

where the sum runs over all possible values of x_i. Each probability $p(x_i)$ simply gives the probability of observing $X = x_i$. The expectation value (or mean) of the random variable X is:

$$\mathbb{E}[X] = \sum_i x_i p(x_i), \tag{3.2}$$

and the variance, which quantifies the uncertainty in X is given by

$$\mathrm{Var}[X] = \sum_i (x_i - \mathbb{E}[X])^2 p(x_i). \tag{3.3}$$

In the case where we instead have a continuous continuous random variable X The probability that $X \in [a, b]$ is given by the integral over the probability density function (PDF):

$$\mathbb{P}(a \leq X \leq b) = \int_a^b dx\, p(x), \qquad \int_{-\infty}^{\infty} dx\, p(x) = 1. \tag{3.4}$$

We define the expectation value of the random variable in a similar way to the discrete case:

$$\mathbb{E}[X] = \int_{-\infty}^{\infty} dx\, x\, p(x) \tag{3.5}$$

furthermore the variance of is given by:

$$\mathrm{Var}[X] = \int_{-\infty}^{\infty} dx\, (x - \mathbb{E}[X])^2 p(x) \tag{3.6}$$

We often refer to the probability density function as the probability distribution, and will do so throughout this text. One such example of a distribution, and one of utmost importance in physics, is the Gaussian distribution (also called the Normal distribution):

$$p(x) = \frac{1}{\sqrt{2\pi\sigma^2}} e^{-\frac{(x-\mu)^2}{2\sigma^2}} \tag{3.7}$$

where it can be easily shown that μ is the expectation value of the distribution, and σ^2 is the variance.

Suppose that the outcomes of our random variable depend on a parameter θ, then our probability distribution picks up a parameter dependence, we write our θ-dependent probability as $p_\theta(x) = p(x|\theta)$, where (3.4) still applies. In general θ can be a vector consisting of any number of parameters, upon which out distribution can depend. It must be noted that in general, the probability distribution function can depend on multiple parameters, however in this text we only treat the single parameter case.

With all this in consideration, a natural question arises: Say we perform an experiment, the outcomes of which are collected in a statistical sample $x = (x_1, x_2, \ldots, x_n)$, assuming that we already know which type of probability distribution best fits our experiment and that the results of this experiment depend on a parameter θ, how well can we estimate θ from our results? To begin answering this question, we define an estimator $\hat{\theta}(x)$ which depends on the results of our experiment. An unbiased estimator is defined in the following way:

$$\mathbb{E}_\theta[\hat{\theta}(x)] \equiv \int_{\mathbb{R}} dx\, \hat{\theta}(x)\, p_\theta(x) = \theta \tag{3.8}$$

such that its expectation value is the true value of the parameter we wish to estimate. If this condition does not hold, then the estimator is said to be *biased*, where the bias is defined accordingly

$$b(\theta) = \mathbb{E}_\theta[\hat{\theta}] - \theta \tag{3.9}$$

In general, we work with unbiased estimators. A useful method of determining the precision of an estimator is the mean square error, which we can try to minimise:

$$\mathrm{MSE}[\hat{\theta}] = \mathbb{E}_\theta[(\hat{\theta} - \theta)^2] \tag{3.10}$$

Expanding the above, we may express the MSE as the sum of the variance and square of the bias:

$$\mathrm{MSE}[\hat{\theta}] = \mathrm{Var}_\theta[\hat{\theta}] + b(\theta)^2 \tag{3.11}$$

when considering an unbiased estimator the standard deviation (which we often refer to as the sensitivity of the estimator) is simply the square root of the variance:

$$\delta\theta = \sqrt{\mathrm{Var}_\theta[\hat{\theta}]} \tag{3.12}$$

The primary goal of parameter estimation is to construct the optimal estimator, such that $\delta\theta$ is as small as possible, meaning that the value of our estimator is close to the actual value of the parameter. It should be noted that, in general, such an estimator that minimises the variance for all θ does not necessarily exist [40]. In the following, we will consider only the maximum likelihood estimator, and use it to construct the Cramér-Rao bound. For a given parameter dependent probability distribution function $p_\theta(x)$, the likelihood function is given by

$$\mathcal{L}(\theta) = \mathcal{L}(\theta|x) = p_\theta(x) \tag{3.13}$$

We note here that the likelihood function $\mathcal{L}(\theta|x)$ is a function of θ, where we consider the statistical sample x to be fixed. If θ were to be fixed to some value, then it is the probability density function. It is often much simpler to work with the loglikelihood function,

$$l(\theta|x) = \ln \mathcal{L}(\theta|x), \tag{3.14}$$

where it is important note that since the logarithm is a monotonously increasing function, the loglikelihood is maximised at the same value of parameter as the likelihood. The MLE is simply the estimator that maximises the loglikelihood function:

$$\hat{\theta}_{\mathrm{MLE}} = \underset{\theta\in\Theta}{\mathrm{argmax}}\, l(\theta|x) \tag{3.15}$$

The derivative of the log-likelihood function with respect to the parameter is called the *score*. If θ is the true parameter, then the expectation value of the score is zero.

$$\mathbb{E}_\theta\left[\partial_\theta l(\theta|x)\right] = \int_{\mathbb{R}} dx \left[\frac{1}{p_\theta(x)}\frac{\partial p_\theta(x)}{\partial\theta}\right] p_\theta(x) \tag{3.16}$$

$$= \int_{\mathbb{R}} dx \, \frac{\partial p_\theta(x)}{\partial\theta} \tag{3.17}$$

$$= \frac{\partial}{\partial\theta}\int_{\mathbb{R}} dx \, p_\theta(x) = \frac{\partial}{\partial\theta}1 = 0 \tag{3.18}$$

The Fisher Information is then defined to be the variance of the score:

$$F_c(\theta) = \int_{\mathbb{R}} dx p_\theta(x)\left(\frac{\partial \ln p_\theta(x)}{\partial\theta}\right)^2, \tag{3.19}$$

where we note that $F(\theta) \geq 0$. We often call this the *classical Fisher information* (CFI), which associated to the probability density function $p_\theta(x)$. The Cramér–Rao bound states that the standard deviation $\delta\hat{\theta} = \sqrt{\mathrm{Var}(\hat{\theta})}$ of any unbiased estimator $\hat{\theta}$ is bounded from below by the inverse square root of the Fisher information:

$$\delta\theta \geq \frac{1}{\sqrt{Q\, F_c(\theta)}} \tag{3.20}$$

where Q is the number of performed experiments. The classical Fisher information quantifies the amount of information that the probability distribution function of a random variable carries about an unknown parameter in a statistical model, serving as a measure of the precision with which the parameter can be estimated.

3.2 Quantum Estimation Theory

While classical estimation theory provides a powerful framework for quantifying the precision limits of parameter inference based on probabilistic measurement outcomes, it assumes that the underlying probability distribution is fixed and independent of the act of measurement. In quantum mechanics, however, the situation is fundamentally different: the probability distributions themselves arise from measurements performed on quantum states, which may be altered or disturbed by the measurement process. In particular, when the parameter of interest θ is encoded in a quantum state ρ_θ, the achievable precision in estimating θ depends both on the choice of measurement (i.e., the measurement operators) and the quantum properties of the state. This necessitates a generalisation of the classical Cramér–Rao bound to the realm of quantum systems, where one seeks to identify the ultimate lower bound on the estimation error over all possible measurements allowed by quantum mechanics. This forms the basis of quantum estimation theory, which we now outline. As discussed in the previous section, in classical estimation theory, the inverse of the Fisher information

$$F_c(\theta) = \int_{\mathbb{R}} dx p_\theta(x) \left(\frac{\partial \ln p_\theta(x)}{\partial \theta} \right)^2, \tag{3.21}$$

which bounds from below the mean square error of any (unbiased) estimator of a given parameter θ encoded in a probability distribution $p_\theta(x)$ of a random variable x. This inequality is the (classical) Cramér–Rao bound (CRB) [41, 42]. In the quantum setting the unknown parameter θ is encoded in the system state via the density operator ρ_θ, while x denotes the random outcome of a measurement described by POVM elements $\{\Pi_x\}$. The outcome probabilities are therefore

$$p_\theta(x) = \mathrm{Tr}[\Pi_x \rho_\theta] \tag{3.22}$$

where the operator Π_x is an element of a set of positive operator-valued measurements (POVM) corresponding to the outcome x.

$$\Pi_x \geq 0 \quad \forall x, \quad \sum_x \Pi_i = 1. \tag{3.23}$$

Maximizing over the set of all possible POVMs yields an upper bound for the classical Fisher information,

$$F_c \leq F_q := \mathrm{tr} \rho_\theta L_\theta^2, \tag{3.24}$$

where the symmetric logarithmic derivative L_θ is introduced through the relation $\partial_\theta \rho_\theta = (L_\theta \rho_\theta + \rho_\theta L_\theta)/2$. We call F_q the quantum Fisher information (QFI). The quantum Cramér–Rao bound (QCRB) [43–45] then provides a lower bound on the achievable standard deviation of any unbiased estimator for θ.

$$\delta\theta \geq \frac{1}{\sqrt{QF_c(\rho_\theta)}} \geq \frac{1}{\sqrt{QF_q(\rho_\theta)}}\,, \tag{3.25}$$

where Q is the number of performed experiments. The measurement that achieves equality in the QCRB is a projective measurement whose POVM elements correspond to projectors onto the eigen-basis of L_θ. In practice, however, such measurements may not be experimentally feasible. Finding the optimal measurements which saturate this bound is often a non-trivial task, however the bound itself serves to inform us about the maximum possible sensitivity of a given experimental set-up, and gives us insight into the viability of certain set-ups in sensing and parameter estimation.

Chapter 4

Gaussian States and Evolution

In this section[1] we lay out the framework of the Gaussian evolution of the system of coupled oscillators [46]. Gaussian quantum states are central to continuous-variable quantum systems, providing a framework to describe systems like coupled oscillators and optical fields. Defined by their first moments and covariance matrices, these states enable a concise representation of quantum dynamics under linear and quadratic Hamiltonians. This chapter outlines the formalism of Gaussian states, including their symplectic structure and Wigner function representation. We present the evolution of first moments and covariance matrices for coupled oscillators, incorporating damping and noise effects in the context of our system. The analysis extends to quantum Fisher information for parameter estimation and stochastic dynamics under continuous general-dyne measurements, relevant to experimental setups like SQUID-based detection.

4.1 Gaussian States

In the continuous variable formalism, the dimensionless quadrature variables are promoted to operators $\hat{x}_i$ and $\hat{p}_i$ for $i = 1, \dots, n$. Grouping these into the column vector $\hat{\mathbf{r}} = (\hat{x}_1, \hat{p}_1, \dots, \hat{x}_n, \hat{p}_n)^T$, the canonical commutation relations take the compact form

$$[\hat{r}_i, \hat{r}_j] = i\Omega_{ij}, \tag{4.1}$$

---

[1] Not to be confused with the 1917 text ”The State and Revolution” by Vladimir Lenin.

with $i, j = 1, \ldots, 2n$ and Ω denoting the symplectic form. The symplectic form is conventionally written as

$$\Omega = \bigoplus_{j=1}^{n} \omega, \quad \text{where} \quad \omega = \begin{pmatrix} 0 & 1 \\ -1 & 0 \end{pmatrix}. \tag{4.2}$$

The structure of Ω follows directly from the canonical relations $[\hat{x}_i, \hat{p}j] = i\delta_{ij}$. Hamiltonians that preserve Gaussianity are at most quadratic in the canonical operators [47]. The general form for such a Hamiltonian can be expressed as

$$\hat{H} = \frac{1}{2}\hat{\mathbf{r}}^T H \hat{\mathbf{r}} + \hat{\mathbf{r}}^T \mathbf{r}_H, \tag{4.3}$$

where $\mathbf{r}_H$ contains the coefficients of the linear terms. For a Gaussian quantum state, the Wigner function has the well known form [48]

$$W(\boldsymbol{r}) = \frac{1}{(2\pi)^n \sqrt{\text{Det}\boldsymbol{\sigma}}} \exp\left(-\frac{1}{2}(\boldsymbol{r} - \langle\hat{\boldsymbol{r}}\rangle)^T \boldsymbol{\sigma}^{-1} (\boldsymbol{r} - \langle\hat{\boldsymbol{r}}\rangle)\right), \tag{4.4}$$

where $\langle\hat{\boldsymbol{r}}\rangle = \text{Tr}(\rho\hat{\boldsymbol{r}})$ denotes the vector of first moments, and $\boldsymbol{\sigma}$ is the covariance matrix (CM) defined as

$$\sigma_{ij} = \frac{1}{2}\langle\{\hat{r}_i, \hat{r}_j\}\rangle - \langle\hat{r}_i\rangle\langle\hat{r}_j\rangle, \tag{4.5}$$

with $\{\cdot, \cdot\}$ the anti-commutator. Gaussian states are thus fully specified by their first moments and covariance matrix. The CM is a real, positive semi-definite $2n \times 2n$ matrix that must satisfy the Robertson–Schrödinger uncertainty principle

$$\boldsymbol{\sigma} + \frac{i}{2}\Omega \geq 0. \tag{4.6}$$

General Gaussian States

In the previous section we explained how the Hamiltonian (2.11) preserves Gaussianity. Because of this, and the fact that Gaussian states (and in particular coherent states) are easily realised experimentally, we employ the Gaussian formalism to parametrize initial states and solve the dynamics [46–49]. We first note that Gaussian states are entirely parametrised by the first momenta $\mathbf{r}$ and the covariance matrix σ [46, 50]. We assume that the input states of the oscillators are uncorrelated. As such, we take a block-diagonal form for the covariance matrix

$$\boldsymbol{\sigma}(0) = \begin{pmatrix} \boldsymbol{\sigma}_1 & 0 \\ 0 & \boldsymbol{\sigma}_2 \end{pmatrix}, \tag{4.7}$$

where $\boldsymbol{\sigma}_{1(2)}$ denote the CM for the first and second physical oscillator. The covariance matrices of the physical oscillators can be recast in the following form via local symplectic transformations

$$\boldsymbol{\sigma}_i(\bar{n}, s) = \begin{pmatrix} \frac{1}{2}(2\bar{n}_i + 1)e^{s_i} & 0 \\ 0 & \frac{1}{2}(2\bar{n}_i + 1)e^{-s_i} \end{pmatrix}, \tag{4.8}$$

We note here that the only parameters which enter the physical covariance matrices are the squeezing parameters s_i and local thermal occupation number $\bar{n}_i = (\exp[\hbar\omega_0/k_b T_i] - 1)^{-1}$ [29].

Coherent states

Among Gaussian states, *coherent states* represent the simplest subclass. These are pure states with zero squeezing and minimal quantum uncertainty. A single-mode coherent state $|\alpha\rangle$ is obtained by applying the displacement operator $\hat{D}(\alpha)$ to the vacuum state $|0\rangle$:

$$|\alpha\rangle = D(\alpha)|0\rangle, \qquad D(\alpha) = \exp\left(\alpha a^\dagger - \alpha^* a\right), \tag{4.9}$$

where $\hat{a}$ and $\hat{a}^\dagger$ are the annihilation and creation operators of the mode. For multi-mode systems, such as our two-oscillator setup, a general multi-mode coherent state is given by the product

$$|\alpha_1\rangle|\alpha_2\rangle = D_1(\alpha_1)D_2(\alpha_2)|0\rangle_1|0\rangle_2, \tag{4.10}$$

with $D_i(\alpha_i)$ the displacement operator acting on mode i. Coherent states are not only analytically simple but also experimentally realisable. In mechanical systems, they can be generated by displacing the equilibrium position of the trap, for instance by applying a controlled initial push to the particle or by shifting the trapping potential. The amplitude α of the coherent state is directly related to the classical displacement in position and momentum:

$$\alpha(t) = \sqrt{\frac{m\omega}{2\hbar}}\langle x(t)\rangle + i\sqrt{\frac{1}{2\hbar m\omega}}\langle p(t)\rangle \tag{4.11}$$

The expectation values of the quadratures is then easily realised

$$\langle x\rangle = \sqrt{\frac{\hbar}{2m\omega}}(\alpha + \alpha^*), \qquad \langle p\rangle = -i\sqrt{\frac{\hbar m\omega}{2}}(\alpha - \alpha^*) \tag{4.12}$$

where here we are considering dimensionful quadratures. In our setup, we consider an initial condition where one oscillator is prepared in a coherent state and the other remains in its ground state. This state remains Gaussian and evolves under the gravitationally coupled Hamiltonian within the Gaussian formalism. The unsqueezed coherent initial state provides a natural starting point to investigate the phase accumulation induced by gravitational interactions, and to analyse its imprint on the output quadrature distributions. We can generate squeezed input states by exciting the physical modes into coherent states and then modifying the trap frequencies. A mode of frequency $a_1(\omega_1)$ can be reformulated as the result of squeezing another mode with frequency ω_0 by to the relation $a_1(\omega_0) = S^\dagger(s_1)a_1(\omega_1)S(s_1)$, where the squeezing operator is defined as $S(s_1) = \exp\left[\frac{1}{2}(s_1^* a_1^2(\omega_1) - s_1 a_1^{\dagger 2}(\omega_1))\right]$ and squeezing parameter is denoted $s_1 = \frac{1}{2}\log(\omega_0/\omega_1)$ [51]. Modifying only the frequency of the first mode $a_1(\omega_1) \to a_1(\omega_0)$ and initializing the $a_2(\omega_0)$ mode in the ground state, our initially uncorrelated input states with $T = 0$ read

$$|\alpha_1\rangle_{a_1(\omega_1)}|0\rangle_{a_2(\omega_0)} = |\alpha_1, s_1\rangle_{a_1(\omega_0)}|0, 0\rangle_{a_2(\omega_0)}\,, \tag{4.13}$$

where $|\alpha\rangle_{a_i(\omega_i)} = D(\alpha)_{a_i(\omega)}|0\rangle_{a_i(\omega)}$ is a coherent state of the $a_i(\omega)$-mode, $|\alpha_i, s_i\rangle_{a_i(\omega)} = S(s_i)D(\alpha_i)_{a_i(\omega)}|0\rangle_{a_i(\omega)}$ is a squeezed coherent state of the $a_i(\omega)$-mode, and $D(\alpha)_{a_i(\omega)} = \exp[\alpha a_i^\dagger(\omega) - \alpha^* a_i(\omega)]$ is the displacement operator.

4.2 General Evolution

As Gaussian states are fully determined by their first moments and covariance matrix, we are able to determine the full evolution of the system by determining the evolution of these two quantities. Here we follow the derivation in Refs. [29, 46]. We recall our full quadratic hamiltonian given in (2.4):

$$H/\hbar = \sum_{i=1,2} \frac{1}{2}\omega_0 \left(p_i^2 + \left(1 - \frac{2Gm}{d^3\omega_0^2}\right) x_i^2\right) - \frac{Gm^2}{\sqrt{d^4\hbar m\omega_0}}x_1 + \frac{Gm^2}{\sqrt{d^4\hbar m\omega_0}}x_2 + \frac{2Gm}{d^3\omega_0}x_1x_2. \tag{4.14}$$

Simple derivation of the Langevin equations yields

$$\begin{aligned}
\dot{x}_1 &= \omega_0 p_1, \\
\dot{x}_2 &= \omega_0 p_2, \\
\dot{p}_1 &= -\omega_0 \left(1 - \frac{2Gm}{d^3\omega_0^2}\right) x_1 - \frac{2Gm}{d^3\omega_0}x_2 - \gamma p_1 + \nu + \xi_1, \\
\dot{p}_2 &= -\omega_2 \left(1 - \frac{2Gm}{d^3\omega_0^2}\right) x_2 - \frac{2Gm}{d^3\omega_0}x_1 - \gamma p_2 - \nu + \xi_2,
\end{aligned} \tag{4.15}$$

where we have introduced a phenomenological damping rate γ, Browninan noise terms ξ_1, ξ_2, and again expressed the G-dependent constants as $\nu = Gm^2/\sqrt{\hbar m\omega_0 d^4}$. We assume a high $\mathcal{Q}$-factor set-up $Q = \omega/\gamma \gg 1$, such that the Brownian noises can be treated as uncoloured noise characterized by

$$\langle \xi_j(t)\xi_j(t') + \xi_j(t')\xi_j(t)\rangle/2 \simeq \gamma(2\bar{n}+1)\delta(t-t'), \tag{4.16}$$

for $j = 1, 2$. Eqs. (4.15) may be expressed in matrix form as

$$\dot{\hat{\boldsymbol{r}}}(t) = K\hat{\boldsymbol{r}}(t) + \mathbf{I}(t) \tag{4.17}$$

where K denotes the drift matrix

$$K = \begin{pmatrix} 0 & \omega_0 & 0 & 0 \\ -\omega_0\left(1 - \frac{2Gm}{d^3\omega_0^2}\right) & -\gamma & -\frac{2Gm}{d^3\omega_0} & 0 \\ 0 & 0 & 0 & \omega_0 \\ -\frac{2Gm}{d^3\omega_0} & 0 & -\omega_0\left(1 - \frac{2Gm}{d^3\omega_0^2}\right) & -\gamma \end{pmatrix}, \tag{4.18}$$

where $\boldsymbol{v}(t) = (0, \xi_1(t), 0, \xi_2(t))^T$ represents the stochastic noise contributions, and $\boldsymbol{\kappa} = (0, \nu, 0, -\nu)^T$ denotes the constant shift. The solutions to the Langevin equations are given by [29]

$$\boldsymbol{r}(t) = W_+(t)\boldsymbol{r}(0) + W_+ \int_0^t dt' W_-(t')\mathbf{I}(t'), \tag{4.19}$$

where $W_\pm(t) = \exp(\pm Kt)$ denotes the evolution matrices. The time evolution of the covariance matrix is then described by the following [46]:

$$\dot{\boldsymbol{\sigma}} = K\boldsymbol{\sigma} + \boldsymbol{\sigma}K^T + D, \tag{4.20}$$

where we introduce the diffusion matrix $D = \mathrm{Diag}[0, \gamma(2\bar{n}+1), 0, \gamma(2\bar{n}+1)]$ which describes how the system and environment couple [46], $\bar{n} = (\exp(\hbar\omega/k_BT) - 1)^{-1}$ is the thermal occupation number, and T the environmental temperature. Solutions to Eq. (4.20) are of the form

$$\boldsymbol{\sigma}(t) = W_+(t)\boldsymbol{\sigma}(0)W_+^T(t) + W_+(t)\int_0^t dt' W_-(t')DW_-^T(t')DW_+^T(t), \tag{4.21}$$

after integrating the above we find

$$\begin{aligned} K\boldsymbol{\sigma}(t) + \boldsymbol{\sigma}(t)K^T = & - D + KW_+(t)\boldsymbol{\sigma}(0)W_+^T(t) \\ & + W_+(t)\boldsymbol{\sigma}(0)W_+^T(t)K^T \\ & + W_+(t)DW_+(t)^T. \end{aligned} \tag{4.22}$$

This expression can generally be solved numerically, however for simple cases analytic solutions are also to be found.

4.3 Quantum Fisher Information - Covariance Matrix Formulation

Since the initial states of our system are Gaussian and remain so throughout the evolution, we must now to quantify their sensitivity to estimating G at a given time. This requires computing both the classical and quantum Fisher information. For a probability density $p_\theta(x)$ that depends on a parameter θ to be estimated, the classical Fisher information is defined as

$$F_c(\theta) = \int_{\mathbb{R}} dx p_\theta(x) \left(\frac{\partial \ln p_\theta(x)}{\partial \theta} \right)^2 . \tag{4.23}$$

For Gaussian states, this expression simplifies to

$$F_c(\boldsymbol{r}_\theta, \boldsymbol{\sigma}_{\theta m}) = (\langle \boldsymbol{r}'_\theta \rangle)^T \boldsymbol{\sigma}_{\theta m}^{-1} \langle \boldsymbol{r}'_\theta \rangle + \frac{1}{2} \mathrm{Tr} \left((\boldsymbol{\sigma}'_{\theta m} \boldsymbol{\sigma}_{\theta m}^{-1})^2 \right) , \tag{4.24}$$

where, in our context, the CFI is evaluated after a measurement has been performed on the system. Here $\boldsymbol{\sigma}_{\theta m}$ denotes the covariance matrix of the post-measurement state. The quantum Fisher information (QFI) quantifies the maximal amount of information about θ that can, in principle, be extracted from the quantum state. For Gaussian states, the QFI takes the form [48]

$$F_q(\rho_\theta) = (\langle \boldsymbol{r}'_\theta \rangle)^T \boldsymbol{\sigma}_\theta^{-1} \langle \boldsymbol{r}'_\theta \rangle + \frac{1}{2(1+P^2)} \mathrm{Tr} \left((\boldsymbol{\sigma}'_\theta \boldsymbol{\sigma}_\theta^{-1})^2 \right) , \tag{4.25}$$

where $\langle \boldsymbol{r}' \rangle$ is the derivative of the first-moment vector with respect to θ, $\boldsymbol{\sigma}$ is the covariance matrix and $P = (\det(\boldsymbol{\sigma}_\theta))^{-1/2}$ denotes the purity of the state. Generally, the best achievable sensitivity of an unbiased estimator of a parameter θ is bounded from below by the Quantum Cramér–Rao bound:

$$\delta\theta \geq \delta\theta_{\min} = \frac{1}{\sqrt{Q F_q(\rho_\theta)}}, \tag{4.26}$$

where Q is the number of performed experiments. Although the QCRB specifies the optimal sensitivity across all possible POVMs, it remains important to identify the specific measurement schemes that achieve this limit.

In Manuscript 7.1, the sensitivity of each measurement scheme is assessed by computing the classical Fisher information whilst focusing purely on local Gaussian measurements of both modes. This type of measurement can be represented by a POVM whose elements correspond to a two-mode Gaussian state with covariance matrix $\sigma_m = \mathrm{diag}[s, s^{-1}, s, s^{-1}]/2$, where $s \in [0, \infty]$ parametrises the degree of squeezing of the POVM elements. Performing such a measurement on a given state $\sigma(t)$, the best achievable sensitivity of said measurement is given by the CFI in Eq. (4.24) with the covariance matrix $\sigma(t) + \sigma_m$ [49].

4.4 Fisher information for time-continuous measurements

Here we cover the details of the dynamics under continuous measurements. First, note that typically, for systems involving levitated magnets, detection is done using SQUID-loop detectors, which provide a continuous homodyne signal rather than a projective measurement. This motivates the need to investigate continuously monitored systems. We do this by considering continuous general-dyne measurements. These make the dynamics stochastic whilst preserving Gaussianity, allowing us to keep using the Gaussian formalism, albeit with some important modification, instead of resorting to stochastic master equations. Continuous measurements are ubiquitous in laboratories and levitated set-ups. When a system is continuously measured, the (classical) information about the parameter of interest is contained in the continuous stochastic currents recorded by detectors. However, the QFI requires the knowledge of the full system-environment quantum state to be properly estimated. This is in general not an easy task and also the subject of current investigations [52–54]. Nonetheless, effective QFIs can be readily estimated given the stochastic dynamics of the system as discussed in [55]. Below we follow the latter route.

Let us consider a Gaussian system coupled to a large Markovian environment. Here we follow [46,56,57]. The environment is described by incoming modes $\hat{\mathbf{r}}_b(t)$, each interacting with the system at a given time t in the input-output formalism. The correlations of these modes are characterized by

$$\langle \{ \hat{\mathbf{r}}_b(t), \hat{\mathbf{r}}_b^\dagger(t') \} \rangle = \sigma_b \delta(t - t'), \quad \sigma_b + \frac{i}{2}\Omega \geq 0, \tag{4.27}$$

where σ_b is the environment's covariance matrix. The coupling between the system and (measured) environment in an interval dt is given by

$$\hat{\mathcal{H}}_C dt = \hat{\mathbf{r}}^T C \hat{\mathbf{r}}_b(t) dt. \tag{4.28}$$

Given this interaction, and considering the continuous monitoring of the bath modes via general-dyne measurements characterized via the CM σ_m, stochastic dynamical equations for the evolution of the first moments and the CM of the system can be derived [cf. [46,56] for the details of the derivation]. We have

$$d\boldsymbol{r}(t) = K\boldsymbol{r}(t)dt + \left(\frac{\sigma B + N}{\sqrt{2}}\right)\boldsymbol{dw} \tag{4.29}$$

$$\frac{d\sigma}{dt} = K\sigma + \sigma K^T + D + (\sigma B + N)(\sigma B + N)^T, \tag{4.30}$$

where $B = C\Omega^T(\sigma_b+\sigma_m)^{-1/2}$, $N = \Omega C\sigma_b(\sigma_b+\sigma_m)^{-1/2}$, and $\boldsymbol{dw}$ is a vector of independent Wiener increments $dw_i dw_j = \delta_{ij}dt$. As discussed in [57], the outcomes of measuring the bath mode are distributed according to a Gaussian multi-variate distribution with mean value $\boldsymbol{x}_m = \Omega C^T \boldsymbol{r}(t)dW$, with dW a real Wiener increment, and covariance matrix $(\sigma_b + \sigma_m)$. This allow the author in [57] to derive the infinitesimal CFI for a specific trajectory $dF_t^{(\mathrm{traj})}(\theta)$.

$$dF_t^{(traj)} = 2\langle \mathbf{r}' \rangle^T C\Omega^T(\sigma_b + \sigma_m)^{-1}\Omega C^T \langle \mathbf{r}' \rangle dt. \tag{4.31}$$

This is a stochastic quantity. Thus the CFI is computed by averaging it over the trajectories

$$dF_c(p_{traj}) = \mathbb{E}_{dw}[dF_t^{(traj)}], \tag{4.32}$$

and integrating the result in time:

$$F_c(p_{\mathrm{traj}}) = \int_0^t dF_c(p_{traj}). \tag{4.33}$$

Finally, the ultimate bound on the FI given a specific continuous measurement estimation strategy is discussed in [55] as given by

$$F_{\text{eff}} = F_c(p_{\text{traj}}) + \sum_{\text{traj}} p_{traj} F_q(\rho_c). \tag{4.34}$$

Here, the first term is the CFI computed as just described. The second term is the average over the stochastic trajectories of the QFI of the conditional state of the system solution of the stochastic master equation. We use this last expression in order to identify the ultimate bound for the general-dyne measurements that we consider in this text.

4.5 Logarithmic Negativity

As discussed, a way to arguably prove some of the quantum features of the gravitational field, proposed originally in [8], is to demonstrate its ability to entangle quantum source masses. Proving that the gravitational field is non-classical would then put to bed one of the most pressing questions of the past hundred years. It is therefore important to understand how much entanglement it is possible to generate between two interacting quantum systems in the ideal conditions offered by levitation. To quantify the amount of generated entanglement, we employ as a measure of it for our bipartite quantum system the logarithmic negativity [50]. Using this measure, we then search for input states ($\sigma(0)$) that yield the maximum possible entanglement generation at a given time for realistic parameters. We consider a input state in which the two oscillators are uncorrelated. In this case the covariance matrix takes block diagonal form:

$$\boldsymbol{\sigma}(t=0) = \begin{pmatrix} \boldsymbol{\sigma}_A & 0 \\ 0 & \boldsymbol{\sigma}_B \end{pmatrix} \tag{4.35}$$

where $\boldsymbol{\sigma}_{A/B}$ is the covariance matrix for the first/second oscillator respectively. For a single mode covariance matrix there is a local symplectic operation S which brings it into the standard diagonal form

$$\boldsymbol{\sigma}_A \to \boldsymbol{\sigma}_{sf} = \begin{pmatrix} a & 0 \\ 0 & a \end{pmatrix}. \tag{4.36}$$

From this standard form we may perform symplectic operation S on the state $\boldsymbol{\sigma}_{sf} \rightarrow \boldsymbol{\sigma}' = S\boldsymbol{\sigma}_{sf}S^T$. In particular, from the standard form we perform a phase space rotation $R(\theta)$ and mode squeezing $Sq(s)$.

$$\boldsymbol{\sigma}_{sf} \quad \rightarrow \quad \boldsymbol{\sigma}_i(a,s,\theta) = Sq(s)R(\theta)\boldsymbol{\sigma}_{sf}R^T(\theta)Sq^T(s) \tag{4.37}$$

Our general initial state for a single mode mode is then:

$$\boldsymbol{\sigma}_i(a,s,\theta) = \begin{pmatrix} a(\cosh(s)+\cos(2\theta)\sinh(s)) & -a\sin(2\theta)\sinh(s) \\ -a\sin(2\theta)\sinh(s) & a(\cosh(s)-\cos(2\theta)\sinh(s)) \end{pmatrix}. \tag{4.38}$$

In this form, we are able to parameterise the one mode initial state using three params parameters (a, s, θ), and thus parameterise the two mode uncorrelated initial state (4.35) with six parameters, the initial diagonal variances a, a', the squeezing parameters s, s', and the initial orientation of the of the states in phase space θ, θ'. In the following, we set $a = \frac{1}{2}$, corresponding to a highly idealised $T = 0$ input state.

Logarithmic Negativity In order to proceed we need to quantify entanglement. While there is no universal way to measure entanglement for all systems, some rigorous measures have been found for specific cases. In our case, that of a bipartite Gaussian system, we may exploit the "Positive Partial Transpose" (PPT) criterion [58]. The PPT criterion is a necessary condition for the density matrix ρ_{AB} of bipartite quantum system to be separable. Negativity of the positive partial trace implies that the subsystems are not separable, and thus entangled. We therefore employ logarithmic negativity as a quantifier of the level of entanglement in our system. We recall that the covariance matrix for a two mode system can be written in terms of three 2×2 matrices $\boldsymbol{\sigma}_A$, $\boldsymbol{\sigma}_B$, $\boldsymbol{\sigma}_{AB}$, such that the CM takes the form

$$\boldsymbol{\sigma} = \begin{pmatrix} \boldsymbol{\sigma}_A & \boldsymbol{\sigma}_{AB} \\ \boldsymbol{\sigma}_{AB}^T & \boldsymbol{\sigma}_B \end{pmatrix}, \tag{4.39}$$

where $\boldsymbol{\sigma}_A$ and $\boldsymbol{\sigma}_B$, describe the local correlations for modes A and B, while $\boldsymbol{\sigma}_{AB}$ characterises the inter-modal correlations. This covariance matrix has two symplectic eigenvalues ν_1, ν_2 where for a physical system $\nu_1, \nu_2 \geq 1/2$. We are concerned with the value of these symplectic eigenvalues after we have performed the partial transposition of the state, $\tilde{\nu}_\pm$, the covariance matrix transforms $\boldsymbol{\sigma} \rightarrow \tilde{\boldsymbol{\sigma}}$, where $\text{Det}\boldsymbol{\sigma}_{AB} \rightarrow -\text{Det}\boldsymbol{\sigma}_{AB}$. The symplectic eigenvalues of $\tilde{\boldsymbol{\sigma}}$ are then:

$$\tilde{\nu}_\pm = \frac{1}{\sqrt{2}}\sqrt{\Sigma \pm \sqrt{\Sigma^2 - 4\text{Det}\boldsymbol{\sigma}}}, \tag{4.40}$$

where $\Sigma(\boldsymbol{\sigma}) = \text{Det}\boldsymbol{\sigma}_A + \text{Det}\boldsymbol{\sigma}_B - 2\text{Det}\boldsymbol{\sigma}_{AB}$. The entanglement between the two modes can now be quantified using the logarithmic negativity:

$$E = \max[0, -\log_2(2\tilde{\nu}_-)] \tag{4.41}$$

where the time dependence is implicit. By maximising the logarithmic negativity at a fixed time over the initial state, we are able to extract the optimal input state for generating maximum entanglement at a given time. What we will see in the following section is that this optimal state is not unique, but depends on both the constraints of the system, and the time at which one wants to find maximum entanglement. Optimising the initial state amounts to numerically maximising the logarithmic negativity (4.41). This is achieved using the python package 'scipy', which provides the optimisation feature 'differential evolution'. With this in hand it is possible to input a set of ranges for the squeezing, temperature, and phase parameter, the best values of which are then extracted numerically, thus yielding the optimal input state state. The procedure is only valid at a fixed time, as such it must be repeated incrementally for a given time step, such that at each time step the optimal initial state is found.

Chapter 5

The Meissner Effect and Magnetic Trapping

The levitated system which we explore in this work relies on magnetic trapping of a dipole between two superconducting plates, reflecting modern experimental set-ups being used for force sensitive measurements, dark matter detection and tabletop experiments of fundamental physics [11, 13, 31–33]. This configuration enables high-stability in the particle's motion, with minimal decoherence and environmental disturbance. The trapping mechanism which is often used is based on the Meissner effect: a hallmark of superconductivity, in which magnetic fields are expelled from the interior of a superconductor [59, 60]. This effect allows superconductors to behave as perfect diamagnets, giving rise to repulsive magnetic forces that can stably levitate magnetic dipoles under certain conditions. In this section, we outline the physical principles and analytic modelling of such trapping configurations, which underlie the harmonic potentials used throughout the main results. Furthermore we briefly outline the use of finite element methods in approximating the solutions to the Maxwell equations in such superconducting traps.

5.1 The Meissner Effect

When a material transitions into the superconducting state below a critical temperature, it exhibits the Meissner effect: The complete expulsion of magnetic fields from its interior [60]. Unlike a perfect conductor, which merely prevents changes in magnetic flux, a superconductor actively expels internal magnetic fields by generating surface screening currents. These surface currents are governed by the London equations, which lead to an exponential decay of the magnetic field inside the material over a length scale known as the London penetration depth λ_L [59]:

$$\nabla^2 \mathbf{B} = \frac{1}{\lambda_L^2} \mathbf{B}. \tag{5.1}$$

In the limit $\lambda_L \to 0$, the superconductor behaves as an ideal diamagnet, imposing the boundary condition

$$\mathbf{B} \cdot \mathbf{n} \,|_{\partial\Sigma} = 0 \tag{5.2}$$

where $\mathbf{n}$ is the vector normal to the superconductors surface, and $\partial\Sigma$ denotes the superconducting boundary. In our modelling of traps, we adopt this idealized assumption, treating the superconducting plates as perfect field-excluding surfaces. In general, solving the Maxwell equations with the Meissner boundary condition is a non-trivial task, however some simple closed form solutions do exist. The method of image dipoles in particular has been used to solve the field equation's in the presence of different superconducting surfaces [11, 59]. In the paper *"Magnetic dipole trapping potential between infinite superconducting plates"* [30], also referenced as Manuscript 7.2, we derived the full induced magnetic field and potential generated by a dipole situated between two infinite superconducting plates. In this two plate system an infinite sum of image dipoles is required in order to correctly solve the boundary condition. In the following we perform the full derivation for the single plate case, as is known in the literature [11], to serve as a illustrative example.

5.2 Image Dipoles and Trapping Potentials

In the sort of system we are considering, the magnetic field is generated by a dipole which is situated near one (or more) infinite superconducting plates. We set the position of the superconducting plate to be at coordinate $z = a$. Noting that we have rotational symmetry of the geometry about the z-axis, we work in cylindrical coordinates (ρ, ϕ, z), and assume that the dipole is oriented in the (ρ, z)-plane. In this case, we may set the angular component $\phi = 0$, without loss of generality. The scalar potential at a point $\boldsymbol{r} = (\rho, z)$ for a dipole $\boldsymbol{\mu} = \mu(\cos\beta_0, \sin\beta_0)$ located at $\mathbf{r}_0 = (\rho_0, z_0)$ is given by

$$\Phi_0(\rho, z) = \frac{\boldsymbol{\mu} \cdot (\mathbf{r} - \mathbf{r}_0)}{4\pi|\mathbf{r} - \mathbf{r}_0|^3}, \tag{5.3}$$

where the magnetic field generated by the dipole potential is given by $\mathbf{B}_0 = -\mu_0 \nabla \Phi_0$. To model the magnetic interaction between a dipole and a superconducting surface, we employ the method of image dipoles. A point magnetic dipole placed near a superconducting plane induces screening currents in the material, which can be equivalently represented by an image dipole. This image is located symmetrically on the opposite side of the plane and oriented to ensure that the normal component of the magnetic field vanishes at the surface. As the dipole and its image both satisfy the Laplace equation with a boundary, the solution to the field equations is unique. To solve the boundary problem we place an image dipole located at $\mathbf{r}_1 = (z_1, \rho_1)$, such that the total scalar magnetic potential is given by

$$\Phi(\rho, z) = \Phi_0(\rho, z) + \Phi_{\mathrm{I}}(\rho, z) = \frac{\boldsymbol{\mu} \cdot (\mathbf{r} - \mathbf{r}_0)}{4\pi|\mathbf{r} - \mathbf{r}_0|^3} + \frac{\boldsymbol{\mu} \cdot (\mathbf{r} - \mathbf{r}_1)}{4\pi|\mathbf{r} - \mathbf{r}_1|^3}. \tag{5.4}$$

where Φ_0 is the potential from the real dipole and Φ_{I} is that from the image. We write explicitly:

$$\Phi_0(\rho, z) = \frac{\mu(z - z_0)\sin\beta_0 + \mu\rho\cos\beta_0}{4\pi(\rho^2 + z^2 + z_0^2 - 2zz_0)^{3/2}}, \tag{5.5}$$

$$\Phi_{\mathrm{I}}(\rho, z) = \frac{\mu(z - z_1)\sin\beta_1 + \mu\rho\cos\beta_1}{4\pi(\rho^2 + z^2 + z_1^2 - 2zz_1)^{3/2}}. \tag{5.6}$$

To enforce the boundary condition we demand that the component of the magnetic field normal to the surface of the plate. Differentiating with respect to z and evaluating the result at $z = a$ yields the boundary contribution:

$$\begin{aligned}\partial_z \Phi|_{z=a} =& \frac{\mu\sin\beta_0}{4\pi(\rho^2 + (z_0 - a)^2)^{3/2}} + \frac{\mu\sin\beta_1}{4\pi(\rho^2 + (z_1 - a)^2)^{3/2}} \\ &- 3(a - z_0)\left(\frac{\mu(a - z_0)\sin\beta_0 + \mu\rho\cos\beta_0}{4\pi(\rho^2 + (z_0 - a)^2)^{5/2}}\right) \\ &- 3(a - z_1)\left(\frac{\mu(a - z_1)\sin\beta_1 + \mu\rho\cos\beta_1}{4\pi(\rho^2 + (z_1 - a)^2)^{5/2}}\right).\end{aligned} \tag{5.7}$$

In order for the term (5.7) to be zero, we must fix the z location of the image dipole to be $z_1 = 2a - z_0$ and fix its orientation to be $\beta_1 = -\beta_0$. What we have done here is place an oppositely oriented dipole of equal magnetic dipole moment on the other side of the plate, which is the same distance from the plate as the original dipole. The scalar potential of the image charge is thus:

$$\Phi_{\mathrm{I}}(\rho, z) = \frac{-\mu(z - (2a - z_0))\sin\beta_0 + \mu\rho\cos\beta_0}{4\pi(\rho^2 + z^2 + (2a - z_0)^2 - 2z(2a - z_0))^{3/2}}. \tag{5.8}$$

Because both Φ_0 and Φ_{I} satisfy Laplace's equation and the combined potential satisfies the boundary condition at $z = a$, the uniqueness theorem for Laplace's equation guarantees that this solution is unique [60]. The potential experienced by the dipole above the plate is calculated using [59]:

$$U(z_0, \beta_0) = -\frac{1}{2}\boldsymbol{\mu} \cdot \mathbf{B}_{\mathrm{I}}, \tag{5.9}$$

where $\mathbf{B}_{\mathrm{I}} = -\mu_0 \boldsymbol{\nabla} \Phi_{\mathrm{I}}$. Some simple calculation yields the potential of a dipole levitated above an infinite superconducting plate:

$$U(z_0, \beta_0) = \frac{\mu_0 \mu^2}{64\pi(z - a)^3}(1 + \sin^2\beta_0). \tag{5.10}$$

Since the system is translationally invariant along the ρ axis, we set $\rho = 0$. It's important to note that this potential on its own is *not* trapping. Indeed we must introduce some form of gravitational potential to the z-axis

$$U(z_0, \beta_0) = \frac{\mu_0 \mu^2}{64\pi(z - a)^3}(1 + \sin^2\beta_0) + mg(z - a) \tag{5.11}$$

where m is the mass of the particle and g is the gravitational acceleration. While these results are known in the literature [11], the derivation serves as a demonstration of the methods used in deriving the trapping potential for the two plate case.

Harmonic Approximation and Trap Frequencies

For small displacements around the centre of motion in the trap, the potential can be expanded to quadratic order in both the z and β degrees of freedom. This harmonic approximation is valid when the oscillation amplitudes are small compared to the plate separation. The effective spring constants governing the dynamics are

$$k_z = \left.\frac{\partial^2 U}{\partial z_0^2}\right|_{z_0=0,\beta_0=0}, \quad k_\beta = \left.\frac{\partial^2 U}{\partial \beta_0^2}\right|_{z_0=0,\beta_0=0}. \tag{5.12}$$

From these, the natural oscillation frequencies of the vertical and angular modes are: Thus we find the resonance frequencies to be

$$\omega_z = \left.\sqrt{\frac{1}{m}\frac{\partial^2 U}{\partial z_0^2}}\right|_{z_0=0,\beta_0=0} \qquad \omega_\beta = \left.\sqrt{\frac{1}{I}\frac{\partial^2 U}{\partial \beta_0^2}}\right|_{z_0=0,\beta_0=0} \tag{5.13}$$

where m is the mass of the dipole and I is the moment of inertia of the dipole. These frequencies describe the harmonic motion of the particle within the trap and serve as inputs to the dynamical models used in later sections.

5.3 Finite element method

The Finite Element Method (FEM) is a numerical technique widely used to solve partial differential equations (PDEs) in physics, particularly for problems with complex geometries and boundary conditions, such as the magnetic field interactions in superconducting traps [61]. In the context of magnetic dipole trapping between superconducting plates, FEM provides a computational framework to approximate the magnetic field and potential energy, complementing the analytic solutions derived via the method of image dipoles, and also providing an alternative avenue of checking their validity (and vice versa). FEM works by discretising a continuous domain into a finite number of subdomains, or elements, to form a mesh of simple geometric shapes, such as triangles in two dimensions or tetrahedra in three dimensions. To solve a PDE on this mesh, the equations are first approximated over each individual element using basis functions, typically polynomials, which are then combined to construct a global solution [62]. The full solution is then obtained by minimizing a functional, such as the system's energy, subject to boundary conditions.

In the work 7.2 we employ such finite element methods to solve Maxwell's equations numerically in three dimensions for a magnetic dipole in a superconducting trap. In such a case the Meissner effect imposes a zero normal component of the magnetic field at the superconductor's surface, i.e., $\mathbf{n} \cdot \mathbf{B} = 0$, which FEM enforces numerically [61]. This trap is designed to approximate the two dimensional geometry explored the previous section as well as in Manuscript 7.1 [30], further verifying the validity of the analytic expressions, as well as reaffirming their role as a benchmark for more general computational simulations of such traps, which are critical for geometries where analytic solutions are not currently available.

For our system we model the levitated particle as a point dipole and take the London penetration depth to zero $\lambda_L \to 0$, treating superconductors as perfect dia-magnets, consistent with the idealized models used in analytic approaches [30,59]. Thus, the system can be modelled using the following differential equations:

$$\begin{aligned} \nabla \times \boldsymbol{B}_{\mathrm{I}} &= 0 \qquad \forall x \in \Sigma, \\ \boldsymbol{n} \cdot \boldsymbol{B}_{\mathrm{I}} &= -\boldsymbol{n} \cdot \boldsymbol{B}_0 \;\; \forall x \in \partial\Sigma, \end{aligned} \tag{5.14}$$

where here $\mathbf{B}_{\mathrm{I}}$ is the induced magnetic field, $\mathbf{B}_0$ is the magnetic field generated by the dipole, $\boldsymbol{n}$ represents the unit vector normal to the surface of the superconductor, $\partial\Sigma$ represents the surface of the superconductor and Σ the space outside of the superconductor.

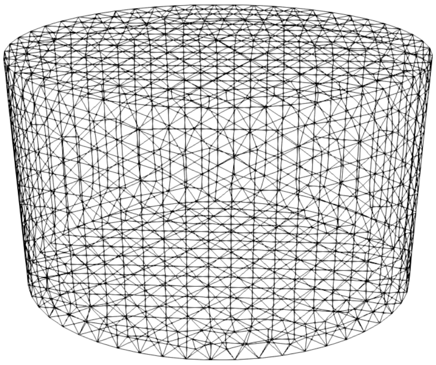

Figure 5.1: An example of a slightly squished cylindrical mesh generated with the python package GMSH [63], the Meissner boundary conditions can be applied in FENICSx (or another FEM platform) to the boundary, and the maxwell equations can then be solved numerically.

To proceed a suitable domain Σ must be generated, which in our case is constructed to conform to the geometry of the superconducting trap, ensuring accurate representation of boundaries where the Meissner effect is imposed. An example of such a mesh, representing a slightly elliptical cylindrical trap can be seen in 5.1.

It must be noted that the accuracy of FEM depends on the mesh quality, which must provide enough resolution to resolve spatial variations in the magnetic field accurately, particularly near superconducting boundaries where field gradients are significant. Finer meshes improve accuracy but increase computational cost significantly. Other methods such adaptive meshing, where element sizes are refined in regions of high field gradients, enhances efficiency [62], however such methods were not employed in this work.

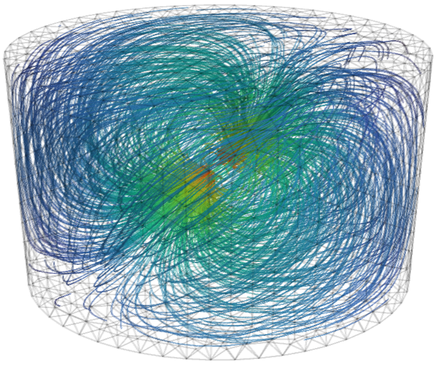

Figure 5.2: An example of the magnetic field lines generated by a magnetic dipole with the Meissner boundary conditions applied to the boundary of the mesh, which in this case is a slightly elliptical cylinder. The simulation was generated using the python package FENICSx [61].

A visualisation of such an FEM simulation can be seen in 5.2, where the mesh seen in 5.1 was used to model an example trap containing a magnetic dipole with the Meissner boundary conditions applied to the boundary of the mesh. The simulations present in Manuscript 7.2 were performed using the same FENICS package [61] a free package in python which implements the finite element method, furthermore the meshes were generated with GMSH [63], another python package. The simulations were magneto-static for each position and orientation of the particle. What this means is that that in order to map out the potential landscape of the trap, one must iteratively run simulations for each position and orientation of the particle, within a certain domain of which you wish to study. In our work, we wished to calculate the potential energy of the dipole around its equilibrium position. In order to do this, we procedurally calculated the induced magnetic field for an iterated list of positions and orientations. At each point we calculated the potential energy using (5.9). Around the equilibrium position the potential is approximately quadratic, as such we used the 'scipy' package to fit a quadratic function to the iterated points, such that the potential is approximated using (5.13).

Chapter 6

Results

In this chapter we present the main results of thesis, primarily based on those presented in Manuscripts 7.1 *'Quantum Metrology of Newton's constant with Levitated Mechanical Systems'* and 7.2 *'Magnetic Dipole Trapping Potential between Infinite Superconducting Plates'*. In section 6.1 we present the main results of the paper 7.2, presenting the analytic potential derived using the method of image dipoles, and then its comparison to a numerical simulation of a system of approximately the same geometry. Indeed, we see that this analytic result is in good agreement with numerical results, opening the doors to further study of the dynamics and modelling of dipoles levitated in superconducting traps. In section 6.2 we present the results of manuscript 7.1, presenting a theoretical bound on the sensitivity of a mechanical interferometer consisting of two levitated dipoles in superconducting traps in measuring G, considering both projective measurements of the quadratures. We see that this type of system promises good relative uncertainty in estimating G under projective measurements, beating the current standard relative uncertainty [3] by several orders of magnitude. Furthermore we employ a continuous measurement strategy, employing the conditional QFI presented in section 4.4. This strategy accounts for the back reaction of the measurement on the state, reducing the sensitivity of our measurements and yielding lower information gain. With this we show that continuous measurement strategies are unable to achieve the sensitivities of the projective case, despite being more experimentally realistic. Furthermore we investigate additional noise sources which may be present, such as the effect of Casimir, thermal and vacuum fluctuations on the sensitivity of the set-up, and find their contributions to be minimal.

Finally, we present work based on a work of Krisnanda et al [29]. Here we analyse the entanglement generation of the same set-up using the logarithmic negativity as a quantifier. This investigation was conducted with more optimised input parameters to provide an upper bound on the maximum possible entanglement generation in this set-up, optimising over the input state to maximise the possible generated entanglement when considering input states in their ground state, evolving with both mechanical damping and squeezing. This allows us to evaluate such levitated systems for their viability in conducting experiments similar to the BMV experiment [18], or other experiments testing for gravitationally mediated entanglement.

6.1 Analytic trapping potential

This section covers the main results of Manuscript 7.2. The potential experienced by a magnetic dipole trapped between two infinite superconducting plates was derived analytically using the method of image dipoles. This approach, adapted from electrostatics, constructs an infinite series of mirror dipoles to satisfy the boundary conditions imposed by the Meissner effect in the superconducting surfaces. Initially, the analytic form of the trapping potential for a dipole levitated above a single infinite superconducting plane located at $z = a$ was re-derived as a pedagogical step. The dipole, assumed to lie in the (ρ, z)-plane and oriented at an angle β_0, experiences a potential of the form:

$$U(z_0, \beta_0) = \frac{\mu_0 \mu^2}{64\pi (z_0 - a)^3}(1 + \sin^2 \beta_0) \tag{6.1}$$

This expression confirms known results and serves as a limiting case for the more complex two-plate system. Extending to the case of two infinite superconducting plates at $z = a$ and $z = b$, a self-consistent series of image dipoles must be constructed. We begin by introducing two image dipoles to impose the boundary conditions on each plate, however these dipoles themselves require image dipoles to correct their contributions to the plates. This necessitates an infinite series of image dipoles, such that the boundary conditions are enforced and that the normal component of the total magnetic field on each plate is

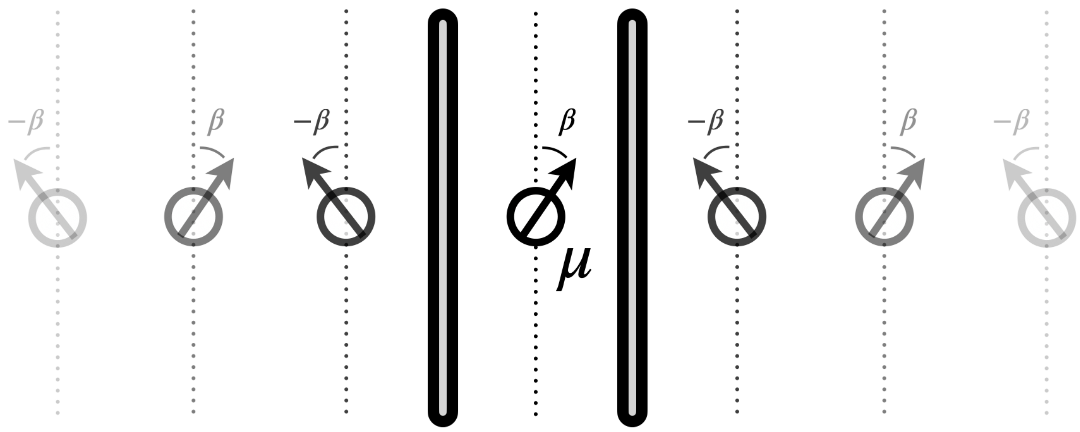

Figure 6.1: Schematic illustration of the infinite sequence of image dipoles representing a magnetic dipole μ confined between two infinitely extended superconducting plates. The method of image dipoles models the effect of the superconducting boundaries by generating an infinite series of image dipoles, thereby satisfying the required boundary conditions.

zero. We can decompose the total scalar potential

$$\Phi_{\mathrm{tot}} = \Phi_0 + \Phi_{\mathrm{I}} \tag{6.2}$$

where Φ_0 is the contribution from the dipole between the two plates and $\Phi_{\mathrm{I}} = \sum_{n\neq 0} \Phi_{n+} + \sum_n \Phi_{n-}$ is the contribution from the image charges. The positions of these image dipoles are given by:

$$z_{n+} = 2n(b-a) + z_0, \quad z_{n-} = 2n(b-a) + 2b - z_0, \quad n \in \mathbb{Z} \tag{6.3}$$

with orientations

$$\beta_{n+} = \beta_0, \quad \beta_{n-} = -\beta_0, \quad n \in \mathbb{Z} \tag{6.4}$$

The total scalar potential Φ_{tot} is simply the superposition of the original dipole and all image dipoles. Evaluating the potential energy at the dipole's position yields the trapping potential:

$$U(z_0, \beta_0) = \frac{\mu_0 \mu^2}{8\pi} \left[\frac{\cos^2\beta_0 - 2\sin^2\beta_0}{4|b-a|^3} \zeta(3) + \sum_{n\in\mathbb{Z}} \frac{1+\sin^2\beta_0}{|z_0 - z_n^-|^3} \right] \tag{6.5}$$

where $\zeta(n)$ is the Riemann zeta function for $n \in \mathbb{Z}$. This is the main result of Manuscript 7.2. We note again that as both Φ_0 and Φ_{I} satisfy Laplace's equation and the combined potential satisfies the boundary condition at $z = a$, the uniqueness theorem for Laplace's equation guarantees that this solution is unique [60]. This expression converges, except when the dipole approaches either superconducting plane, as expected. In the limit $b \to \infty$, the expression reduces to the single-plate result seen in Eq. 6.1. Assuming the plates are located symmetrically about the origin $z = \pm b$, the potential admits harmonic expansions in both the vertical (z) and rotational (β) degrees of freedom near equilibrium. The resonant frequencies of the dipole motion can then easily be determined:

$$\omega_z = \sqrt{\frac{93}{256} \cdot \frac{\zeta(5)}{\pi} \cdot \frac{\mu_0 \mu^2}{b^5 m}}, \quad \omega_\beta = \sqrt{\frac{5}{64} \cdot \frac{\zeta(3)}{\pi} \cdot \frac{\mu_0 \mu^2}{b^3 m r^2}} \tag{6.6}$$

These expressions provide a direct analytic handle on the dynamics of the system. Furthermore, fixing $z_0 = 0$ this expression further simplifies to:

$$U(\beta_0) = \frac{\mu_0 \mu^2 \zeta(3)}{128 \pi b^3} (5 - \cos(2\beta_0)) \tag{6.7}$$

This potential forms a double-well potential with minima at $\beta_0 = 0$ and π, corresponding to dipole alignment parallel to the superconducting plates. To validate the analytic potential, numerical simulations were performed using the Finite Element Method utilising FEniCS [61], a free python package used in such numerics. The magneto-static field equations were solved for a point-like dipole in a cylindrical approximation to the infinite plate geometry. The extracted potential energy landscape for small displacements in z and β was extracted by iteratively solving the maxwell equations for different locations and orientations of the dipole, and the potential was plotted and fit to quadratic curves, and the corresponding resonant frequencies were extracted.

The comparison between the analytic and numerical results is summarized in 6.1. The numerical z-mode frequency is in good agreement with the analytics, with a relative deviation of approximately 0.56%. The β-mode frequency however showed a larger deviation of approximately 4.78%, which is attributed to the cylindrical geometry in the simulation introducing additional boundary contributions not present in the idealized analytic model. Increasing the radius of the simulation domain was shown to reduce this discrepancy, in-

	Analytic	FEniCS	$\mathrm{Diff}_{\mathrm{rel}}$
f_z	155.545	154.673	0.56%
f_β	323.659	308.899	4.78%
U	4.096×10^{-8}	4.126×10^{-8}	0.73%

Table 6.1: Results for the z frequency, β frequency, and potential energy, obtained using the analytic expressions in Eq. (6.5) and (6.6) as well as the finite element method (FEniCS).

dicating that finite-size effects play a non-negligible role, especially in rotational modes. These results confirm the validity and precision of the image dipole method in modelling levitated dipole systems in superconducting environments and establish it as a reliable analytic benchmark for numerical simulations. The derived potentials and frequencies are directly relevant for ongoing experiments in magnetic levitation, quantum sensing, and searches for weak forces and dark matter [31, 32].

6.2 Quantum Fisher Information - Projective measurements

In this section we present the key results of Manuscript 7.1. To begin we show how the truncated QFI is derived, then we compare with the full QFI of the system under the evolution of the Hamiltonian (4.14), presenting the achievable sensitivity of the system when accounting for different input states with thermal temperature T, squeezing s and a mechanical damping rate of γ. To begin the truncated Hamiltonian seen in (2.11) is given:

$$H/\hbar \simeq \omega_0 a_+^\dagger a_+ + \omega_0(1-\eta) a_-^\dagger a_- \,. \tag{6.8}$$

It is possible to translate between coherent states of the $a_{1/2}$ modes and the $a_\pm$ modes

$$|\alpha\rangle_{a_1}|\beta\rangle_{a_2} = |(\alpha+\beta)/\sqrt{2}\rangle_{a_+}|(\beta-\alpha)/\sqrt{2}\rangle_{a_-}, \tag{6.9}$$

$$|\mu\rangle_{a_+}|\nu\rangle_{a_-} = |(\mu-\nu)/\sqrt{2}\rangle_{a_1}|(\mu+\nu)/\sqrt{2}\rangle_{a_2}, \tag{6.10}$$

where the lower index refers to the operator which defines the ground state. The state evolves correspondingly as

$$e^{-iHt/\hbar}|\alpha\rangle_{a_1}|\beta\rangle_{a_2} = \left|e^{-i\omega_0 t}\frac{\alpha+\beta}{\sqrt{2}}\right\rangle_{a_+} \otimes \left|e^{-i\omega_0(1-\eta)t}\frac{\beta-\alpha}{\sqrt{2}}\right\rangle_{a_-}. \tag{6.11}$$

For coherent states, the QFI is given to be the modulus square of the derivative of the coherent amplitude with respect to the parameter we wish to measure [64]. For a product of two coherent states $|\alpha\rangle \otimes |\beta\rangle$ the QFI is simply the sum of the QFI's of the individual states $F_q(\theta) = 4(|\partial_\theta \alpha|^2 + |\partial_\theta \beta|^2)$. We see again that the G-dependence of the evolution of the coherent modes under Eq. (6.11) is coded entirely in the a_- mode. The expression of the QFI for a coherent state evolving under (6.8) is then:

$$F_q(G) = 4\left|\partial_G\left(e^{-i\omega_0(1-\eta)t}\Delta\right)\right|^2, \tag{6.12}$$

where $\Delta = (\beta-\alpha)/\sqrt{2}$ is simply the input amplitude of the a_- mode. We see here that the QFI scaltes as $\propto t^2$ for longer time scales, such that it diverges for $t \to \infty$. Furthermore this yields a $1/\sqrt{N}t$ scaling for the Quantum Cramér–Rao bound. Simplifying 6.12 further we see

$$F_q(G) = 16\left(\frac{m}{d^3\omega_0}\Delta\right)^2 t^2. \tag{6.13}$$

where we have used $\eta = 2Gm/d^3\omega_0^2$. This is one of our main results [28].

CFI of Intensity Measurement.

Here we briefly cover how the CFI for an intensity measurement of our system was derived. For an intensity measurement in quantum optics, one would usually do photon counting. However, we are not dealing with a light source, our system is mechanical. As such, one can perform an intensity measurement by measuring the energy of the oscillators. This energy measurement is done by measuring the amplitude $x_{\max}$ as well as the frequency of the oscillations. This can be derived from the potential energy $m\omega^2 x_{\max}^2/2$ for times where the kinetic energy is vanishing and as such the total energy equals the potential energy. When considering a product of m coherent states $|\Phi\rangle = |\beta_1\rangle \otimes \cdots \otimes |\beta_m\rangle$,

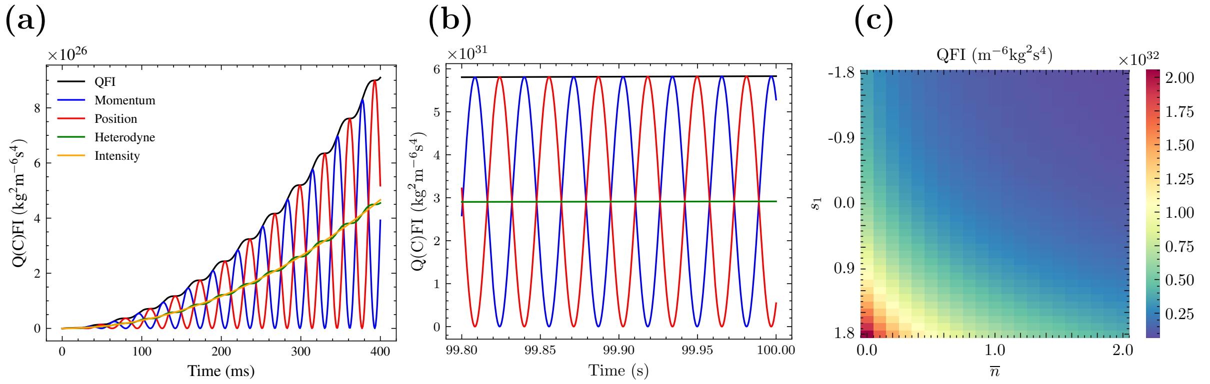

Figure 6.2: QFI and CFI for different measurement schemes. **(a)** Black curve: Exact QFI calculated using the CM; Red curve: CFI for $s \to 0$ (Projective position measurement); Blue curve: CFI for $s \to \infty$ (Projective momentum measurement); Green curve: CFI for $s \to 1$ (Heterodyne measurement); Yellow curve: CFI for intensity measurement. **(b)** Same as in panel **(a)** but for longer times. In panels **(a)** and **(b)**, we took the input state $|\alpha_1, 0\rangle_{a_1(\omega_0)} \otimes |0, 0\rangle_{a_2(\omega_0)}$ with parameters $\omega_0 = 100$ rad s^{-1}, $m = 1 \times 10^{-4}$kg, $d = 5 \times 10^{-3}$m, $\alpha_1 \approx 3.374 \times 10^{12}$, $\alpha_2 = 0$, $\bar{n} = 0$. **(c)** QFI as a function of the squeezing s_1 and thermal occupation number $\bar{n}$ for a displaced squeezed thermal state at $t = 100$s. Other parameters as in panels **(a)** and **(b)**, where the input amplitude is defined through the initial displacement as $\langle x_i(0)\rangle = \sqrt{2}\alpha_i$.

the CFI is then the sum of the individual CFI's of each mode respectively [64]

$$F_c^{ph}(\theta) = 4 \sum_{i=1}^{m} \left(\mathrm{Re}\left[\frac{\beta_i^*}{|\beta_i|} \frac{\partial \beta_i}{\partial \theta} \right] \right)^2 . \tag{6.14}$$

Rewriting Eq. (6.11) in terms of the physical modes a_1 and a_2, we evaluate the CFI associated with intensity measurements on these modes. This leads, after straightforward calculation, to the approximate form for the CFI in the case of intensity detection,

$$F_c^{ph}(G) = 8 \left(\frac{m}{d^3 \omega_0} \Delta \right)^2 t^2 . \tag{6.15}$$

Homodyne and Heterodyne Detection

We consider local projective general-dyne measurements acting on each physical mode, a class of measurements that is straightforward to implement in Gaussian systems [46–49]. The effect of performing such a measurement can be accounted for by modifying the system covariance matrix according to $\boldsymbol{\sigma}(t) \to \boldsymbol{\sigma}(t) + \boldsymbol{\sigma}_m$ [49], where the

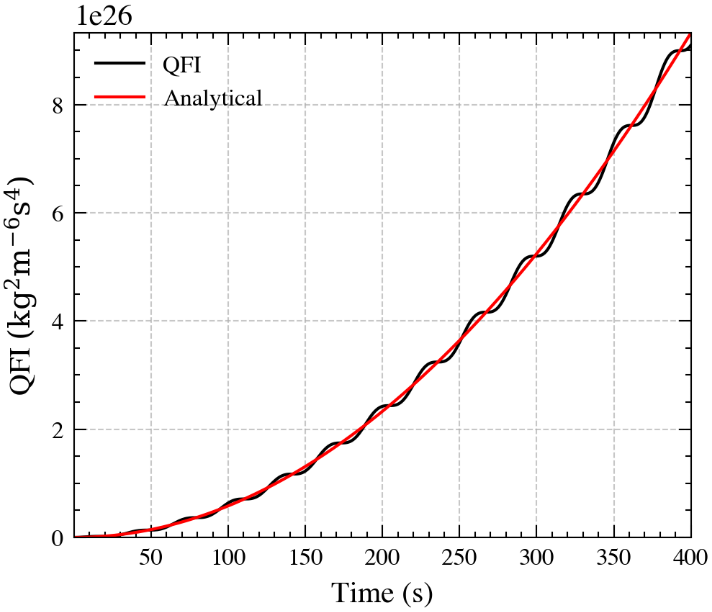

Figure 6.3: Comparison of the exact QFI (Black) and the approximation Eq. 6.13, which utilizes the corotating frame for input state $|\alpha_1, 0\rangle_{a_1(\omega_0)} \otimes |0, 0\rangle_{a_2(\omega_0)}$ with parameters $\omega_0 = 100\,\mathrm{rad\ s^{-1}}$, $m = 1 \times 10^{-4}\,\mathrm{kg}$, $d = 5 \times 10^{-3}\,\mathrm{m}$, $\alpha_1 \approx 3.374 \times 10^{12}$, $\alpha_2 = 0$, $\bar{n} = 0$.

term $\boldsymbol{\sigma}_m = \mathrm{Diag}\left[s, s^{-1}, s, s^{-1}\right]/2$ corresponds to projective measurements of the physical $a_1(\omega_0)$, $a_2(\omega_0)$ modes. The parameter s selects the measurement basis: $s \to 0$ corresponds to a position measurement, $s \to \infty$ to a momentum measurement, and $s = 1$ to balanced heterodyne detection. With the parameters discussed in chapter 2 the prefactor in Eq. (6.13) is $16m^2\Delta^2/(d^6\omega_0^2) = 5.8 \times 10^{27}\mathrm{kg^2\,m^{-6}\ s^2}$, which leads to the very rapid increase of the QFI.

The results of these projective measurement procedures can be seen in in Fig. 6.2(a)–(b). Projective homodyne measurements of either quadrature repeatedly saturates the QFI and outperform the balanced heterodyne case; thus, at instants where the projective measurement meets the QFI it is the optimal measurement. For instance, a projective momentum readout at $t \approx 100\,\mathrm{s}$ saturates the QFI, corresponding to a sensitivity of $\delta G \approx 1.31 \times 10^{-16}\,\mathrm{kg^{-1}m^3s^{-2}}$, or relative statistical error $\delta G/G \approx 1.96 \times 10^{-6}$, and beating the current CODATA value of $\delta G/G \approx 2.2 \times 10^{-5}$ [3] by one order of magnitude. At longer times the quadratic growth of the QFI becomes dominant. If instead a projective position measurement is made at $t = 10^5\,\mathrm{s}$, the sensitivity reaches $\delta G \approx 1.31 \times 10^{-19}$, corresponding to a relative uncertainty of $\delta G/G \approx 1.96 \times 10^{-9}$, which is a four order of magnitude improvement over CODATA standard uncertainty. We see in Figure 6.3

that the result of Eq. (6.13) contains the leading t^2 scaling of the exact result, displayed in Fig. 6.2. This validates using the 'rotating wave approximation' with the parameter regime studied here.

Unlike conventional optical interferometers, where one typically measures the intensity difference between the two output ports, our set-up grants direct access to the output quadratures. As we see in equation 6.15, measuring intensity differences yields a significant information gain, but at only half the observed for projective homodyne detection. As such intensity-based readouts do not saturate the QCRB and are therefore inferior to homodyne detection at all times.

Squeezed and thermal states states – More general Gaussian input states are conveniently parametrised by their squeezing parameters s_1, s_2, thermal occupation $\bar{n}$, and the first and second moments, as introduced earlier. The input amplitude is related to the initial displacement by $\langle x_i(0)\rangle = \sqrt{2}\alpha_i$. Fig. 6.2 **(c)** illustrates how squeezing and the thermal occupation $\bar{n}$ of the $a_1(\omega_0)$ mode influence the QFI. Increasing $\bar{n}$ decreases the sensitivity at all times. Indeed, the QFI scales as $F_q(G) \propto (1+2\bar{n})^{-1}$, which implies $\delta G \propto (1+2\bar{n})^{1/2}$ [28]. This reduction is visible at $t = 100\,\mathrm{s}$ in Fig. 6.2 (c). Despite this loss, the QCRB remains attainable with projective position and momentum measurements over both short and long timescales.

Holding temperature fixed, squeezing the momentum quadrature of the input $a_1(\omega_0)$ mode ($s_1 > 0$) increases the QFI for all times. As an example, for $s_1 = 1.73$ and $\bar{n} = 0$ the relative uncertainty at $t = 100\,\mathrm{s}$ is $\delta G/G \approx 1.08 \times 10^{-6}$, roughly a factor of two improvement over the unsqueezed case at the same temperature; similar improvements are observed at other times. Conversely, squeezing the position quadrature ($s_1 < 0$) reduces the QFI and worsens sensitivity when the initial displacement lies in the position coordinate. However, if the initial coherent amplitude is placed in the momentum coordinate instead (i.e. $\langle p_1(0)\rangle = \sqrt{2}\alpha_1$ and $\langle x_1(0)\rangle = 0$), the dependence on squeezing reverses: position squeezing ($s_1 < 0$) then provides approximately a two-fold improvement in sensitivity for all times.

The effect of damping on the sensitivity of the system is considered with respect to currently realistic experimental set-ups, where quality factors $\mathcal{Q} = \omega/\gamma$ of order $\mathcal{Q} \approx 10^7$ have been achieved [12,13,15,65]. Introducing damping causes an exponential suppression

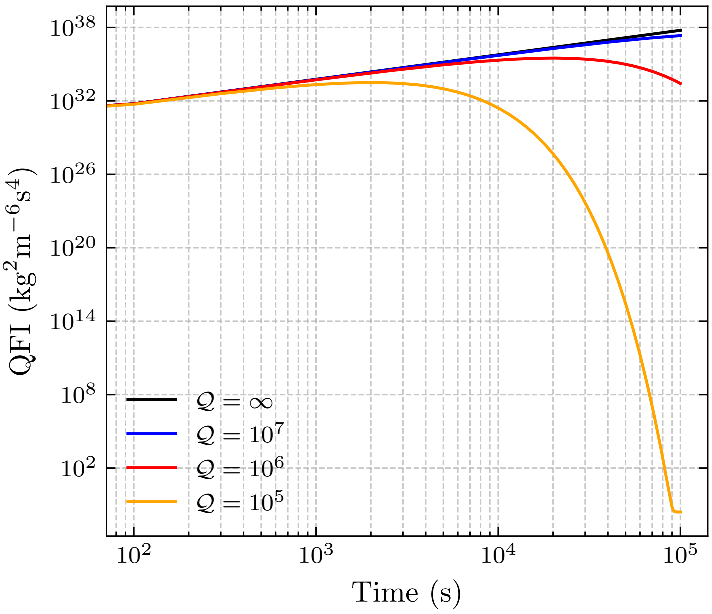

Figure 6.4: QFI against time for different values of the $\mathcal{Q}$ factor (see the plot legend). All curves shown are for the input state $\rho = |\alpha_1, 0\rangle_{a_1(\omega_0)} \otimes |0, 0\rangle_{a_2(\omega_0)}$ with parameters $\omega_0 = 100\,\mathrm{rad\ s^{-1}}$, $m = 1 \times 10^{-4}\,\mathrm{kg}$, $d = 5 \times 10^{-3}\,\mathrm{m}$, $\alpha_1 \approx 3.374 \times 10^{12}$, $\alpha_2 = 0$, $\bar{n} = 0$.

of the QFI, approximately $F_q^{\gamma}(G, \gamma) \approx F_q(G) e^{-\gamma t}$. Including both finite temperature $\bar{n}$ and mechanical damping γ leads to the modified analytic form

$$F_q(G) = \frac{16}{(1 + 2\bar{n})} \left(\frac{m}{d^3 \omega_0} \Delta \right)^2 e^{-\gamma t}\, t^2, \tag{6.16}$$

as can be seen in [28]. From this expression the QFI attains a maximum in finite time and decays for large t, see Fig. 6.4, consequently, the t^2 scaling is effectively limited to shorter durations when $\mathcal{Q}$ is small. For separable coherent inputs the maximum value is $\max F_q^{\gamma}(G, \gamma) = \frac{64 m^2 \Delta^2}{d^6 \omega^2 \gamma^2 e^2}$ at $t_{\max} = 2/\gamma$. Using our parameter choices and $\mathcal{Q} = 10^7$, the minimum achievable relative standard uncertainty is $\delta G_{\min}/G \approx 2.67 \times 10^{-9}$ corresponding to roughly 2.3 days of measurement and representing a four orders of magnitude improvement over the current CODATA value. For a lower quality factor $\mathcal{Q} = 10^5$ (i.e. $\gamma = 10^{-3}\,\mathrm{s^{-1}}$), the QFI falls to near zero after about 10^5 s. Curves with non-zero γ show similar behaviour but at different time scales. At short times the influence of damping is negligible.

6.3 Quantum Fisher Information - Continuous measurements

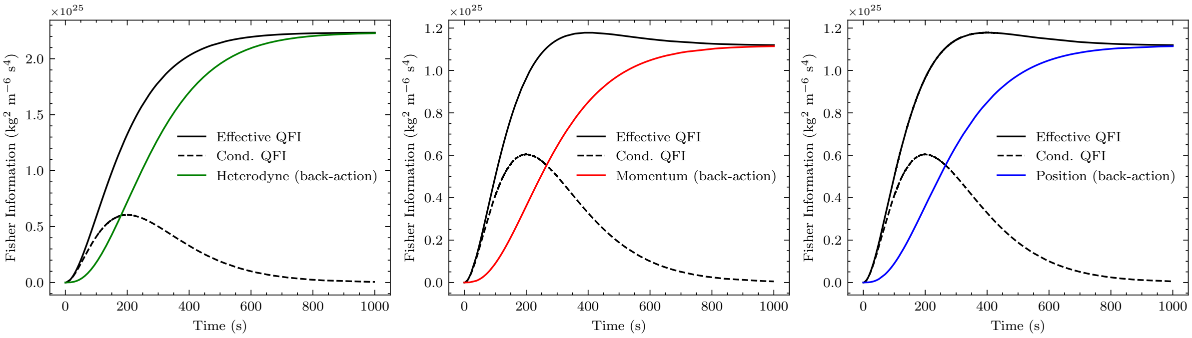

Figure 6.5: Here we compare the left-hand side of eq. (4.34), representing the effective QFI (black curves) with the second term on the right-hand side of eq. (4.34) — representing the conditional QFI (dashed black lines) — and the first term on the right-hand side of the same equation that is the CFI (coloured curves). The three panels show these quantities for the three measurement strategies considered. The parameters are $\bar{n} = 1.31 \times 10^6$ ($T = 1\,\mathrm{mK}$) and $\Gamma_m = 1 \times 10^{-2}$.

While projective measurements prove themselves to be an effective strategy for saturating the QCRB, they are often difficult to realise experimentally. Indeed, for the case of levitated magnets in superconducting traps, the most common measurement device would be a SQUID (superconducting quantum interference device). These SQUIDS perform continuous measurements of the magnetic flux through a small superconducting coil. In order to model this type of continuous measurement, we followed the formalism laid out in section 4.4. As discussed in section 4.4, performing a continuous measurement on quantum system causes a back-reaction on the system [46, 66]. By measuring the system, we further disturb it and thus lose information. Therefore instead of gaining all of the information in a 'single shot', the information accumulates over the course of the duration of the measurement. However, whilst we accumulate information, we also disturb the system, potentially destroying information we would have otherwise wished to measure.

Using the experimentally reasonable input parameters which were presented in section 2, we can calculate the CFI seen in equation (4.33) for different types of continuous measurement, that being homodyne, position and momentum measurements at a rate of $\Gamma_m = 1 \times 10^{-2}$ [19], and compare with the conditional and effective QFI, as presented in (4.34). We see in all cases that the CFI of the measurement saturates the effective QFI at around $t = 1000$s, with homodyne measurements yielding twice as much CFI as the momentum and position measurements. Indeed, this behaviour is also seen in the projective case for high temperature of $T = 1$mK. We see that the best possible relative uncertainty in this case is $\delta G/G \approx 3 \times 10^{-3}$, which is approximately 2 orders worse than the standard CODATA value [3]. It may be possible to improve this value by optimising over the measurement rate, leaving room for future work.

6.4 Additional Sources of Noise

In any experimental proposal, it is essential to consider the possible influence of secondary forces and environmental perturbations that may affect the dynamics of the system or mask the signal of interest. For levitated mechanical systems, common concerns include Casimir-Polder interactions, electrostatic potentials, and mechanical fluctuations in the trap geometry. The purpose of this section is to show that, for the system parameters considered in this work, such effects are negligible. This is supported by analytic estimates and scaling arguments which demonstrate that the relevant forces either fall off rapidly with distance, are suppressed by the geometry of the trap, or lie well below the sensitivity threshold of our gravitational measurement protocol. In particular, the large trap separations (on the order of several millimetres), combined with effective shielding and cryogenic operation, render Casimir forces and thermal effects irrelevant. Similarly, mechanical fluctuations of the trap geometry contribute at higher order in the dynamical evolution and do not couple significantly to the gravitational interaction term in the Hamiltonian. As such, we conclude that the dominant contribution to the system's evolution remains gravitational.

Particle Thermal Displacement – For two levitated magnets with mass $m = 10^{-4}\,\mathrm{kg}$, trap frequency $\omega_0 = 100\,\mathrm{rad/s}$, and temperature $T = 1\,\mathrm{mK}$, the root-mean-square (RMS) thermal displacement is calculated as:

$$\delta x_{\mathrm{thermal}} = \sqrt{\frac{k_B T}{m\omega_0^2}} \approx 1.18 \times 10^{-13}\,\mathrm{m}, \tag{6.17}$$

where k_B is the Boltzmann constant. For two particles separated by a distance $d = 5\,\mathrm{mm}$, the relative distance fluctuation is:

$$\delta d = \sqrt{2} \cdot \delta x_{\mathrm{thermal}} \approx 1.67 \times 10^{-13}\,\mathrm{m} \tag{6.18}$$

The relative error in the gravitational coupling parameter $\eta = \frac{2Gm}{d^3\omega_0^2}$ is:

$$\frac{\delta\eta}{\eta} = 3\frac{\delta d}{d} \approx 1 \times 10^{-10}. \tag{6.19}$$

This is rather low compared the target sensitivity of $\delta G/G \approx 1.96 \times 10^{-9}$ and is negligible compared to the achievable sensitivity of $\delta G/G \approx 4.33 \times 10^{-6}$ at current experimental temperatures and quality factors. The impact of thermal fluctuations diminishes at lower temperatures due to the $\sqrt{T}$ scaling.

Faraday Shield Thermal Displacement – For a Faraday shield made of lead with stiffness $k_{\mathrm{shield}} \approx 10^2\,\mathrm{N\,m^{-1}}$ [67] at $T = 1\,\mathrm{mK}$, the RMS thermal displacement is:

$$\delta z = \sqrt{\frac{k_B T}{k_{\mathrm{shield}}}} \approx 1.18 \times 10^{-14}\,\mathrm{m}. \tag{6.20}$$

The relative distance error due to the shield's displacement is:

$$\frac{\delta d}{d} \approx \frac{\delta z}{d} \approx \frac{1.18 \times 10^{-14}}{5 \times 10^{-3}} \approx 2.36 \times 10^{-12}, \tag{6.21}$$

where we have modelled the fluctuating surface by a since harmonic degree of freedom. This contribution is also negligible compared to the target sensitivity of $\delta G/G \approx 1.96 \times 10^{-9}$, confirming that thermal displacements of the Faraday shield do not significantly impact the precision of the gravitational constant measurement.

Vacuum effects – In magnetic levitation within a superconducting cavity, the levitation mechanism is passive, eliminating the need for optical or microwave cavities and active fields. However the systems considered above can also apply to optically levitated setups. The gravitational interaction yields an effective coupling parameter $\eta \sim 10^{-11}$. In contrast, vacuum-induced effects, such as single-photon radiation-pressure coupling, scale as $\hbar\omega_c(x_{\mathrm{zpf}}/L)$ [68–70]. For the parameters used throughout ($m = 10^{-4}\,\mathrm{kg}$, $\omega_0 = 100\,\mathrm{rad/s}$), the zero-point fluctuation amplitude is $x_{\mathrm{zpf}} \approx 7.26 \times 10^{-17}\,\mathrm{m}$. With a trap (cavity) scale $L \sim 5\,\mathrm{mm}$, the ratio $(x_{\mathrm{zpf}}/L) \sim 10^{-14}$, making vacuum-induced effects negligible by over three orders of magnitude. To quadratic order, this scales as $(x_{\mathrm{zpf}}/L)^2 \sim 10^{-28}$, further confirming their insignificance.

Casimir effects – When considering the Casimir forces between the levitated oscillators and the plates, the proximity-force approximation of the plane-sphere Casimir energy $\mathcal{E}_{PS}^{PFS}$ [71] is given

$$\mathcal{E}_{PS}^{PFS} = -\frac{\hbar c \pi^3 r}{720(l/2 - r)^2} \tag{6.22}$$

where r is the radius of the oscillator, and l the distance between the two plates. Taking $l = 4.9\mathrm{mm}$ and $r \approx 1.5\mathrm{mm}$, we see that the ratio between the Casimir and gravitational term is $r_{cg} \sim 1 \times 10^{-8}$. It is thus legitimate to ignore the Casimir terms in our model.

6.5 Entanglement Generation

In this section, we examine the conditions under which entanglement can be generated between two gravitationally coupled levitated oscillators. Building on the theoretical framework of Gaussian states and previous proposals such as that of Krisnanda et al. [29], we numerically investigate how parameters such as damping, initial phase, squeezing, and temperature affect the resulting logarithmic negativity. This analysis provides a practical protocol for identifying optimal experimental configurations for entanglement generation. Furthermore, we use the same set of highly optimised parameters, such that the entanglement generated serves as an upper bound for all current and future experiments. By quantifying entanglement in terms of logarithmic negativity, we obtain a robust, experimentally relevant measure that captures the non-classical correlations induced by gravitational coupling. As in [29] we will assume that our masses are two oscillating spheres of uniform density ρ and radius R, separated by a distance $2.1R$, as seems to be possible in current experimental setups [12–14]. Our dimensionless parameter can therefore be written $\eta = 8\pi G\rho/3(2.1)^3\omega^2$, which independent of the mass of the objects. As our entanglement parameter η scales linearly in the density ρ, a value which can often vary by orders of magnitude. This makes material selection a critical factor in experimental design, as the density alone governs the strength of gravitational interaction in this regime. With this in mind, we seek the 'best case scenario', such that a benchmark is provided for future experiments. Osmium is the densest available material, with $\rho = 22.59\,\mathrm{g/\,cm^3}$. This provides an upper bound for the achievable entanglement, considering other parameters fixed. With this in mind, for our numerical calculations we use the value $\eta = 1.36 \times 10^{-4}$, where $\omega = 0.1$Hz, as was done in the cooling of a mechanical oscillator to near its ground state [72–77].

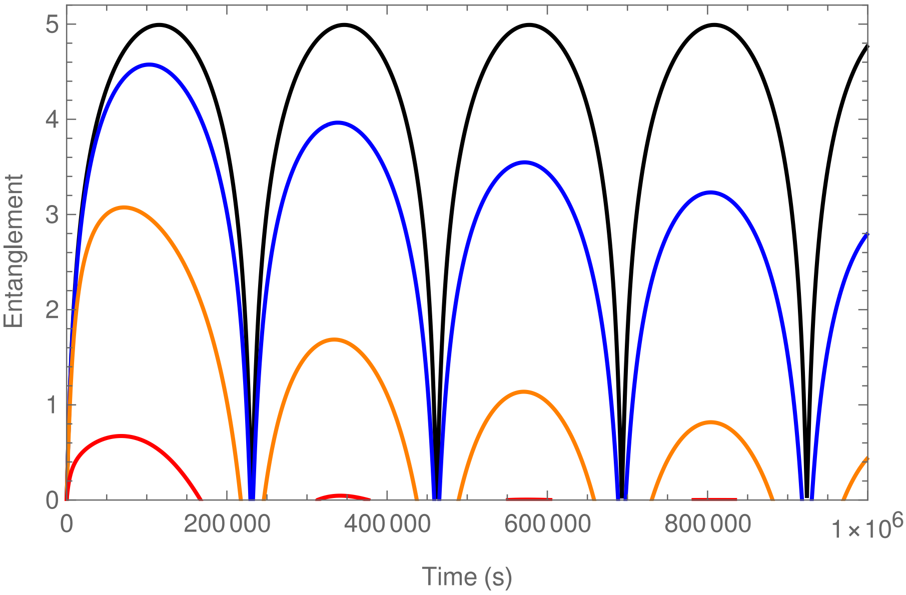

Figure 6.6: Maximum logarithmic negativity of the system with different damping rates. We have used $\gamma = \{0,\ 1,\ 10,\ 100\} \times 10^{-7}$ (black, blue, orange, and red curve, respectively).

Damping: Understanding the impact of dissipation is crucial for determining the practical limits of entanglement observability in these systems. As can be seen in Fig 6.6, systems with a higher damping rate γ generate less entanglement. The logarithmic negativity oscillates over both long and short time periods, with the amplitude decaying over long times for damped oscillators, something which is not present in the undamped case. This can be seen more clearly in Fig 6.6 , where the undamped scenario is represented by the black curve. If we take $\gamma = 1 \times 10^{-6}$ as an example, represented by the orange curve in Fig 6.6, we observe that the logarithmic negativity is significant within the first 1×10^5 seconds, the amplitude being half that of the idealised undamped system, however the amplitude of said negativity decreases for longer time-frames. This is even more pronounced for $\gamma = 1 \times 10^{-5}$, represented by the red curve. From this it is clear that high experimental Q factors ($Q = \omega/\gamma$) are critical in the engineering of entanglement generating systems. Quality factors of 10^7 have been experimentally achieved for levitated micro-magnets [12, 13]. The states which achieve maximum logarithmic negativity any given time always had maximum squeezing (which in this case was limited to $s = 1.73$, the current record [38, 39]) and minimum temperature ($\bar{n} = 0$). The initial phases θ, θ' are not quite so simple. It can be seen that the entanglement is maximised when they are of equal value $\theta = \theta'$, however their exact value which maximises the logarithmic negativity depends explicitly on t. This phase dependence shows that timing control or state preparation protocols is critical in optimising entanglement yield for short measurement windows. More clearly, the phase of the optimal initial state depends on precisely when you wish to reach maximum entanglement. Indeed, as can be seen in Figure 6.7, the maximum logarithmic negativity is plotted in black, which sits above the various analytic evolutions of given initial states. Each state differs by a phase of $\pi/8$, and it can be seen that each initial state achieves the maximal value, albeit usually at different times.

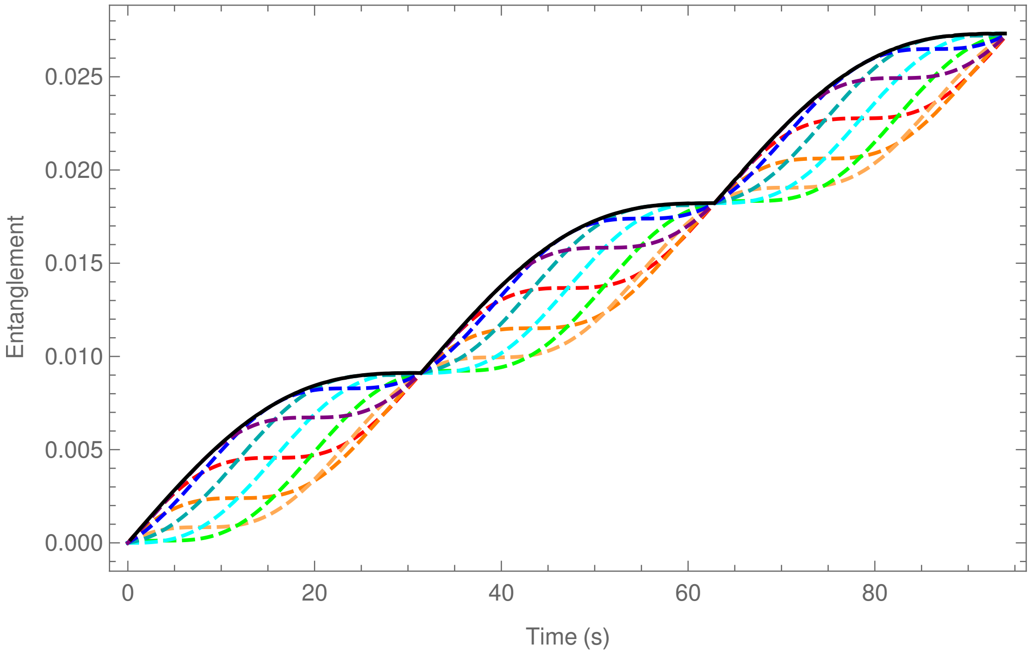

Figure 6.7: Optimised logarithmic negativity (Black) for $s = 1.73$, $\bar{n} = 0$, $\gamma = 1\times10^{-6}$, and $\theta = \theta'$. The coloured lines represent analytic evolutions of states with the aforementioned parameters, but with different initial phases. For example: Red $\theta = 0$, Green $\theta = 3\pi/8$, Cyan $\theta = 4\pi/8$, Blue $\theta = 6\pi/8$, Purple $\theta = 7\pi/8$.

It should be noted that independently of the initial phase, the curves coincide at regular intervals. This can be seen in Fig 6.7 at $t_1 \approx 31.4$, $t_2 \approx 62.8\,\mathrm{s}$ and so on. It is little surprise that this coincidence of curves occurs with period $T_E = \pi/\omega$, which is the time taken for the system to complete a half rotation in phase space. Independently of the initial angle, the states will (from different starting points) sweep out the same path in phase space, such that after T_E they will all have been at some point in time in the same state, simply at different times. The entanglement accumulated over the π rotation is for short times approximately constant, as such at these regular intervals, the logarithmic negativity of the system is independent of starting orientation.

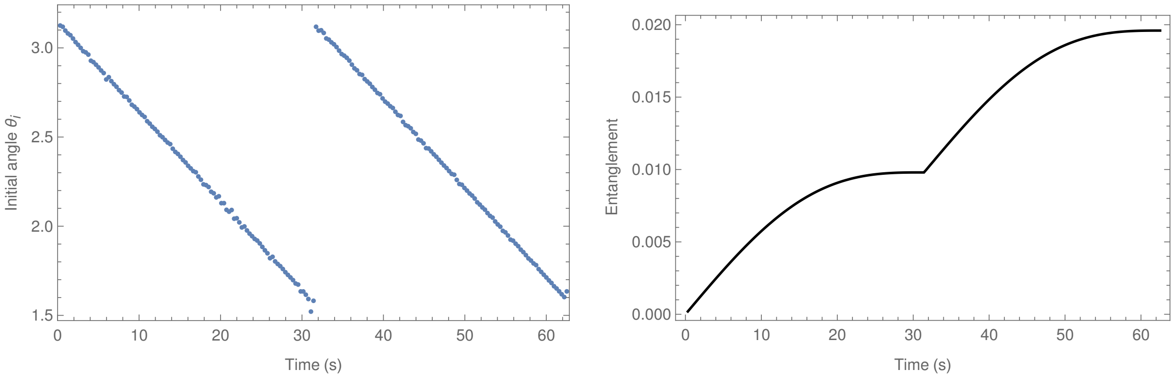

Figure 6.8: Left: Optimal input angle θ_i for $s = 1.73$, $\gamma = 0$, $\bar{n} = 0$. Right: Maximal entanglement for $s = 1.73$, $\gamma = 0$, $\bar{n} = 0$
.

To achieve the maximum logarithmic negativity away from these 'coincidence points', the optimal input angle θ_i takes periodic values between $\pi/2 \leq \theta_i \leq \pi$, with the period T_C. The linear relationship between the logarithmic negativity and θ_i is more apparent when plotted, as in Fig 6.8.

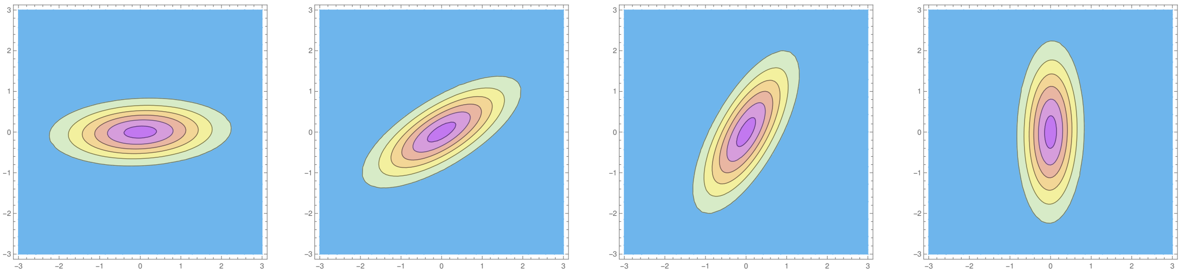

(a) $t = 1,\ \theta \approx 3.10$ (b) $t = 11,\ \theta \approx 2.59$ (c) $t = 21,\ \theta \approx 2.08$ (d) $t = 31,\ \theta \approx 1.59$

Figure 6.9: The Wigner Function of the initial states which generates maximum entanglement at different times.

To gain further insight into the phase-space evolution of the optimal states, the Wigner function of one mode at several key time points is presented in Fig 6.9, where the evolution of the Wigner function (4.4) of one of the $\boldsymbol{\sigma}_1$ mode is presented, showing the optimal initial state over the period T_C. Again, it is clear that the optimal states complete a clock-wise $\pi/2$ rotation in phase space over the period. To summarize, we have found a procedural way to optimise entanglement generation between two gravitationally coupled mechanical oscillators with respect to the initial state. Indeed, the optimal state is maximally squeezed, at a minimum temperature, and has low rates of mechanical damping. The input phase contributes significantly for shorter time frames, but for longer experiments differences in initial phase become irrelevant.

Here, we have put forward a procedural way to optimise entanglement generation between two gravitationally-coupled mechanical oscillators with respect to the initial state. Indeed, the optimal state is maximally squeezed, at a minimum temperature, and has low rates of mechanical damping. The input phase contributes significantly for shorter time frames, but for longer experiments differences in initial phase become irrelevant. The approach that we have brought forward is plug-and-play in nature as it allows to identify the best initial configuration of the system for a given dynamical arrangement, and for set environmental conditions. The method will be utilised to inform the developments that should be pursued in the lab so as to guarantee optimal entanglement-generation performance. Future work could investigate how this protocol performs under more realistic noise models, or extend the optimisation to include feedback and continuous monitoring strategies.

Chapter 7

Conclusion and Outlook

We developed a quantum-metrological framework for estimating Newton's gravitational constant G using two magnetically levitated mechanical oscillators confined to superconducting traps. Working in the quadratic Hamiltonian regime, the dynamics remain Gaussian and information about G is encoded in the phase evolution of one of the normal modes of the coupled system; this information is quantified using the Quantum Fisher Information. From the effective Hamiltonian for the interferometric protocol we derived the QFI and established a theoretical benchmark relative uncertainty $\delta G/G \approx 2.67 \times 10^{-9}$ under the idealised yet experimentally motivated parameter set considered here, thereby defining a clear target for future experiments.

The analysis of measurement strategies clarifies the principal trade-offs between achievable sensitivity and experimental practicality. Input squeezing of quadratures increases the QFI and projective measurements of position and momentum can periodically saturate the quantum Cramér–Rao bound. By contrast, heterodyne and intensity measurements attain at most roughly fifty percent of the optimal sensitivity, and continuous monitoring is strongly limited by measurement back-action: continuous readout introduces disturbance that significantly reduces the extractable information. These results highlight a fundamental information–disturbance trade-off that experimental protocols must negotiate when attempting to saturate the QFI bound.

Within the same Gaussian framework we computed logarithmic negativity to quantify gravitationally mediated correlations between the levitated masses and obtained numerical bounds on entanglement in the presence of weak damping and thermal noise. Although the predicted entanglement is modest under realistic noise, its origin in a purely gravitational interaction (absent other couplings) makes it a meaningful and experimentally testable signature in efforts to probe the quantum nature of gravity. Furthermore, we derived an exact closed-form expression for the magnetic trapping potential of a dipole between two superconducting plates using the method of image dipoles and validated this analytic result against finite-element simulations that approximate the infinite-plate limit; the resulting double-well structure offers a natural platform for orientational tunnelling and related mesoscopic quantum phenomena.

The theoretical sensitivity bounds reported here are compatible with recent progress in cryogenic levitation and superconducting readout, where ferromagnetic particles have been trapped and cooled near their motional ground state and effective quality factors $Q \sim 10^7$ are being reported [11–15]. Realising the metrological advantage identified in this work therefore requires further improvements in mechanical dissipation, operation at milli-kelvin temperatures to suppress temperature based sensitivity loss, and high-fidelity readout together with the ability to trap and control two particles.

Several practical challenges and limitations remain and point to immediate directions for follow-on work. A primary experimental obstacle is the precise characterisation of other parameters such as particle mass, trap frequency, magnetisation and relative alignment, as the uncertainties in these quantities propagate into the final estimate of G. In the present theoretical analysis these parameters were treated as known; converting the best-case benchmarks into experimentally actionable requirements therefore demands an explicit treatment of such parameters, either via linear error propagation or within a multi-parameter Fisher framework, together with sensitivity scans of δG and entanglement versus the dominant imperfections. Additionally, decoherence mechanisms not modelled in full detail here, such as eddy currents and flux pinning in the superconducting environment, will introduce effective damping and dephasing that must be mitigated or incorporated into refined theoretical models.

Beyond the direct goal of improving the measurement of G, the methods developed in this thesis have broader applicability. The formalism is directly applicable to searches for other inverse-square or short-range forces (for example Yukawa-type modifications to Newtonian gravity) and to the wider programme of quantum sensing with levitated systems. The quantitative entanglement estimates and the analytic trap potential provide concrete, testable benchmarks for experiments that seek both to certify gravity-mediated quantum correlations and to employ levitated sensors in searches for weak, exotic interactions.

To conclude, this thesis establishes a coherent theoretical foundation and a set of concrete numerical targets for quantum-enhanced gravitational metrology using magnetically levitated mechanical systems. Achieving the sensitivity limits derived here will require coordinated advances in materials, cryogenics and quantum control, together with careful uncertainty characterisation and improved modelling of non-ideal decoherence. The bounds and robustness checks presented in this work provide a clear and testable roadmap; with continued experimental progress at the mesoscopic scale, probing quantum aspects of gravity moves from the realm of distant speculation toward a practically approachable experimental programme.

Appendix: publications

7.1 First publication

Quantum Metrology of Newton's constant with Levitated Mechanical Systems

Francis J. Headley,[1, *] Alessio Belenchia,[2] Mauro Paternostro,[3, 4] and Daniel Braun[1]
[1] *Institut für Theoretische Physik, Eberhard-Karls-Universität Tübingen, 72076 Tübingen, Germany*
[2] *Institute of Quantum Technologies, German Aerospace Center (DLR), D-89077 Ulm, Germany*
[3] *Universita' degli Studi di Palermo, Dipartimento di Fisica e Chimica - Emilio Segre', via Archirafi 36, I-90123 Palermo, Italy*
[4] *Centre for Quantum Materials and Technologies, School of Mathematics and Physics,*
Queen's University Belfast, BT7 1NN, United Kingdom

(Dated: April 7, 2025)

Newton's constant is the least well-measured among the fundamental constants of Nature, and, indeed, its accurate measurement has long served an experimental challenge. Levitated mechanical systems are attracting growing attention for their promising applications in sensing and as an experimental platform for exploring the intersection between quantum physics and gravitation. Here we propose a mechanical interferometric scheme of interacting levitated oscillators for the accurate estimation of Newton's constant. Our scheme promises to beat the current standard by several orders of magnitude.

Introduction– Accurate measurement of Newton's constant $G \approx 6.67 \times 10^{-11}\,\mathrm{m}^3\mathrm{kg}^{-1}\mathrm{s}^{-2}$ [1] has long been an experimental challenge, primarily due to the weakness of the gravitational interaction with respect to the other fundamental interactions. To date, G remains the fundamental constant with the highest uncertainty. This uncertainty is due to a host of experiments with large deviations in their experimental findings [2–7]. The precise measurement of G requires tremendous isolation from external sources of noise. This, combined with the difficulty of precisely measuring masses and the impossibility of screening gravitational interactions, leaves the precise value of Newton's constant uncertain.

Recently, levitated mechanical systems, i.e. particles suspended in electromagnetic, optical, or acoustic fields, have emerged as a promising experimental platform to address some of these challenges [8–11]. Magnetic levitation, in particular, has been shown to offer exceptional isolation from non-gravitational environmental disturbances [10] as well as long-lived coherent oscillations [12–14], essential for stable experimental setups capable of high-precision measurements. Furthermore, as magnetic levitation allows for stable trapping of Planck-scale masses, it holds the promise to allow for high-precision measurements of the gravitational field at sub-millimetric distances and, in the long run, the detection of the gravitational field of quantum sources [15–18].

In this work, motivated by the recent advancements in levitomechanics, in particular the cooling of mechanical oscillators close to their quantum ground state [19–24] and the preparation of mechanical systems in squeezed states [22, 25–27], we show how to engineer a mechanical interferometer using two harmonically trapped masses whose gravitational interaction generates a G-dependent phase. We test a variety of input-states and show that this scheme has the potential to estimate G to great accuracy via simple local measurements that saturate the quantum Cramér-Rao bound.

Modelling the system– Consider two harmonic oscillators with free Hamiltonian

$$H_0 = \sum_{i=1,2} \left(\frac{p_i^2}{2m} + \frac{1}{2} m\omega_0^2 x_i^2 \right). \tag{1}$$

We assume oscillators with identical masses m and identical trapping frequencies ω_0 that can be adapted e.g. through the choice of the trap geometry. The non-relativistic gravitational interaction potential between two spherical masses m at distance r between their center of masses reads

$$U(r) = -G\frac{m^2}{r}, \tag{2}$$

where G denotes Newton's constant. The assumption of perfect harmonic oscillators is tenable only as far as the oscillating amplitudes x_1, x_2 of the particles around their equilibrium positions remain small compared to their distance d at equilibrium and the width of the trap. Writing $r = |d - x_1 + x_2|$ we expand to quadratic order in $x_1, x_2 \ll d$,

$$H_G = -\frac{Gm^2}{d}\left(1 + \frac{(x_1 - x_2)}{d} + \frac{(x_1 - x_2)^2}{d^2} + \dots\right). \tag{3}$$

The full Hamiltonian is

$$H = H_0 + H_G. \tag{4}$$

The linear term in $x_1 - x_2$ leads to a G-dependent shift of the equilibrium positions of the oscillators relative to the uncoupled case. It contains information about G but is difficult to exploit, as G cannot be switched off. We therefore focus on the modes with the new, shifted equilibrium positions and denote them as the "physical modes" $\{x_1, p_1, x_2, p_2\}$. In these coordinates,

---

[*] francis.headley@uni-tuebingen.de

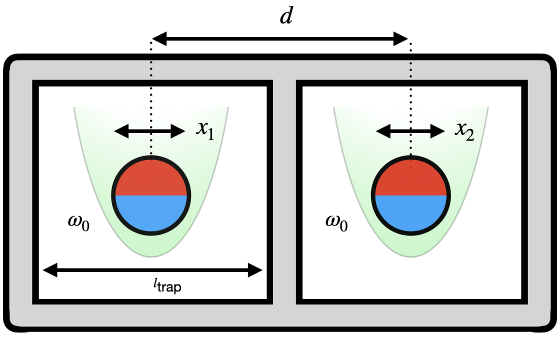

FIG. 1. Sketch of the set-up. Two objects of mass m separated by a distance d and interacting through gravity levitate in harmonic traps of frequency ω_0, generated e.g. by trapping small ferromagnets in superconducting boxes. Here $x_{1,2}$ are the displacements from the respective equilibrium positions.

the linear term in (3) is eliminated. The treatment including the linear contributions is given in the Appendix. We write x_i, p_i in units of the oscillator length, $x_i \to \sqrt{\hbar/m\omega_0}x_i$, $p_i \to \sqrt{\hbar m\omega_0}p_i$. After introducing the normal modes $x_\pm = (x_2 \pm x_1)/\sqrt{2}$ and $p_\pm = (p_2 \pm p_1)/\sqrt{2}$, the quadratic parts of the Hamiltonian are diagonalized,

$$H/\hbar = \omega_0 a_+^\dagger a_+ + \omega_0(1-\eta)a_-^\dagger a_- - \eta(a_-^2 + a_-^{\dagger 2}), \quad (5)$$

with $a_\pm = (x_\pm + ip_\pm)/\sqrt{2}$ and $\eta = 2Gm/d^3\omega_0^2$. A dependence on G appears only in the a_- mode, i.e. the relative motion of the coupled oscillators. Both η-dependent terms in Eq. (5) can generate G-dependent squeezing of the a_- mode. In the following we investigate the sensitivity of such a system for the estimation of G Newton's constant including the effect of quantum and thermal fluctuations.

Parameter estimation theory – In classical estimation theory, the inverse of the Fisher information (CFI)

$$F_c(\theta) = \int_{\mathbb{R}} dx p_\theta(x) \left(\frac{\partial \ln p_\theta(x)}{\partial\theta}\right)^2, \quad (6)$$

provides a lower bound to the mean square error of any (unbiased) estimator of a parameter θ coded in a probability distribution $p_\theta(x)$ of a random variable x. This is known as the (classical) Cramér-Rao bound (CRB) [28, 29]. In the quantum mechanical context, θ parametrizes a density operator ρ_θ that describes the state of the system, and x is the random outcome of a measurement with $p_\theta(x)$ given by the Born rule $p_\theta(x) = \mathrm{Tr}[\Pi_x\rho_\theta]$. The operator Π_x is the element in the set $\{\Pi_x\}$ of positive operators that corresponds to outcome x of the measurement, with $\int dx\, \Pi_x = \mathbf{1}$. Optimization over all possible POVM measurements leads to an upper bound for the classical Fisher information, $F_c \leq F_q := \mathrm{tr}\rho_\theta L_\theta^2$, where the symmetric logarithmic derivative L_θ is defined via $\partial_\theta\rho_\theta = (L_\theta\rho_\theta + \rho_\theta L_\theta)/2$. The smallest uncertainty (standard deviation) of an unbiased estimator of θ is then bounded from below by the quantum Cramér–Rao bound (QCRB) [30–32]

$$\delta\theta \geq \frac{1}{\sqrt{QF_c(\rho_\theta)}} \geq \frac{1}{\sqrt{QF_q(\rho_\theta)}}, \quad (7)$$

where Q is the number of performed experiments. The optimal measurement is a projective measurement with POVM elements given by the projectors onto the eigenstates of L_θ, but these may not be realizable experimentally. It is therefore common to use the QCRB as a benchmark and check whether experimentally feasible measurements saturate it.

The interferometric scheme– We consider as input states separable, Gaussian states of the coupled physical modes $a_{1,2}$ with no initial dependence on G. Since the approximate Hamiltonian considered is at most quadratic in the quadratures, Gaussianity is preserved[1]. After initialising the input states at time $t = 0$, the two harmonic oscillators evolve in their traps and interact solely via the Newtonian potential for the duration of the experiment. The transformation from the $a_{1,2}$ modes to the $a_\pm$ modes acts as a beamsplitter, and the $a_\pm$ modes serve as the two arms of the interferometer, of which only the a_- arm acquires an additional phase that depends on G. At a time $t = t_f$ we close the interferometer by performing local projective Gaussian measurements on the physical modes of the oscillators $a_{1,2}$. By having two freely evolving modes with a phase accumulated between them that carries information on G, our interferometric setup differs from standard measurement schemes where only a single test mass evolves freely, and a source mass is driven [33, 34] or displaced with external forces [4, 35].

Input states– We employ the Gaussian formalism to parametrize initial states and solve the dynamics [36–39]. Gaussian states are parametrised entirely by the first moments $\mathbf{r}(t) = (x_1(t), p_1(t), x_2(t), p_2(t))^T$ and covariance matrix σ (CM) where $\sigma_{ij} = \frac{1}{2}\langle\{\hat{r}_i, \hat{r}_j\}\rangle - \langle\hat{r}_i\rangle\langle\hat{r}_j\rangle$, with $\{\cdot,\cdot\}$ the anti-commutator. The relevant parameters which enter into the CM are the squeezing parameters s_1, s_2 and thermal occupation number $\bar{n} = (\exp[\hbar\omega_0/k_bT] - 1)^{-1}$ [40] (see also the Appendices to the manuscript). Squeezed input states can be generated by first exciting the physical modes of the oscillators into coherent states and then modifying the trap frequencies. Explicitly, a mode of frequency $a_1(\omega_1)$ can be cast as the result of squeezing a different mode of frequency ω_0 according to the relation $a_1(\omega_0) = S^\dagger(s_1)a_1(\omega_1)S(s_1)$, with the squeezing operator $S(s_1) = \exp\left[\frac{1}{2}(s_1^* a_1^2(\omega_1) - s_1 a_1^{\dagger 2}(\omega_1))\right]$ and squeezing parameter $s_1 = \frac{1}{2}\log(\omega_0/\omega_1)$ [41]. Modifying only the

---

[1] This remains the case upon considering noise that can be modelled by a Lindblad master equation with jump operators at most linear in the quadratures.

frequency of the first mode $a_1(\omega_1) \to a_1(\omega_0)$ and initializing the $a_2(\omega_0)$ mode in the ground state, our input states for zero temperature read [cf. Appendices]

$$|\alpha_1\rangle_{a_1(\omega_1)}|0\rangle_{a_2(\omega_0)} = |\alpha_1, s_1\rangle_{a_1(\omega_0)}|0, 0\rangle_{a_2(\omega_0)}\,, \tag{8}$$

where $|\alpha\rangle_{a_i(\omega_i)} = D(\alpha)_{a_i(\omega)}|0\rangle_{a_i(\omega)}$ is a coherent state of the $a_i(\omega)$-mode, $|\alpha_i, s_i\rangle_{a_i(\omega)} = S(s_i)D(\alpha_i)_{a_i(\omega)}|0\rangle_{a_i(\omega)}$ is a squeezed coherent state of the $a_i(\omega)$-mode, and $D(\alpha)_{a_i(\omega)} = \exp[\alpha a_i^\dagger(\omega) - \alpha^* a_i(\omega)]$ is the displacement operator. The amplitudes of the coherent states are calculated through the input first moments [cf. Appendices]. We consider projective general-dyne measurements on both physical modes that are accounted for within the Gaussian formalism [36–39]. The CFI is associated to a projective local measurement obtained by modifying the covariance matrix as $\boldsymbol{\sigma}(t) \to \boldsymbol{\sigma}(t) + \boldsymbol{\sigma}_m$ [39]. The added term $\boldsymbol{\sigma}_m = \mathrm{Diag}\left[s, s^{-1}, s, s^{-1}\right]/2$ corresponds to projective measurements of the $a_1(\omega_0)$, $a_2(\omega_0)$ modes, with measurements of position ($s \to 0$) and momentum quadratures ($s \to \infty$), homodyne detection and balanced heterodyne detection ($s = 1$).

Results – We consider a possible experimental realization of the interferometric set-up with realistic parameters: two neodymium magnets with a density of $\varrho = 7430\,\mathrm{kg\,m^{-3}}$, levitated in superconducting traps, see Fig. 1. The magnets are taken to be perfect spheres of radius $r_{\mathrm{mass}} \approx 1.48\,\mathrm{mm}$, corresponding to a mass of $m = 1 \times 10^{-4}\mathrm{kg}$. The trap size is taken as $l_{\mathrm{trap}} = 4.9 \times 10^{-3}\,\mathrm{m}$, slightly smaller than the distance between the centers of motion $d = 5 \times 10^{-3}\mathrm{m}$. We assume $\omega_0 = 100\,\mathrm{rad s^{-1}}$, as trapping frequencies in the range $\sim 10 - 100\,\mathrm{Hz}$ have been experimentally achieved for levitated neodymium magnets [12, 14, 42]. Squeezed light experiments have yielded high squeezing parameters of up to $s \approx 1.73$, corresponding to 15 dB [43, 44]. Such large squeezing may, through the process of state transfer, be imparted onto mechanical systems [45]. Therefore, a squeezing parameter $s \in [-1.8, 1.8]$ was used in our analysis. With these values, we achieve a coupling parameter $\eta = 1.068 \times 10^{-11}$. A superconducting wall between the two magnets shields the electromagnetic forces. An experimental realization with similar scales to our set-up with just one levitated particle can be found in Ref. [8].

In order to increase the QFI, one may use large-amplitude input states. However, one must then consider the validity of the truncation of the gravitational potential in Eq. (3) to second order in δx. To third order in δx, the relative difference between Eq. (3) and the full expression in Eq. (2) is $D_{rel} = (x_1 - x_2)^3/d^3$. For $D_{rel} < 1 \times 10^{-3}$, and a maximum amplitude smaller than the center of mass separation, $|x_1 - x_2| < \lambda d$, the bound imposes $\lambda < 1/10$, and for $\lambda = 1/10$, with input oscillator amplitude $\langle x(0)\rangle = \lambda l_{\mathrm{trap}} < \lambda d$ we are well within the appropriate length-scales that justify the truncation in Eq. (3). Hence, in the following we fix the input amplitude[2] $\langle x_1(0)\rangle = l_{\mathrm{trap}}/10$, which implies a dimensionless input amplitude of the a_1 mode of $\alpha_1 \approx 3.374 \times 10^{12}$ [cf. Appendices]. Introducing larger amplitudes requires considering higher-order terms of the gravitational potential and would result in non-linear effects beyond the scopes of this work.

The results for projective measurements are shown in Fig. 2 **(a)** and **(b)**. Measurements of the position and momentum quadratures periodically saturate the QFI, winning out over heterodyne measurements. For long times, the t^2 term in the QFI dominates. With our given set of parameters, we see in Fig. 2 **(a)**-**(b)** that a projective momentum measurement performed at $t \approx 100\,\mathrm{s}$ saturates the QFI. This corresponds to a sensitivity of $\delta G \approx 1.31 \times 10^{-16}\,\mathrm{kg^{-1}m^3s^{-2}}$, or relative statistical error $\delta G/G \approx 1.96 \times 10^{-6}$, beating the current CODATA value of $\delta G/G \approx 2.2 \times 10^{-5}$ [1] by one order of magnitude. Performing a projective position measurement instead at $t = 10^5\,\mathrm{s}$, a sensitivity of $\delta G \approx 1.31 \times 10^{-19}$ is achieved, corresponding to a relative uncertainty of $\delta G/G \approx 1.96 \times 10^{-9}$, four orders of magnitude better than the CODATA standard uncertainty.

Due to the weakness of the gravitational coupling $(Gm/d^3\omega_0^2) \ll 1$, one may approximate the Hamiltonian in Eq. (5) by neglecting the terms involving a_i^2 and $a_i^{\dagger 2}$ $(i = 1, 2)$

$$H/\hbar \simeq \omega_0 a_+^\dagger a_+ + \omega_0(1 - \eta)a_-^\dagger a_-\,. \tag{9}$$

Coherent, separable initial states $|\alpha_1\rangle_{a_1(\omega_0)} \otimes |\alpha_2\rangle_{a_2(\omega_0)}$ evolving with Eq. (9) then yield a simple analytical expression for the QFI [46],

$$F_q(G) = 4(|\partial_\theta \alpha_1|^2 + |\partial_\theta \alpha_2|^2) = \frac{16m^2}{d^6\omega_0^2}\Delta^2 t^2, \tag{10}$$

where $\Delta = (\alpha_2 - \alpha_1)/\sqrt{2}$ parametrizes the differences in amplitude of the input states. Eq. (10) reproduces the leading behaviour of the exact result in Fig. 2. The t^2 scaling of the QFI and the corresponding $1/\sqrt{Q}t$ scaling for the QCRB are typical of coherent evolution. For our set of parameters, the prefactor in Eq. (10) is $16m^2\Delta^2/(d^6\omega_0^2) = 5.8 \times 10^{27}\mathrm{kg^2\,m^{-6}\ s^2}$, and leads to the very rapid increase of the QFI. Different from standard interferometric setups in quantum optics, we profit from direct access to the quadratures in the output ports rather than measuring the difference between the two output intensities. We see in Fig. 2 that the latter also leads to very rapid information gain, albeit only with half the rate compared to homodyne measurements. The CFI for intensity measurements can be calculated using the evolution described by Eq. (9) to be $F_c^{ph}(G) = F_q(G)/2$

---

[2] For the dimensionful position quadrature.

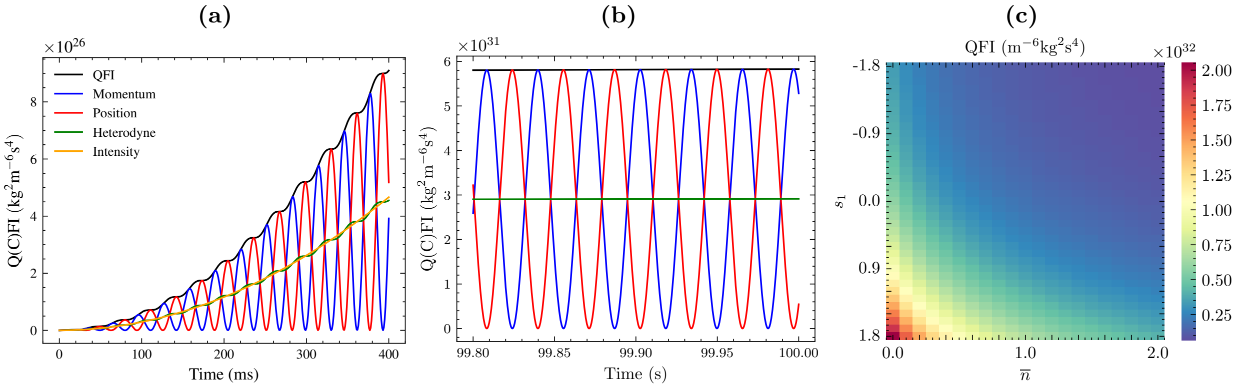

FIG. 2. QFI and CFI for different measurement schemes. **(a)** Black curve: Exact QFI calculated using the CM; Red curve: CFI for $s \to 0$ (Projective position measurement); Blue curve: CFI for $s \to \infty$ (Projective momentum measurement); Green curve: CFI for $s \to 1$ (Heterodyne measurement); Yellow curve: CFI for intensity measurement. **(b)** Same as in panel **(a)** but for longer times. In panels **(a)** and **(b)**, we took the input state $|\alpha_1, 0\rangle_{a_1(\omega_0)} \otimes |0, 0\rangle_{a_2(\omega_0)}$ with parameters $\omega_0 = 100$ rad s^{-1}, $m = 1 \times 10^{-4}$kg, $d = 5 \times 10^{-3}$m, $\alpha_1 \approx 3.374 \times 10^{12}$, $\alpha_2 = 0$, $\bar{n} = 0$. **(c)** QFI as a function of the squeezing s_1 and thermal occupation number $\bar{n}$ for a displaced squeezed thermal state at $t = 100$s. Other parameters as in panels **(a)** and **(b)**, where the input amplitude is defined through the initial displacement as $\langle x_i(0)\rangle = \sqrt{2}\alpha_i$.

[cf. Appendices]. Therefore, such measurements do not saturate the QCRB and are outperformed by homodyne measurements.

Thermal and squeezed states – We now consider more general Gaussian input states parametrized by their squeezing s_1, s_2, thermal occupation number $\bar{n}$, and first and second moments, as outlined before. For thermal and squeezed states the input amplitude is defined through the initial displacement $\langle x_i(0)\rangle = \sqrt{2}\alpha_i$. Fig. 2 **(c)** shows the impact of squeezing and the thermal occupation number $\bar{n}$ of the $a_1(\omega_0)$ mode of the input state on the QFI. Increasing $\bar{n}$ leads to reduced sensitivity at all times. Indeed, the QFI decays with the inverse of the thermal occupation number, $F_q(G) \propto (1 + 2\bar{n})^{-1}$, which implies $\delta G \propto (1 + 2\bar{n})^{1/2}$ [cf. Appendices]. Fig. 2 **(c)** shows this reduction at $t = 100$ s. Despite this reduction in sensitivity the QCRB remains saturable under projective position and momentum measurements in short and long time frames. For fixed temperature, squeezing of the $a_1(\omega_0)$'s momentum coordinate ($s_1 > 0$) leads to an increase of the value of the QFI at all times. For example, a squeezing parameter of $s_1 = 1.73$ and thermal occupation $\bar{n} = 0$ achieves a relative uncertainty $\delta G/G \approx 1.08 \times 10^{-6}$ at $t = 100s$, approximately a two-fold improvement over the unsqueezed state. Comparable gains are present at all times. In contrast, squeezing the position coordinate ($s_1 < 0$) decreases the QFI at all times, reducing the achievable sensitivity compared to the unsqueezed case. When the input state of the a_1 mode is chosen in such a way that $\langle p_1(0)\rangle = \sqrt{2}\alpha_1$ and $\langle x_1(0)\rangle = 0$, then the behavior is inverted, such that squeezing of the position coordinate ($s_1 < 0$) gives a two-fold improvement for all times.

Effects of damping– The effect of damping on the sensitivity of the system is considered with respect to currently realistic experimental set-ups, where quality factors $\mathcal{Q} = \omega/\gamma$ of order $\mathcal{Q} \approx 10^7$ have been achieved [12, 14, 42, 47]. The QFI reaches a maximum at finite time and decays to very small values for long times, see Fig. 3, limiting the t^2 scaling of the QFI to shorter and shorter times for decreasing Q. Under damping, the QFI scales as $F_q^\gamma(G,\gamma) \approx F_q(G)e^{-\gamma t}$. The preparation of separable coherent states achieves max $F_q^\gamma(G,\gamma) = \frac{64m^2\Delta^2}{d^6\omega^2\gamma^2e^2}$ at $t_{\max} = 2/\gamma$. With our choice of parameters and $\mathcal{Q} = 10^7$, the minimum relative standard uncertainty is

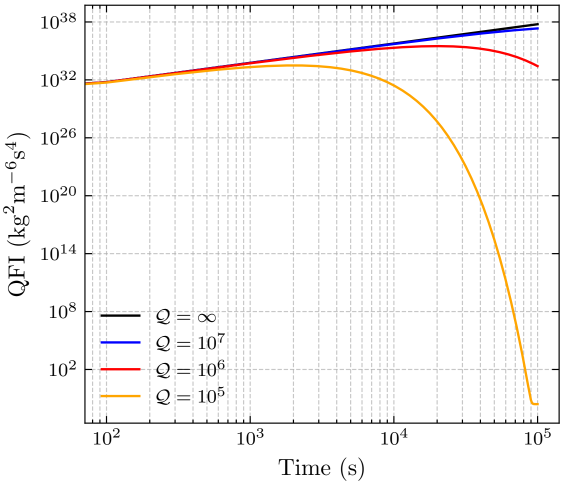

FIG. 3. QFI against time for different values of the $\mathcal{Q}$ factor (see the plot legend). All curves shown are for the input state $\rho = |\alpha_1, 0\rangle_{a_1(\omega_0)} \otimes |0, 0\rangle_{a_2(\omega_0)}$ with parameters $\omega_0 = 100$ rad s^{-1}, $m = 1 \times 10^{-4}$ kg, $d = 5 \times 10^{-3}$ m, $\alpha_1 \approx 3.374 \times 10^{12}$, $\alpha_2 = 0$, $\bar{n} = 0$.

$\delta G_{\min}/G \approx 2.67 \times 10^{-9}$, gaining four orders of magnitude over the current CODATA value in approximately 2.3 days. For $\mathcal{Q} = 10^5$ ($\gamma = 10^{-3}\,\mathrm{s}^{-1}$) the QFI goes to almost zero after approximately 10^5 s. The other curves for which $\gamma \neq 0$ show similar behavior, however at a much longer time scale. For shorter time frames, the effect of damping is minimal.

Conclusions– We have shown that coupled levitated mechanical oscillators offer themselves as a platform for an interferometric measurement of Newton's constant G, theoretically beating the current standard uncertainty by four orders of magnitude with a measurement time of about a day. With additional squeezing in one input mode, it is possible to gain further improvements in the sensitivity, also at finite temperature. Although mass estimation and other experimental factors will make it challenging to achieve these levels of sensitivity, our results, together with the rapid progress of experimental implementations, motivate the use of these systems for quantum metrology of small gravitational effects, and, more generally, for the exploration of the boundary between gravitational physics and quantum mechanics.

Acknowledgements – We thank Emre Köse, Hendrik Ulbricht, Albert Cabot, Paulo J Paulino, Adriano Braga Barreto, and Fabian Müller for fruitful discussions. We acknowledge the EU EIC Pathfinder project QuCoM (101046973). MP acknowledges financial support from the UK funding agency EPSRC (grant EP/T028424/1), the Royal Society Wolfson Fellowship (RSWF/R3/183013), the Department for the Economy of Northern Ireland under the US-Ireland R&D Partnership Programme, the “Italian National Quantum Science and Technology Institute (NQSTI)” (PE0000023) - SPOKE 2 through project ASpEQCt, and the “National Centre for HPC, Big Data and Quantum Computing (HPC)” (CN00000013) – SPOKE 10 through project HyQELM.

[1] E. Tiesinga, P. Mohr, D. Newell, and B. Taylor, Reviews of Modern Physics **93**, 025010 (2021).

[2] G. T. Gillies, Reports on Progress in Physics **60**, 151 (1997).

[3] A. Bertoldi, G. Lamporesi, L. Cacciapuoti, M. De Angelis, M. Fattori, T. Petelski, A. Peters, M. Prevedelli, J. Stuhler, and G. M. Tino, The European Physical Journal D **40**, 271 (2006).

[4] J. B. Fixler, G. T. Foster, J. M. McGuirk, and M. A. Kasevich, Science **315**, 74 (2007).

[5] G. Rosi, F. Sorrentino, L. Cacciapuoti, M. Prevedelli, and G. M. Tino, Nature **510**, 518 (2014).

[6] R. Newman, M. Bantel, E. Berg, and W. Cross, Philosophical Transactions of the Royal Society A: Mathematical, Physical and Engineering Sciences **372**, 20140025 (2014).

[7] Q. Li, C. Xue, J.-P. Liu, J.-F. Wu, S.-Q. Yang, C.-G. Shao, L.-D. Quan, W.-H. Tan, L.-C. Tu, Q. Liu, H. Xu, L.-X. Liu, Q.-L. Wang, Z.-K. Hu, Z.-B. Zhou, P.-S. Luo, S.-C. Wu, V. Milyukov, and J. Luo, Nature **560**, 582 (2018).

[8] A. Vinante, C. Timberlake, and H. Ulbricht, Entropy **24**, 1642 (2022).

[9] J. Prat-Camps, C. Teo, C. Rusconi, W. Wieczorek, and O. Romero-Isart, Physical Review Applied **8**, 034002 (2017).

[10] C. Gonzalez-Ballestero, M. Aspelmeyer, L. Novotny, R. Quidant, and O. Romero-Isart, Science **374**, eabg3027 (2021).

[11] S. Bose, I. Fuentes, A. A. Geraci, S. M. Khan, S. Qvarfort, M. Rademacher, M. Rashid, H. Ulbricht, and C. C. Wanjura, arXiv:2311.09218 (2023).

[12] T. M. Fuchs, D. Uitenbroek, J. Plugge, N. van Halteren, A. Vinante, H. Ulbricht, and T. H. Oosterkamp, arXiv:2303.03545 (2023).

[13] C. Timberlake, G. Gasbarri, A. Vinante, A. Setter, and H. Ulbricht, Applied Physics Letters **115**, 224101 (2019).

[14] A. Vinante, P. Falferi, G. Gasbarri, A. Setter, C. Timberlake, and H. Ulbricht, Physical Review Applied **13**, 064027 (2020).

[15] T. Westphal, H. Hepach, J. Pfaff, and M. Aspelmeyer, Nature **591**, 225 (2021).

[16] R. Kaltenbaek, G. Hechenblaikner, N. Kiesel, O. Romero-Isart, K. C. Schwab, U. Johann, and M. Aspelmeyer, Experimental Astronomy **34**, 123 (2012).

[17] A. Belenchia, R. M. Wald, F. Giacomini, E. Castro-Ruiz, t. Brukner, and M. Aspelmeyer, Physical Review D **98**, 126009 (2018).

[18] T. Weiss, M. Roda-Llordes, E. Torrontegui, M. Aspelmeyer, and O. Romero-Isart, Phys. Rev. Lett **127**, 023601 (2021).

[19] J. D. Teufel, T. Donner, D. Li, J. H. Harlow, M. S. Allman, K. Cicak, A. J. Sirois, J. D. Whittaker, K. W. Lehnert, and R. W. Simmonds, “Sideband Cooling Micromechanical Motion to the Quantum Ground State,” (2011).

[20] J. Chan, T. P. M. Alegre, A. H. Safavi-Naeini, J. T. Hill, A. Krause, S. Gröblacher, M. Aspelmeyer, and O. Painter, Nature **478**, 89 (2011).

[21] B. Abbott *et al.*, New Journal of Physics **11**, 073032 (2009).

[22] A. Youssefi, S. Kono, M. Chegnizadeh, and T. J. Kippenberg, Nature Physics **19**, 1697 (2023).

[23] U. Delic, M. Reisenbauer, K. Dare, D. Grass, V. Vuletic, N. Kiesel, and M. Aspelmeyer, Science **367**, 892 (2020).

[24] C. Wang, L. Banniard, K. Børkje, F. Massel, L. Mercier De Lépinay, and M. A. Sillanpää, Nature Communications **15**, 7395 (2024).

[25] J.-M. Pirkkalainen, E. Damskägg, M. Brandt, F. Massel, and M. A. Sillanpää, Physical Review Letters **115**, 243601 (2015).

[26] E. E. Wollman, C. U. Lei, A. J. Weinstein, J. Suh, A. Kronwald, F. Marquardt, A. A. Clerk, and K. C. Schwab, Science **349**, 952 (2015).

[27] F. Lecocq, J. B. Clark, R. W. Simmonds, J. Aumentado, and J. D. Teufel, Physical Review X **5**, 041037 (2015).

[28] C. R. Rao, Bull. Calcutta Math. Soc. **37**, 81 (1945).

[29] H. Cramér, *Mathematical Methods of Statistics* (Princeton University Press, Princeton, NJ, 1946).

[30] C. W. Helstrom, J. Stat. Phys. **1**, 231 (1969).

[31] A. S. Holevo, *Probabilistic and Statistical Aspect of Quan-*

tum Theory (North-Holland, Amsterdam, 1982).

[32] S. L. Braunstein and C. M. Caves, Physical Review Letters **72**, 3439 (1994).

[33] C. D. Hoyle, D. J. Kapner, B. R. Heckel, E. G. Adelberger, J. H. Gundlach, U. Schmidt, and H. E. Swanson, Physical Review D **70**, 042004 (2004).

[34] D. J. Kapner, T. S. Cook, E. G. Adelberger, J. H. Gundlach, B. R. Heckel, C. D. Hoyle, and H. E. Swanson, Physical Review Letters **98**, 021101 (2007).

[35] H. Cavendish, Philosophical Transactions of the Royal Society of London **88**, 469 (1997).

[36] A. Ferraro, S. Olivares, and M. G. A. Paris, "Gaussian states in continuous variable quantum information," (2005), arXiv:quant-ph/0503237.

[37] M. G. Genoni, L. Lami, and A. Serafini, Contemporary Physics **57**, 331 (2016).

[38] O. Pinel, J. Fade, D. Braun, P. Jian, N. Treps, and C. Fabre, Physical Review A **85**, 010101 (2012).

[39] S. McMillen, M. Brunelli, M. Carlesso, A. Bassi, H. Ulbricht, M. G. A. Paris, and M. Paternostro, Physical Review A **95**, 012132 (2017).

[40] T. Krisnanda, G. Y. Tham, M. Paternostro, and T. Paterek, npj Quantum Information **6**, 12 (2020).

[41] R. Graham, Journal of Modern Optics **34**, 873 (1987).

[42] C. Timberlake, E. Simcox, and H. Ulbricht, Phys. Rev. Research **6**, 033345 (2024).

[43] H. Vahlbruch, M. Mehmet, N. Lastzka, B. Hage, S. Chelkowski, A. Franzen, S. Gossler, K. Danzmann, and R. Schnabel, Physical Review Letters **100**, 033602 (2008).

[44] H. Vahlbruch, M. Mehmet, K. Danzmann, and R. Schnabel, Physical Review Letters **117**, 110801 (2016).

[45] M. Aspelmeyer, T. J. Kippenberg, and F. Marquardt, Reviews of Modern Physics **86**, 1391 (2014).

[46] F. Müller, E. Köse, A. J. Meixner, E. Schäffer, and D. Braun, "Pushing the Boundaries: Interferometric Mass Photometry at the Quantum Limit of Sensitivity," (2024).

[47] J. Vovrosh, M. Rashid, D. Hempston, J. Bateman, M. Paternostro, and H. Ulbricht, Journal of the Optical Society of America B **34**, 1421 (2017).

Appendix A: Input Amplitudes

For a coherent state, the expectation value of the position and momentum are proportional to the state's amplitude $\langle x\rangle = \sqrt{\frac{\hbar}{2m\omega}}(\alpha+\alpha^*)$, $\langle p\rangle = -i\sqrt{\frac{\hbar m\omega}{2}}(\alpha-\alpha^*)$, where x and p are dimensionful. As such

$$\alpha = \sqrt{\frac{m\omega}{2\hbar}}\langle x(t)\rangle + i\sqrt{\frac{1}{2\hbar m\omega}}\langle p(t)\rangle. \tag{11}$$

If we assume at $t=0$ that the expectation value of the momentum $\langle p(0)\rangle = 0$, then the input amplitude can be calculated to be

$$\alpha = \sqrt{\frac{m\omega}{2\hbar}}\langle x(0)\rangle. \tag{12}$$

Assuming $\omega = 100\,\mathrm{rad\,s^{-1}}$, $m = 1\times10^{-4}\,\mathrm{kg}$ and a trap of size $l_{trap} = 4.9\times10^{-3}\,\mathrm{m}$ with oscillatory amplitude of $l_{\mathrm{trap}}/10$, then $\alpha \approx 3.374\times10^{12}$. For thermal and squeezed states, the input amplitude is similarly defined through the initial displacement, such that $\langle x_i(0)\rangle = \sqrt{\dfrac{2\hbar}{m\omega}}\alpha_i$.

Appendix B: States and Evolution

In this section we lay out the framework of the Gaussian evolution of our coupled oscillators. Much is borrowed from [37]. In continuous variable systems we promote the dimensionless quadratures to operators $\hat{x}_i$ and $\hat{p}_i$, for $i = 1,\dots,n$, which if combined to form the vector $\hat{\mathbf{r}} = (\hat{x}_1,\hat{p}_1,\dots,\hat{x}_n,\hat{p}_n)^T$, satisfy the commutation relations:

$$[\hat{r}_i,\hat{r}_j] = i\Omega_{ij}, \tag{13}$$

where $i,j = 1,\dots,2n$ and Ω is the symplectic form, usually defined as

$$\Omega = \bigoplus_{j=1}^{n}\omega, \quad \text{where} \quad \omega = \begin{pmatrix} 0 & 1 \\ -1 & 0 \end{pmatrix}. \tag{14}$$

The implementation of the symplectic matrix follows naturally from the commutation relations $[\hat{x}_i,\hat{p}_j] = i\delta_{ij}$. In general, Gaussian Hamiltonians are at most quadratic in the canonical operators. A general Hamiltonian for Gaussian evolution may be written:

$$\hat{H} = \frac{1}{2}\hat{\mathbf{r}}^T H\hat{\mathbf{r}} + \hat{\mathbf{r}}^T\mathbf{r}_H, \tag{15}$$

where $\mathbf{r}_H$ is comprised of the linear coefficients. We wish to study the evolution of our Gaussian states utilizing the Heisenberg evolution for canonical operators. The covariance matrix $\boldsymbol{\sigma}$ (CM) is defined as

$$\sigma_{ij} = \frac{1}{2}\langle\{\hat{r}_i,\hat{r}_j\}\rangle - \langle\hat{r}_i\rangle\langle\hat{r}_j\rangle, \tag{16}$$

with $\{\cdot,\cdot\}$ the anti-commutator. The CM is a positive semi-definite $2n\times2n$ matrix satisfying the Robertson-Schrödinger uncertainty relations

$$\boldsymbol{\sigma} + \frac{i}{2}\Omega \geq 0. \tag{17}$$

In order to preserve Gaussianity the Hamiltonian of the system can be at most quadratic in the quadratures while the jump operators in the Lindblad master equation, describing the open dynamics of the system, can be at most linear in the quadratures.

Appendix C: Quantum Fisher Information - Covariance Matrix Formulation

For a probability distribution $p_\theta(x)$ dependent on a parameter θ which we wish to estimate, the classical Fisher

Information (CFI) can be written as:

$$F_c(\theta) = \int_{\mathbb{R}} dx p_\theta(x) \left(\frac{\partial \ln p_\theta(x)}{\partial\theta}\right)^2 . \tag{18}$$

For a quantum Gaussian state the CFI takes the rather simple form:

$$F_c(\boldsymbol{r}_\theta, \boldsymbol{\sigma}_{\theta m}) = (\langle \boldsymbol{r}'_\theta \rangle)^T \boldsymbol{\sigma}_{\theta m}^{-1} \langle \boldsymbol{r}'_\theta \rangle + \frac{1}{2}\mathrm{Tr}\left((\boldsymbol{\sigma}'_{\theta m}\boldsymbol{\sigma}_{\theta m}^{-1})^2\right) , \tag{19}$$

where $\sigma_{\theta m}$ is the covariance matrix of the system after performing a measurement. The Quantum Fisher Information (QFI) represents the maximum amount of accessible information about the parameter θ which can be extracted from the state. The Quantum Fisher information for Gaussian states can be expressed as [38]:

$$F_q(\rho_\theta) = (\langle \boldsymbol{r}'_\theta \rangle)^T \boldsymbol{\sigma}_\theta^{-1} \langle \boldsymbol{r}'_\theta \rangle + \frac{1}{2(1+P^2)}\mathrm{Tr}\left((\boldsymbol{\sigma}'_\theta \boldsymbol{\sigma}_\theta^{-1})^2\right) , \tag{20}$$

where $\langle \boldsymbol{r}' \rangle$ denotes derivative of the column vector of expectation values for the first moments with respect to the parameter θ and $\boldsymbol{\sigma}$ is again the covariance matrix. Generally, the best achievable sensitivity of an unbiased estimator of a parameter θ is bounded from bellow by the Quantum Cramér–Rao bound:

$$\delta\theta \geq \delta\theta_{\min} = \frac{1}{\sqrt{QF_q(\rho_\theta)}}, \tag{21}$$

where Q is the number of performed experiments and $P = (\det(\sigma_\theta))^{-1/2}$ is the purity of the state, which we note has has no parameter dependence for our system. Whilst the QCRB gives us the best achievable sensitivity over all unbiased estimators and all POVM measurements, it is important to ask which types of measurements saturate this bound.

In the main text, we evaluate the CFI whilst restricting to local Gaussian measurements on both of our modes. An example of such a measurement can be described by a POVM with elements restricted to a pure two-mode Gaussian state with covariance matrix $\sigma_m = \mathrm{diag}[s, s^{-1}, s, s^{-1}]$, where $s \in [0, \infty]$ parameterises the degree of squeezing of the elements of the POVM. If such a measurement is performed on a state $\sigma(t)$, the best achievable sensitivity of the measurement is given by the CFI in Eq. (19) with the covariance matrix $\sigma(t) + \sigma_m$ [39].

Appendix D: General Evolution

As our full Hamiltonian in Eq. (4) is truncated to be at most quadratic in order, it maps Gaussian states to Gaussian states. As a Gaussian state is fully determined by its first moments and the covariance matrix, we are able to determine the full evolution of the system by determining the evolution of these two quantities. Here we follow the derivation in Refs. [37, 40]. We begin by recasting Eq. (4) in dimensionless form through the rescaling transformations $x_i \to \sqrt{\hbar/m\omega_0}x_i$ and $p_i \to \sqrt{\hbar m\omega_0}p_i$

$$H/\hbar = \sum_{i=1,2} \frac{1}{2}\omega_0 \left(p_i^2 + \left(1 - \frac{2Gm}{d^3\omega_0^2}\right) x_i^2\right) - \frac{Gm^2}{\sqrt{d^4\hbar m\omega_0}}x_1 + \frac{Gm^2}{\sqrt{d^4\hbar m\omega_0}}x_2 + \frac{2Gm}{d^3\omega_0}x_1 x_2 . \tag{22}$$

The Langevin equations of motion of for the dimensionless quadratures read

$$\begin{aligned}
\dot{x}_1 &= \omega_0 p_1, \\
\dot{x}_2 &= \omega_0 p_2, \\
\dot{p}_1 &= -\omega_0 \left(1 - \frac{2Gm}{d^3\omega_0^2}\right) x_1 - \frac{2Gm}{d^3\omega_0}x_2 - \gamma p_1 + \nu, \\
\dot{p}_2 &= -\omega_2 \left(1 - \frac{2Gm}{d^3\omega_0^2}\right) x_2 - \frac{2Gm}{d^3\omega_0}x_1 - \gamma p_2 - \nu,
\end{aligned} \tag{23}$$

where we have introduced a phenomenological damping rate γ and defined $\nu = Gm^2/\sqrt{\hbar m\omega_0 d^4}$. Eqs. (23) may be expressed in matrix form as $\dot{\hat{\boldsymbol{r}}}(t) = K\hat{\boldsymbol{r}}(t) + \mathbf{I}(t)$ with the drift matrix

$$K = \begin{pmatrix} 0 & \omega_0 & 0 & 0 \\ -\omega_0\left(1 - \frac{2Gm}{d^3\omega_0^2}\right) & -\gamma & -\frac{2Gm}{d^3\omega_0} & 0 \\ 0 & 0 & 0 & \omega_0 \\ -\frac{2Gm}{d^3\omega_0} & 0 & -\omega_0\left(1 - \frac{2Gm}{d^3\omega_0^2}\right) & -\gamma \end{pmatrix}, \tag{24}$$

and where we have introduced the vector $\mathbf{I}(t) = \boldsymbol{v}(t) + \boldsymbol{\kappa}$, which is comprised of the noise term $\boldsymbol{v}(t) = (0, \xi_1(t), 0, \xi_2(t))^T$ and the constant term $\boldsymbol{\kappa} = (0, \nu_1, 0, -\nu_2)^T$. The solutions to the Langevin equations are given by [40]

$$\boldsymbol{r}(t) = W_+(t)\boldsymbol{r}(0) + W_+ \int_0^t dt' W_-(t')\mathbf{I}(t'), \tag{25}$$

where $W_\pm(t) = \exp(\pm Kt)$ are evolution matrices. The dynamics of the covariance matrix is governed by the expression

$$\dot{\boldsymbol{\sigma}} = K\boldsymbol{\sigma} + \boldsymbol{\sigma}K^T + D, \tag{26}$$

where $D = \mathrm{Diag}[0, \gamma(2\bar{n}+1), 0, \gamma(2\bar{n}+1)]$is the diffusion matrix describing the coupling of the system to the environment [37], $\bar{n} = (\exp(\hbar\omega/k_B T) - 1)^{-1}$ is the thermal occupation number, and T the temperature of the environment. The solutions to Eq. (26) are of the form

$$\begin{aligned}\boldsymbol{\sigma}(t) = {} & W_+(t)\boldsymbol{\sigma}(0)W_+^T(t) \\ & + W_+(t)\int_0^t dt' W_-(t')DW_-^T(t')DW_+^T(t),\end{aligned} \tag{27}$$

which, upon integration, gives us the linear equation

$$\begin{aligned}K\boldsymbol{\sigma}(t) + \boldsymbol{\sigma}(t)K^T = & - D + KW_+(t)\boldsymbol{\sigma}(0)W_+^T(t) \\ & + W_+(t)\boldsymbol{\sigma}(0)W_+^T(t)K^T \\ & + W_+(t)DW_+(t)^T.\end{aligned} \tag{28}$$

Appendix E: Initial State Parameterisation

We consider an uncorrelated input state of the oscillators. In this case, the covariance matrix takes the block-diagonal form

$$\boldsymbol{\sigma}(0) = \begin{pmatrix} \boldsymbol{\sigma}_1 & 0 \\ 0 & \boldsymbol{\sigma}_2 \end{pmatrix}, \tag{29}$$

where $\boldsymbol{\sigma}_{1(2)}$ is the covariance matrix for the first (second) oscillator respectively. Through local symplectic transformations, each of them can be cast in the form

$$\boldsymbol{\sigma}_i(\bar{n}, s) = \begin{pmatrix} \frac{1}{2}(2\bar{n}+1)e^{s_i} & 0 \\ 0 & \frac{1}{2}(2\bar{n}+1)e^{-s_i} \end{pmatrix}, \tag{30}$$

which is paparameterized through the local thermal excitation number $\bar{n}_i$ and degree of squeezing s_i (i=1,2).

Appendix F: Quantum Fisher Information from Coherent Amplitudes

We note that Eq. (3) contains the term $\frac{Gm^2}{d^2}(x_1 - x_2)$, which displaces the ground state creating a coherent state that evolves under the remainder of the Hamiltonian. For completeness, we include here the contribution of this displacement in the derivation of the QFI. A suitable change of coordinates allows us to discard such displacement. This is the approach taken in the main text, addressing the situation where both oscillators are in equilibrium positions, including the action of gravity, and then one oscillator is excited. However, one might also envisage situations where one has access to the shift of equilibrium positions due to gravity, e.g. by bringing the mass in from positions where they are far apart. As the Hamiltonian is at most quadratic, it maps coherent states to coherent states. Thus, we can calculate the QFI through the amplitudes of the aforementioned induced coherent states. We begin by translating our Hamiltonian into the coordinate basis of the normal modes $x_\pm = \frac{1}{\sqrt{2}}(x_2 \pm x_1)$, $p_\pm = \frac{1}{\sqrt{2}}(p_2 \pm p_1)$. The position and momentum operators may be expressed as the sum of these operators as

$$x_\pm = \frac{1}{\sqrt{2}}(a_\pm + a_\pm^\dagger), \quad p_\pm = -\frac{i}{\sqrt{2}}(a_\pm - a_\pm^\dagger). \tag{31}$$

In the normal basis, the quadratic terms of the Hamiltonian diagonalise, with only a linear term remaining:

$$H/\hbar = \frac{1}{2}\omega_0(p_+^2 + x_+^2 + p_-^2 + (1-2\eta)x_-^2) + \sqrt{2}\nu x_-. \tag{32}$$

Recasting again in terms of the creation and annihilation operators of the normal modes in Eq. (31), we get

$$\begin{aligned}H/\hbar = \frac{1}{2}\omega_0\Big[& (a_+^\dagger a_+ + a_+ a_+^\dagger) + (1-\eta)(a_-^\dagger a_- + a_- a_-^\dagger) \\ & - \eta(a_-^2 + (a_-^\dagger)^2)\Big] + \nu(a_- + a_-^\dagger).\end{aligned} \tag{33}$$

Rotating Wave Approximation – Due to the weakness of the gravitational coupling $Gm/(d^3\omega^2) \ll 1$ we are able to make an approximation in which the a^2, $(a^\dagger)^2$ terms are neglected (sometimes called "rotating wave approximation" (RWA), even though here no resonance phenomenon is involved): Transforming into the corotating frame, we see that the a^2, $(a^\dagger)^2$ terms are fast oscillating and, as such, can be disregarded. This is also justified a posteriori by a comparison of the exact QFI and the QFI using the Hamiltonian in Eq. (9) that can be seen in Fig. 4. The resulting Hamiltonian reads

$$H/\hbar \approx \omega_0 a_+^\dagger a_+ + \omega_0(1-\eta)a_-^\dagger a_- + \nu(a_- + a_-^\dagger). \tag{34}$$

In order to deal with the linear term, we redefine our a_- mode via a linear translation, sending $a_- \to b \equiv a_- + \kappa$, where $\kappa = \nu/(\omega_0(1-\eta))$. The Hamiltonian becomes completely diagonal: $H/\hbar = \omega_0 a_+^\dagger a_+ + \omega_0(1-\eta)b^\dagger b$. We may easily translate between coherent states of the $a_{1/2}$ modes and the $a_\pm$ modes

$$|\alpha\rangle_{a_1}|\beta\rangle_{a_2} = |(\alpha+\beta)/\sqrt{2}\rangle_{a_+}|(\beta-\alpha)/\sqrt{2}\rangle_{a_-}, \tag{35}$$

$$|\mu\rangle_{a_+}|\nu\rangle_{a_-} = |(\mu-\nu)/\sqrt{2}\rangle_{a_1}|(\mu+\nu)/\sqrt{2}\rangle_{a_2}, \tag{36}$$

where the lower index refers to the operator which defines the ground state. The ground state of a_- is a coherent state of the b mode with amplitude κ. Explicitly, we have $|0\rangle_{a_-} = |\kappa\rangle_b$ and $|0\rangle_b = |-\kappa\rangle_{a_-}$. Furthermore we may translate coherent states of a_- into their corresponding coherent state in b, $|\alpha\rangle_{a_-} \approx |\alpha+\kappa\rangle_b$, where we have discarded the phase factor. The state evolves

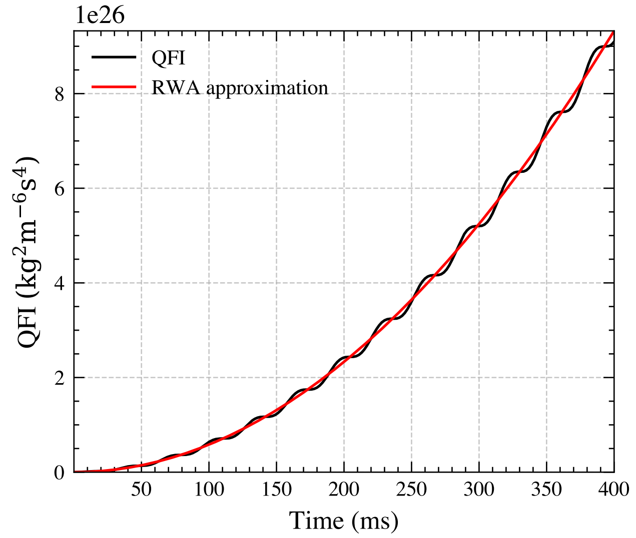

FIG. 4. Comparison of the exact QFI (Black) and the approximation Eq. (10), which utilises the corotating frame for input state $\rho = |\alpha_1, 0\rangle_{a_1(\omega_0)} \otimes |0, 0\rangle_{a_2(\omega_0)}$ with parameters $\omega_0 = 100\,\mathrm{rad\ s}^{-1}$, $m = 1 \times 10^{-4}\,\mathrm{kg}$, $d = 5 \times 10^{-3}\,\mathrm{m}$, $\alpha_1 \approx 3.374 \times 10^{12}$, $\alpha_2 = 0$, $\bar{n} = 0$.

correspondingly as

$$e^{-iHt/\hbar}|\alpha\rangle_{a_1}|\beta\rangle_{a_2} = \left| e^{-i\omega_0 t}\frac{\alpha+\beta}{\sqrt{2}} \right\rangle_{a_+} \otimes \left| e^{-i\omega_0(1-\eta)t}\left(\frac{\beta-\alpha}{\sqrt{2}} + \kappa\right) - \kappa \right\rangle_{a_-}. \tag{37}$$

For coherent states, the QFI is given to be the absolute value squared of the derivative of the amplitude with respect to the parameter we wish to measure. For the product of two coherent states $|\alpha\rangle \otimes |\beta\rangle$ the QFI is $F_q(\theta) = 4(|\partial_\theta \alpha|^2 + |\partial_\theta \beta|^2)$. The G dependence of the state in Eq. (37) is coded entirely in the a_- mode. Inserting the amplitudes of Eq. (37) into the expression of the QFI for a coherent state

$$F_q(G) = 4\left|\partial_G \left(e^{-i\omega_0(1-\eta)t}\,(\Delta + \kappa) - \kappa\right)\right|^2, \tag{38}$$

where $\Delta = (\beta - \alpha)/\sqrt{2}$ parameterises the amplitude of the input state of the a_- mode. For longer time scales the t^2 terms come to dominate the dynamics, leading to a divergence of the QFI for $t \to \infty$ and a $1/\sqrt{N}t$ scaling for the Quantum Cramér–Rao bound,

$$F_q(G) = \cdots + 16\left(\frac{Gm^{5/2}}{d^2\sqrt{\omega_0\hbar}\,(d^3\omega_0^2 - 2Gm)} + \frac{m}{d^3\omega_0}\Delta\right)^2 t^2. \tag{39}$$

where we have used $\eta = 2Gm/d^3\omega_0^2$, $\kappa = \nu/(\omega_0(1-\eta))$ and $\nu = Gm^2/\sqrt{\hbar m\omega_0 d^4}$. If we do not consider the shift in the equilibrium position, then this further reduces to

$$F_q(G) = 16\left(\frac{m}{d^3\omega_0}\Delta\right)^2 t^2. \tag{40}$$

CFI of Intensity Measurement.

For a coherent state $|\beta\rangle$, the CFI associated with an intensity measurement is [46]

$$F_{int}(\theta) = 4\mathrm{Re}\left[\frac{\beta^*}{|\beta|}\frac{\partial\beta}{\partial\theta}\right]^2. \tag{41}$$

In quantum optics the intensity measurement would correspond to photon counting. For the mechanical oscillators considered here, it can be achieved by measuring the energy of the oscillators, which in turn can be achieved by measuring the amplitude $x_{\max}$ and frequency of the oscillations, knowing the mass of the oscillators. From this one gets the potential energy $m\omega^2 x_{\max}^2/2$ at times when the kinetic energy vanishes and hence total energy equals the potential energy. For a product state of m coherent states $|\Phi\rangle = |\beta_1\rangle \otimes \cdots \otimes |\beta_m\rangle$, the CFI is the sum of the CFI of each mode

$$F_c^{ph}(\theta) = 4\sum_{i=1}^{m}\left(\mathrm{Re}\left[\frac{\beta_i^*}{|\beta_i|}\frac{\partial\beta_i}{\partial\theta}\right]\right)^2. \tag{42}$$

To prove this, we use $p_\theta(n) = |\langle n|\beta\rangle|^2 = e^{-|\beta_\theta|^2}\frac{(|\beta_\theta|^2)^n}{n!}$ to get

$$\frac{\partial p_\theta(n)}{\partial\theta} = -e^{-|\beta_\theta|^2}\frac{\partial|\beta|^2}{\partial\theta}\frac{(|\beta_\theta|^2)^n}{n!} + e^{-|\beta_\theta|^2}\frac{\partial|\beta|^2}{\partial\theta}\frac{(|\beta_\theta|^2)^{n-1}}{(n-1)!} \tag{43}$$

The calculation of the CFI for the photon resolving measurement on a single mode leads to

$$\begin{aligned} F_c^{ph}(\theta) &= \sum_n \frac{1}{p_\theta(n)}\left(\frac{\partial p_\theta(n)}{\partial\theta}\right)^2 = \sum_n e^{-|\beta_\theta|^2}\left(\frac{\partial|\beta_\theta|^2}{\partial\theta}\right)^2\left(\frac{|\beta_\theta|^{2n}}{n!} - 2\frac{|\beta_\theta|^{2(n-1)}}{(n-1)!} + \frac{n!(|\beta_\theta|^{2(n-2)})}{(n-1)!^2}\right) \\ &= e^{-|\beta_\theta|^2}\left(\frac{\partial|\beta_\theta|^2}{\partial\theta}\right)^2\left[e^{|\beta_\theta|^2} - 2e^{|\beta_\theta|^2} + e^{|\beta_\theta|^2}\left(1 + \frac{1}{|\beta_\theta|^2}\right)\right] = 4\mathrm{Re}\left[\frac{\beta^*}{|\beta|}\frac{\partial\beta}{\partial\theta}\right]^2. \end{aligned} \tag{44}$$

This can then be extended in a straightforward manner to a product state of m modes [46]. By disregarding the constant shift κ, we express Eq. (37) in terms of the physical modes a_1 and a_2, and calculate the CFI for intensity measurements on them. After a simple calculation one arrives at the approximate expression for the CFI relating to intensity measurements,

$$F_c^{ph}(G) = 8\left(\frac{m}{d^3\omega_0}\Delta\right)^2 t^2. \tag{45}$$

For our system, the output physical modes of the interferometer, remain in a product state of coherent states, $|\alpha(1+e^{-i\omega_0(1-\eta)t})/2\rangle_{a_1}|\alpha(1+e^{-i\omega_0(1-\eta)t})/2\rangle_{a_2}$ which follows from Eq. (37) (modulo shift of κ in the equilibrium positions). Straightforward calculations using Eq. (42) yield $F_c^{ph}(G) = 8\frac{m^2}{d^6\omega_0^2}\Delta^2 t^2$.

7.2 Second publication

Magnetic Dipole Trapping Potential between Infinite Superconducting Plates

Francis J. Headley[1, *]
[1] *Institut für Theoretische Physik, Eberhard-Karls-Universität Tübingen, 72076 Tübingen, Germany*

(Dated: July 2, 2025)

We derive the exact analytic form of the potential experienced by a magnetic dipole trapped between two infinite parallel superconducting plates using the method of image dipoles, providing a benchmark for numerical methods and a foundation for studying the stability and dynamics of magnetically levitated systems in precision measurements and fundamental physics experiments.

INTRODUCTION

The image charge method has long been used to solve boundary problems in electrostatics, particularly those concerning conductors and dielectrics [7]. More recently the image charge method has been used to approximate the potential of macroscopic magnets levitated in superconducting traps [8, 13]. These levitated systems boast high quality factors [5, 12] and force sensitivity, being currently at the forefront of technological applications and the exploration of fundamental physics problems such as probing the quantum nature of weak forces such as gravity [3, 5, 6, 9] as well as its current use in the search for dark matter [2, 4]. For levitated systems in general, finding the potential for a trapped magnetic dipole is often done numerically, utilising finite element methods to solve the field equations, however in some special cases it is possible to obtain analytical solutions [8, 13]. For macroscopic superconductors the London penetration depth can be assumed to be negligibly small and as such the superconductors can be assumed to be in an ideal Meissner state, a perfect diamagnet [11]. With this assumption, it is possible to obtain an analytic form of the potential of a dipole levitated above an infinite superconducting plate without ever having to solve the field equations [8, 13].

The purpose of this letter is to present an analytic form of the potential generated by a dipole trapped between two superconducting plates, which should serve as a good approximation of the trapping potential observed in real world experiments in fundamental physics, and furthermore provide a benchmark for numerical approximations of dipole potentials in more complicated geometries. We first present the derivation of the potential for a single dipole in the presence of one infinite superconducting plate. This solution is already present in the literature [13], however the calculations serve as instruction for the derivation of the potential between two plates, which is presented directly after. These results are then compared with the Finite Element Method, which is a commonly used numerical technique for solving PDE's with different boundary conditions.

DIPOLE ABOVE AN INFINITE SUPERCONDUCTING PLANE

To begin, consider a magnetic dipole in the presence of an infinite superconducting plate. As the superconductor can be treated as a perfect diamagnet, the magnetic induction inside of the plate is zero. Thus, we only need to consider the magnetic field outside of the plate. There is no free electric current outside of the plate, therefore we can introduce the magnetic scalar potential Φ_{I} such that the total magnetic field is $\mathbf{B} = -\mu_0 \nabla(\Phi_0 + \Phi_{\mathrm{I}})$ where Φ_0 is the scalar potential of the magnetic dipole and Φ_{I} is the scalar potential generated by the induced currents on the surface of the superconductor. Our dipole is situated near an infinite superconducting plate, defined at coordinate $z = a$. Noting that we have rotational symmetry of the geometry about the z-axis, we work in cylindrical coordinates (ρ, ϕ, z), and assume that the dipole is oriented in the (ρ, z)-plane. In this case, we may set the angular component $\phi = 0$, without loss of generality. The scalar potential at a point $\boldsymbol{r} = (\rho, z)$ for a dipole $\boldsymbol{\mu} = \mu(\cos\beta_0, \sin\beta_0)$ located at $\mathbf{r}_0 = (\rho_0, z_0)$ is given by

$$\Phi_0(\rho, z) = \frac{\boldsymbol{\mu} \cdot (\mathbf{r} - \mathbf{r}_0)}{4\pi |\mathbf{r} - \mathbf{r}_0|^3}. \tag{1}$$

In order to calculate the induced scalar potential Φ_{I}, we note that the Meissner effect implies the boundary condition on the induced magnetic field, that is $\mathbf{n} \cdot \mathbf{B}|_{z=a} = 0$, where $\mathbf{n}$ is the unit vector normal to the surface of the superconductor, which in this case is a unit vector in the z direction. To solve the boundary problem we place an image dipole located at $\mathbf{r}_1 = (z_1, \rho_1)$

$$\Phi(\rho, z) = \Phi_0(\rho, z) + \Phi_{\mathrm{I}}(\rho, z) = \frac{\boldsymbol{\mu} \cdot (\mathbf{r} - \mathbf{r}_0)}{4\pi |\mathbf{r} - \mathbf{r}_0|^3} + \frac{\boldsymbol{\mu} \cdot (\mathbf{r} - \mathbf{r}_1)}{4\pi |\mathbf{r} - \mathbf{r}_1|^3}. \tag{2}$$

Where we write explicitly:

$$\Phi_0(\rho, z) = \frac{\mu(z - z_0)\sin\beta_0 + \mu(\rho - \rho_0)\cos\beta_0}{4\pi((\rho - \rho_0)^2 + z^2 + z_0^2 - 2zz_0)^{3/2}}, \tag{3}$$

$$\Phi_{\mathrm{I}}(\rho, z) = \frac{\mu(z - z_1)\sin\beta_1 + \mu(\rho - \rho_1)\cos\beta_1}{4\pi((\rho - \rho_1)^2 + z^2 + z_1^2 - 2zz_1)^{3/2}}. \tag{4}$$

We note here that both Φ_0 and Φ_{I} satisfy the Laplace equation $\nabla^2 \Phi = 0$. The correct boundary condition requires that the normal component of the magnetic field

---

[*] francis.headley@uni-tuebingen.de

in the z direction to be zero at the surface of the plate. Taking the derivative with respect to z and evaluating at $z = a$ we find the boundary term:

$$\begin{aligned}\partial_z \Phi|_{z=a} =& \frac{\mu \sin\beta_0}{4\pi((\rho-\rho_0)^2 + (z_0-a)^2)^{3/2}} - 3(a-z_0)\left(\frac{\mu(a-z_0)\sin\beta_0 + \mu(\rho-\rho_0)\cos\beta_0}{4\pi((\rho-\rho_0)^2+(z_0-a)^2)^{5/2}}\right) \\ &+ \frac{\mu \sin\beta_1}{4\pi((\rho-\rho_1)^2 + (z_1-a)^2)^{3/2}} - 3(a-z_1)\left(\frac{\mu(a-z_1)\sin\beta_1 + \mu(\rho-\rho_1)\cos\beta_1}{4\pi((\rho-\rho_1)^2+(z_1-a)^2)^{5/2}}\right). \qquad (5)\end{aligned}$$

To set the term (5) to zero, we fix the z-coordinate of the image charge to be $z_1 = 2a - z_0,\ \ \rho_1 = \rho_0$, and its orientation $\beta_1 = -\beta_0$. This is tantamount to placing an oppositely oriented dipole of equal strength equidistant on the other side of the plate. The scalar potential of the image charge is thus:

$$\Phi_{\mathrm{I}}(\rho, z) = \frac{-\mu(z-(2a-z_0))\sin\beta_0 + \mu(\rho-\rho_0)\cos\beta_0}{4\pi((\rho-\rho_0)^2 + (z-(2a-z_0))^2)^{3/2}}. \qquad (6)$$

Because both Φ_0 and Φ_{I} satisfy Laplace's equation and the combined potential satisfies the boundary condition at $z = a$, the uniqueness theorem for Laplace's equation guarantees that this solution is unique [7]. We now set $\rho_0 = 0$ without loss of generality. The potential experienced by the dipole above the plate is calculated using [8]:

$$U(z_0, \beta_0) = -\frac{1}{2}\boldsymbol{\mu} \cdot \mathbf{B}_{\mathrm{I}}, \qquad (7)$$

where $\mathbf{B}_{\mathrm{I}} = -\mu_0 \boldsymbol{\nabla}\Phi_{\mathrm{I}}$. After some simple calculation, the potential experienced by the dipole levitated above an infinite superconducting plate may be expressed as:

$$U(z_0, \beta_0) = \frac{\mu_0 \mu^2}{64\pi(z_0 - a)^3}(1 + \sin^2\beta_0). \qquad (8)$$

As we have translational invariance along the ρ axis, we have set $\rho = 0$. Although this result is known in the literature [13], the derivation will serve as a basis for the calculations in the next section.

DIPOLE TRAPPED BETWEEN TWO SUPERCONDUCTING PLATES

To calculate the potential between two plates located at $z = a$ and $z = b$, we generalize the method from the single-plate case by accounting for an infinite series of image dipoles. This iterative process ensures that the boundary conditions are consistently satisfied on both superconducting surfaces. To begin, we introduce two image dipoles with potentials Φ_1 and Φ_{-1} at $z_1 = 2a - z_0$ and $z_{-1} = 2b - z_0$ respectively:

$$\Phi_0 = \frac{\mu(z-z_0)\sin\beta_0 + \mu\rho\cos\beta_0}{4\pi(\rho^2 + z^2 + z_0^2 - 2zz_0)^{3/2}}, \qquad (9)$$

$$\Phi_1 = \frac{-\mu(z-(2a-z_0))\sin\beta_1 + \mu\rho\cos\beta_1}{4\pi(\rho^2 + z^2 + (2a-z_0)^2 - 2z(2a-z_0))^{3/2}}, \qquad (10)$$

$$\Phi_{-1} = \frac{-\mu(z-(2b-z_0))\sin\beta_{-1} + \mu\rho\cos\beta_{-1}}{4\pi(\rho^2 + z^2 + (2b-z_0)^2 - 2z(2b-z_0))^{3/2}}. \qquad (11)$$

We introduce these dipoles with the same intention as in the previous section, to set the normal component of the B-field to zero at the plates $\partial_z\Phi|_{z=a/b} = 0$, however this fails immediately. To see this, we sum these terms $\Phi = \Phi_0 + \Phi_1 + \Phi_{-1}$ and take the derivative with respect to z.

Evaluating at the a-plate we find that the image dipole located at z_{-1} contributes a non-zero term, similarly the image dipole located at z_1 contributes a non-zero term on the b-plate. Explicitly:

$$\partial_z\Phi|_{z=a} = \frac{\mu\sin\beta_{-1}}{4\pi(\rho^2 + (a-(2b-z_0))^2)^{3/2}} - 3(a-(2b-z_0))\left(\frac{\mu(a-(2b-z_0))\sin\beta_{-1} + \mu\rho\cos\beta_{-1}}{4\pi(\rho^2 + (a-(2b-z_0))^2)^{5/2}}\right), \qquad (12)$$

$$\partial_z\Phi|_{z=b} = \frac{\mu\sin\beta_1}{4\pi(\rho^2 + (b-(2a-z_0))^2)^{3/2}} - 3(b-(2a-z_0))\left(\frac{\mu(b-(2a-z_0))\sin\beta_1 + \mu\rho\cos\beta_1}{4\pi(\rho^2 + (b-(2a-z_0))^2)^{5/2}}\right). \qquad (13)$$

To set these terms to zero we must modify our scalar potential to include two new image charges $\Phi \to \Phi' =$

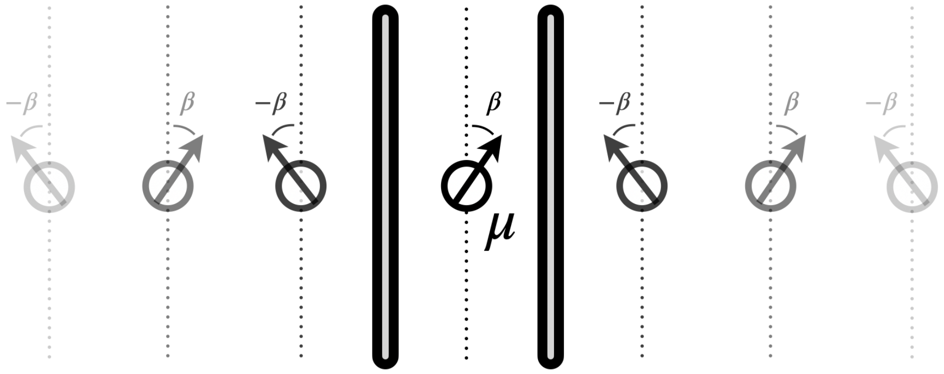

FIG. 1. Schematic representation of the infinite stack of image charges used to model the magnetic dipole μ trapped between two infinite superconducting plates. The image dipole method is used to represent the influence of the superconductors, creating an infinite series of mirror dipoles that enforce the boundary conditions.

$\Phi + \Phi_{-2} + \Phi_2$. To cancel the term (12) we add a dipole Φ_{-2} at $z_{-2} = 2a - 2b + z_0$ with orientation $\beta_{-2} = \beta_0$. Similarly to cancel the term (13) we introduce a fourth dipole Φ_2 at $z_2 = 2b - 2a + z_0$ with orientation $\beta_2 = \beta_0$. However, we are not out of the woods yet. Indeed, if we evaluate the derivative of our new scalar potential at both plates $\partial_z \Phi'|_{z=a/b}$ we find that the image charges we introduced to generate counter terms, will themselves require counter terms. It is easy to see how the charges introduced to generate counter terms require counter terms themselves. Luckily for us, we can do this forever. Repeating the process with our new potential Φ' we see that we must introduce two new dipoles at $z_{-3} = 4a - 2b - z_0$ and $z_3 = 4b - 2a - z_0$ with orientations $\beta_{-3} = \beta_3 = -\beta_0$. We repeat this process ad infinitum and enumerate it in a clever way. The 'counter-clockwise oriented' β_0 image dipoles Φ_{n+} and the 'clockwise-oriented' $-\beta_0$ image dipoles Φ_{n-} must be located at positions

$$\begin{aligned} z_{n+} &= 2n(b-a) + z_0, \\ z_{n-} &= 2n(b-a) + 2b - z_0, \qquad n \in \mathbb{Z}, \end{aligned} \tag{14}$$

respectively, such that all terms vanish on the plates. We note that the dipole z_{0+} is the original dipole located at z_0. Combining the above and summing over our infinite image charges, we arrive at the expression for the total scalar potential:

$$\Phi_{\text{tot}}(\rho, z) = \sum_{n\in\mathbb{Z}} \left(\frac{\mu(z - z_{n+})\sin\beta_0 + \mu\rho\cos\beta_0}{4\pi(\rho^2 + z^2 + z_{n+}^2 - 2zz_{n+})^{3/2}} + \frac{\mu(z_{n-} - z)\sin\beta_0 + \mu\rho\cos\beta_0}{4\pi(\rho^2 + z^2 + z_{n-}^2 - 2zz_{n-})^{3/2}} \right). \tag{15}$$

We can decompose the total scalar potential $\Phi_{\text{tot}} = \Phi_0 + \Phi_{\text{I}}$ where Φ_0 is the contribution from the dipole and $\Phi_{\text{I}} = \sum_{n\neq 0} \Phi_{n+} + \sum_n \Phi_{n-}$ is the contribution from the image charges. To calculate the potential experienced by the dipole, we calculate $U(z, \beta) = -\frac{1}{2}\boldsymbol{\mu} \cdot \boldsymbol{B}_{\text{I}}$, where $\boldsymbol{B}_{\text{I}} = -\mu_0 \boldsymbol{\nabla} \cdot \Phi_{\text{I}}$ [8]. Evaluating at $z = z_0$ and setting $\rho = 0$ we obtain the trapping potential of the dipole between two superconducting plates:

$$U = \frac{\mu_0 \mu^2}{8\pi} \left(\frac{\cos^2\beta_0 - 2\sin^2\beta_0}{4|b-a|^3} \zeta(3) + \sum_{n\in\mathbb{Z}} \frac{\sin^2\beta_0 + 1}{|z_0 - z_{n-}|^3} \right), \tag{16}$$

where $\zeta(n)$ is the Riemann zeta function. This is our main result. The expression (16) is divergent only if $z_0 = b$ or a, and is convergent otherwise. Furthermore, we note that in the limit $b \to \infty$, the two plate potential (16) converges to the single plate potential (8). Assuming that the infinite plates are located the same distance from the origin, that is to say at $z = b$ and $z = -b$, the resonance frequencies of the z and β modes may be calculated via the spring constants $\omega_z = \sqrt{k_z/m}$ and $\omega_\beta = \sqrt{k_\beta/I}$, where I is the moment of inertia of the magnet, which for a solid sphere magnet of radius r is $I = \frac{2}{5}mr^2$, m is the mass of the magnet, and k_z, k_β are the spring constants calculated via the second derivatives of (16):

$$k_z = \left.\frac{\partial^2 U}{\partial z_0^2}\right|_{z_0=0,\beta_0=0} \qquad k_\beta = \left.\frac{\partial^2 U}{\partial \beta_0^2}\right|_{z_0=0,\beta_0=0}. \tag{17}$$

as in [13]. Thus we find the resonance frequencies to be

$$\omega_z = \left.\sqrt{\frac{1}{m}\frac{\partial^2 U}{\partial z_0^2}}\right|_{z_0=0,\beta_0=0} \qquad \omega_\beta = \left.\sqrt{\frac{1}{I}\frac{\partial^2 U}{\partial \beta_0^2}}\right|_{z_0=0,\beta_0=0} \tag{18}$$

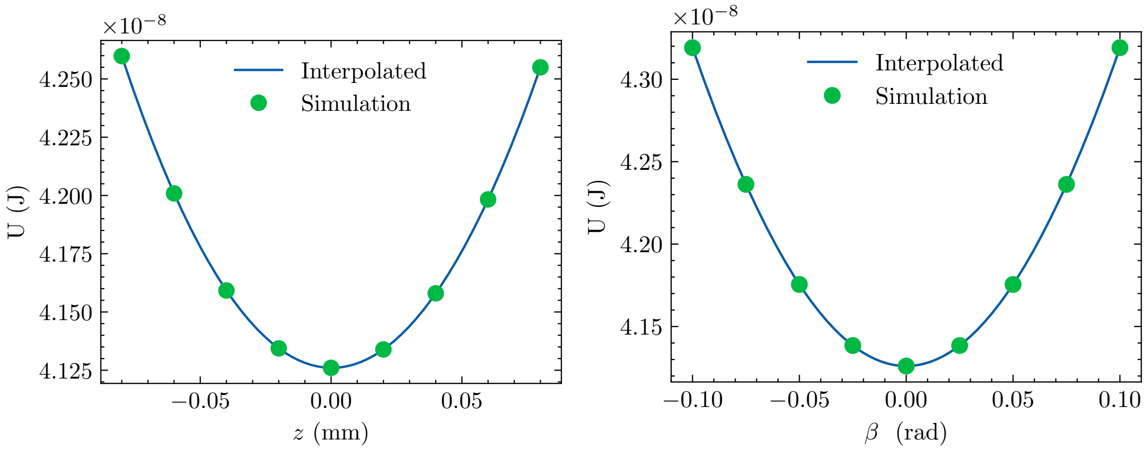

FIG. 2. Finite element method (FEM) simulations of a magnetic dipole trapped in a hollow superconducting cylinder near equilibrium. The left and right plots correspond to the z and β coordinates, respectively. The data, obtained by numerically solving Maxwell's equations using FEniCS, is fitted with quadratic functions to extract the trapping frequencies via Eq. (18).

The z_0 and β_0 mode frequencies may be extracted:

$$\omega_z = \sqrt{\frac{93}{256}\frac{\zeta(5)}{\pi}\frac{\mu_0\mu^2}{b^5 m}}, \qquad \omega_\beta = \sqrt{\frac{5}{64}\frac{\zeta(3)}{\pi}\frac{\mu_0\mu^2}{b^3 m r^2}}. \tag{19}$$

This formulation allows us to evaluate the magnetic potential at any point between the plates with arbitrary precision. Setting $z_0 = 0$ in (16), we find a simple form of the rotational potential:

$$U(\beta_0) = \frac{\mu_0\mu^2\zeta(3)}{128 b^3\pi}(5 - \cos(2\beta_0)) \tag{20}$$

which is a double well potential with minima located at $\beta_0 = 0,\ \pi$, which corresponds to both orientations of the magnet parallel to the plates.

NUMERICS

A useful point of comparison for Eq.(16) and Eq.(19) would be another commonly used method of extracting trapping frequencies for levitated particles. One example of such a method is Finite Element Method (FEM), which has been used to numerically approximate trapping frequencies for experiments involving levitated superconductors [10, 12]. FEM was selected due to its robustness in solving partial differential equations with boundary conditions, as encountered in the case of dipoles near superconducting planes. By discretizing the spatial domain of the problem into finite chunks, FEM allows for precise calculation of magnetic potential. Treating the levitated particle as a point dipole and assuming that the London penetration depth is negligibly small, the system is modelled using the following differential equations:

$$\begin{aligned} \nabla \times \boldsymbol{B}_\mathrm{I} &= 0 \qquad \forall x \in \Omega, \\ \boldsymbol{n}\cdot\boldsymbol{B}_\mathrm{I} &= -\boldsymbol{n}\cdot\boldsymbol{B}_0 \quad \forall x \in \partial\Omega, \end{aligned} \tag{21}$$

where $\mathbf{B}_0$ is the magnetic field generated by the dipole, $\mathbf{B}_\mathrm{I}$ is the induced magnetic field, $\boldsymbol{n}$ represents the unit vector normal to the surface of the superconductor, $\partial\Omega$ represents the surface of the superconductor and Ω the space outside of the superconductor, in our case the interior of a hollow superconducting cylinder where the dipole is located.

To solve this magnetostatics problem, we use FEniCS, a Python package for finite element method to solve PDE's [1]. The trapping frequencies are obtained by numerically solving Maxwell's equations (21) at points surrounding the dipole's equilibrium position, for both the z and β coordinates. At each point, the potential energy is calculated and fitted to a quadratic function, allowing the trapping frequencies to be determined via Eq. (18). With a Neodymium magnet of density $\rho = 7420$ kg m^{-3}, $\mu = 5.222 \times 10^{-5}$ A m^2, radius $r \approx 2.4 \times 10^{-4}$ m, a mass of $m = 4.3 \times 10^{-7}$ kg, and assuming the distance from the centre of the trap to the superconductor is $b = 1$ mm, the magnetic field induced by a point-like dipole was simulated. Although it is not possible to simulate two infinite plates using FEniCS, an approximation was implemented by using a wide cylinder of height $2b = 2$ mm and radius 25 mm. The results of this numerical procedure are plotted in Fig 2, and the frequencies extracted the interpolated data are displayed in Table I.

As we can see, for the calculation of the trapping frequency of the z-mode $f_z = \omega_z/2\pi$, the analytic result deviates only by approximately $\sim 0.5\%$ from the value calculated using FEM. For the β-mode trapping frequency

	Analytic	FEniCS	$\mathrm{Diff}_{\mathrm{rel}}$
f_z	155.545	154.673	0.56%
f_β	323.659	308.899	4.78%
U	4.096×10^{-8}	4.126×10^{-8}	0.73%

TABLE I. Results for the z frequency, β frequency, and potential energy, obtained using the analytic expression in Eq. (16) as well as the the finite element method (FEniCS).

the deviation from the FEM data is far larger, approximately $\sim 5\%$. One possible source of this deviation can be attributed to the additional geometry used when calculating the trapping frequencies using FEniCS, which in our case was a flattened cylinder. The additional circular walls of the trap, which are not considered in the analytic results, also contribute to the induced magnetic field and thus the trapping frequencies. This additional contribution to the field is more present in the β-mode than in the z-mode. It is also seen that increasing the radius of the simulated superconducting region systematically reduces the discrepancy between the numerical and analytical results, as the finite-size effects diminish and the boundary conditions more closely approximate the idealized analytic geometry.

CONCLUSION

We have derived the analytic potential experienced by a magnetic dipole positioned between two infinite parallel superconducting plates. By extending the image method commonly used in electrostatics, we formulated a systematic approach to construct the infinite series of image dipoles required to satisfy the boundary conditions imposed by the superconducting plates. This approach allowed us to obtain an exact analytical form of the trapping potential. Our results provide a useful benchmark for numerical simulations of levitated magnetic dipoles in superconducting environments. The derived potential serves as a step toward improving the accuracy of models used in high-precision experiments involving magnetic levitation, in particular those investigating weak forces such as gravity, applications to dark matter searches, as well as modelling of mesoscopic quantum tunnelling between orientations of the levitated magnet.

Acknowledgements – We thank Alessio Belenchia, Fabian Müller, Hendrik Ulbricht, Tim Fuchs, Chris Timberlake, Elliot Simcox, and Denis Uitenbroek for fruitful discussions. We further thank Daniel Braun, Alessio Belenchia and Sophie Heinrich for feedback on the draft of this paper, as well ast Giulio Gasbarri for help with the FEM code. We acknowledge the EU EIC Pathfinder project QuCoM (101046973).

[1] M. S. Alnaes, J. Blechta, J. Hake, A. Johansson, B. Kehlet, A. Logg, C. N. Richardson, J. Ring, M. E. Rognes, and G. N. Wells, *The FEniCS project version 1.5*, Archive of Numerical Software, 3 (2015).

[2] D. W. P. Amaral, D. G. Uitenbroek, T. H. Oosterkamp, and C. D. Tunnell, *First Search for Ultralight Dark Matter Using a Magnetically Levitated Particle*, (2024).

[3] S. Bose, I. Fuentes, A. A. Geraci, S. M. Khan, S. Qvarfort, M. Rademacher, M. Rashid, H. Ulbricht, and C. C. Wanjura, *Massive quantum systems as interfaces of quantum mechanics and gravity*, arXiv:2311.09218, (2023).

[4] D. Carney, S. Ghosh, G. Krnjaic, and J. M. Taylor, *Proposal for gravitational direct detection of dark matter*, Phys. Rev. D, 102 (2020), p. 072003.

[5] T. M. Fuchs, D. Uitenbroek, J. Plugge, N. van Halteren, A. Vinante, H. Ulbricht, and T. H. Oosterkamp, *Magnetic Zeppelin: Detection of gravitational drive in the Hz regime*, arXiv:2303.03545, (2023).

[6] C. Gonzalez-Ballestero, M. Aspelmeyer, L. Novotny, R. Quidant, and O. Romero-Isart, *Levitodynamics: Levitation and control of microscopic objects in vacuum*, Science, 374 (2021), p. eabg3027.

[7] J. D. Jackson, *Classical Electrodynamics*, Wiley, New York, 3rd ed., 1998.

[8] Q.-G. Lin, *Theoretical development of the image method for a general magnetic source in the presence of a superconducting sphere or a long superconducting cylinder*, Physical Review B, 74 (2006), p. 024510.

[9] J. Prat-Camps, C. Teo, C. Rusconi, W. Wieczorek, and O. Romero-Isart, *Ultrasensitive Inertial and Force Sensors with Diamagnetically Levitated Magnets*, Physical Review Applied, 8 (2017), p. 034002.

[10] C. Timberlake, G. Gasbarri, A. Vinante, A. Setter, and H. Ulbricht, *Acceleration sensing with magnetically levitated oscillators above a superconductor*, Applied Physics Letters, 115 (2019), p. 224101.

[11] M. Tinkham, *Introduction to Superconductivity*, McGraw-Hill, New York, 2nd ed., 1996.

[12] A. Vinante, P. Falferi, G. Gasbarri, A. Setter, C. Timberlake, and H. Ulbricht, *Ultralow mechanical damping with Meissner-levitated ferromagnetic microparticles*, Physical Review Applied, 13 (2020), p. 064027.

[13] A. Vinante, C. Timberlake, and H. Ulbricht, *Levitated Micromagnets in Superconducting Traps: A New Platform for Tabletop Fundamental Physics Experiments*, Entropy, 24 (2022), p. 1642.

Bibliography

[1] I. Newton, *Philosophiæ Naturalis Principia Mathematica.* Londini: Sumptibus Societatis, 1687.

[2] H. Cavendish, "XXI. Experiments to determine the density of the earth," *Philosophical Transactions of the Royal Society of London*, vol. 88, pp. 469–526, Jan. 1997.

[3] E. Tiesinga, P. Mohr, D. Newell, and B. Taylor, "Codata recommended values of the fundamental physical constants: 2018," *Reviews of Modern Physics*, vol. 93, p. 025010, 2021.

[4] G. T. Gillies, "The Newtonian gravitational constant: recent measurements and related studies," *Reports on Progress in Physics*, vol. 60, pp. 151–225, Feb. 1997. Number: 2.

[5] C. Rothleitner and S. Schlamminger, "Invited Review Article: Measurements of the Newtonian constant of gravitation, G," *Review of Scientific Instruments*, vol. 88, Nov. 2017. Publisher: AIP Publishing.

[6] B. S. DeWitt, "Quantum theory of gravity. i. the canonical theory," *Physical Review*, vol. 160, no. 5, pp. 1113–1148, 1967.

[7] F. DYSON, *IS A GRAVITON DETECTABLE?*, pp. 670–682.

[8] R. P. Feynman, "The role of gravitation in physics," in *Proceedings of the Conference on the Role of Gravitation in Physics* (C. W. Kilmister, ed.), (Chapel Hill, North Carolina), Wright Air Development Center, Air Research and Development Command, U.S. Air Force, 1957. Reprinted by WADC Technical Report 57-216, 1962.

[9] S. Bose, A. Mazumdar, G. W. Morley, H. Ulbricht, M. Toroš, M. Paternostro, A. Geraci, P. Barker, M. S. Kim, and G. Milburn, "A Spin Entanglement Witness for Quantum Gravity," *Physical Review Letters*, vol. 119, p. 240401, Dec. 2017. Number: 24 arXiv:1707.06050 [gr-qc, physics:hep-th, physics:quant-ph].

[10] C. Marletto and V. Vedral, "Gravitationally induced entanglement between two massive particles is sufficient evidence of quantum effects in gravity," *Phys. Rev. Lett.*, vol. 119, p. 240402, Dec 2017.

[11] A. Vinante, C. Timberlake, and H. Ulbricht, "Levitated Micromagnets in Superconducting Traps: A New Platform for Tabletop Fundamental Physics Experiments," *Entropy*, vol. 24, p. 1642, Nov. 2022. Number: 11.

[12] A. Vinante, P. Falferi, G. Gasbarri, A. Setter, C. Timberlake, and H. Ulbricht, "Ultralow mechanical damping with Meissner-levitated ferromagnetic microparticles," *Physical Review Applied*, vol. 13, p. 064027, June 2020. Number: 6 arXiv:1912.12252 [cond-mat, physics:physics, physics:quant-ph].

[13] T. M. Fuchs, D. Uitenbroek, J. Plugge, N. van Halteren, A. Vinante, H. Ulbricht, and T. H. Oosterkamp, "Magnetic Zeppelin: Detection of gravitational drive in the Hz regime," Mar. 2023. Issue: arXiv:2303.03545 arXiv:2303.03545 [cond-mat, physics:quant-ph].

[14] C. Timberlake, G. Gasbarri, A. Vinante, A. Setter, and H. Ulbricht, "Acceleration sensing with magnetically levitated oscillators above a superconductor," *Applied Physics Letters*, vol. 115, p. 224101, Nov. 2019. Number: 22.

[15] C. Timberlake, E. Simcox, and H. Ulbricht, "Linear cooling of a levitated micromagnetic cylinder by vibration," May 2024. arXiv:2310.03880 [quant-ph].

[16] J. Prat-Camps, C. Teo, C. Rusconi, W. Wieczorek, and O. Romero-Isart, "Ultrasensitive Inertial and Force Sensors with Diamagnetically Levitated Magnets," *Physical Review Applied*, vol. 8, p. 034002, Sept. 2017.

[17] C. Gonzalez-Ballestero, M. Aspelmeyer, L. Novotny, R. Quidant, and O. Romero-Isart, “Levitodynamics: Levitation and control of microscopic objects in vacuum,” *Science*, vol. 374, p. eabg3027, Oct. 2021. Number: 6564.

[18] S. Bose, I. Fuentes, A. A. Geraci, S. M. Khan, S. Qvarfort, M. Rademacher, M. Rashid, H. Ulbricht, and C. C. Wanjura, “Massive quantum systems as interfaces of quantum mechanics and gravity,” Nov. 2023. Issue: arXiv:2311.09218 arXiv:2311.09218 [quant-ph].

[19] K. Winkler, A. V. Zasedatelev, B. A. Stickler, U. Delić, A. Deutschmann-Olek, and M. Aspelmeyer, “Steady-state entanglement of interacting masses in free space through optimal feedback control,” Apr. 2025. arXiv:2408.07492 [quant-ph].

[20] A. N. Poddubny, K. Winkler, B. A. Stickler, U. Delić, M. Aspelmeyer, and A. V. Zasedatelev, “Nonequilibrium entanglement between levitated masses under optimal control,” Apr. 2025. arXiv:2408.06251 [quant-ph].

[21] T. Weiss, M. Roda-Llordes, E. Torrontegui, M. Aspelmeyer, and O. Romero-Isart, “Large Quantum Delocalization of a Levitated Nanoparticle using Optimal Control: Applications for Force Sensing and Entangling via Weak Forces,” July 2021. arXiv:2012.12260.

[22] H. Rudolph, U. Delić, M. Aspelmeyer, K. Hornberger, and B. A. Stickler, “Force-Gradient Sensing and Entanglement via Feedback Cooling of Interacting Nanoparticles,” *Physical Review Letters*, vol. 129, p. 193602, Nov. 2022.

[23] F. Cosco, J. S. Pedernales, and M. B. Plenio, “Enhanced force sensitivity and entanglement in periodically driven optomechanics,” *Physical Review A*, vol. 103, p. L061501, June 2021.

[24] F. Ahrens, W. Ji, D. Budker, C. Timberlake, H. Ulbricht, and A. Vinante, “Levitated Ferromagnetic Magnetometer with Energy Resolution Well Below ,” *Physical Review Letters*, vol. 134, p. 110801, Mar. 2025.

[25] T. Westphal, H. Hepach, J. Pfaff, and M. Aspelmeyer, “Measurement of Gravitational Coupling between Millimeter-Sized Masses,” Mar. 2021. arXiv:2009.09546 [gr-qc, physics:physics, physics:quant-ph].

[26] R. Kaltenbaek, G. Hechenblaikner, N. Kiesel, O. Romero-Isart, K. C. Schwab, U. Johann, and M. Aspelmeyer, “Macroscopic quantum resonators (MAQRO): Testing quantum and gravitational physics with massive mechanical resonators,” *Experimental Astronomy*, vol. 34, pp. 123–164, Oct. 2012. Number: 2.

[27] A. Belenchia, R. M. Wald, F. Giacomini, E. Castro-Ruiz, Brukner, and M. Aspelmeyer, “Quantum Superposition of Massive Objects and the Quantization of Gravity,” *Physical Review D*, vol. 98, p. 126009, Dec. 2018. Number: 12 arXiv:1807.07015 [gr-qc, physics:hep-th, physics:quant-ph].

[28] F. J. Headley, A. Belenchia, M. Paternostro, and D. Braun, “Quantum Metrology of Newton’s Constant with Levitated Mechanical Systems,” Mar. 2025. arXiv:2503.16215 [quant-ph].

[29] T. Krisnanda, G. Y. Tham, M. Paternostro, and T. Paterek, “Observable quantum entanglement due to gravity,” *npj Quantum Information*, vol. 6, p. 12, Jan. 2020.

[30] F. J. Headley, “Magnetic Dipole Trapping Potential between Infinite Superconducting Plates,” May 2025. arXiv:2504.18852 [cond-mat].

[31] D. Carney, S. Ghosh, G. Krnjaic, and J. M. Taylor, “Proposal for gravitational direct detection of dark matter,” *Physical Review D*, vol. 102, p. 072003, Oct. 2020. arXiv:1903.00492 [hep-ph].

[32] D. Carney, P. C. E. Stamp, and J. M. Taylor, “Tabletop experiments for quantum gravity: a user’s manual,” *Classical and Quantum Gravity*, vol. 36, p. 034001, Feb. 2019.

[33] M. Carlesso, S. Donadi, L. Ferialdi, M. Paternostro, H. Ulbricht, and A. Bassi, “Present status and future challenges of non-interferometric tests of collapse models,” *Nature Physics*, vol. 18, pp. 243–250, Mar. 2022. Number: 3.

[34] A. Bassi, A. Großardt, and H. Ulbricht, “Gravitational Decoherence,” *Classical and Quantum Gravity*, vol. 34, p. 193002, Oct. 2017. Number: 19 arXiv:1706.05677 [gr-qc, physics:quant-ph].

[35] C. D. Hoyle, D. J. Kapner, B. R. Heckel, E. G. Adelberger, J. H. Gundlach, U. Schmidt, and H. E. Swanson, “Submillimeter tests of the gravitational inverse-square law,” *Physical Review D*, vol. 70, p. 042004, Aug. 2004.

[36] D. J. Kapner, T. S. Cook, E. G. Adelberger, J. H. Gundlach, B. R. Heckel, C. D. Hoyle, and H. E. Swanson, “Tests of the Gravitational Inverse-Square Law below the Dark-Energy Length Scale,” *Physical Review Letters*, vol. 98, p. 021101, Jan. 2007. Number: 2.

[37] J. B. Fixler, G. T. Foster, J. M. McGuirk, and M. A. Kasevich, “Atom Interferometer Measurement of the Newtonian Constant of Gravity,” *Science*, vol. 315, pp. 74–77, Jan. 2007.

[38] H. Vahlbruch, M. Mehmet, N. Lastzka, B. Hage, S. Chelkowski, A. Franzen, S. Gossler, K. Danzmann, and R. Schnabel, “Observation of squeezed light with 10dB quantum noise reduction,” *Physical Review Letters*, vol. 100, p. 033602, Jan. 2008. arXiv:0706.1431 [quant-ph].

[39] H. Vahlbruch, M. Mehmet, K. Danzmann, and R. Schnabel, “Detection of 15 dB Squeezed States of Light and their Application for the Absolute Calibration of Photoelectric Quantum Efficiency,” *Physical Review Letters*, vol. 117, p. 110801, Sept. 2016.

[40] E. Köse, *High-resolution imaging with multi-parameter quantum metrology in passive remote sensing.* PhD thesis, Eberhard Karls Universität Tübingen, Mathematisch-Naturwissenschaftliche Fakultät, 2023. Dissertation zur Erlangung des Grades eines Dr. rer. nat.; mündliche Qualifikation: 22 Mai 2023.

[41] C. R. Rao, “Information and the accuracy attainable in the estimation of statistical parameters,” *Bull. Calcutta Math. Soc.*, vol. 37, pp. 81–91, 1945.

[42] H. Cramér, *Mathematical Methods of Statistics.* Princeton University Press, Princeton, NJ, 1946.

[43] C. W. Helstrom, "Quantum detection and estimation theory," *J. Stat. Phys.*, vol. 1, no. 2, pp. 231–252, 1969.

[44] A. S. Holevo, *Probabilistic and Statistical Aspect of Quantum Theory.* North-Holland, Amsterdam, 1982.

[45] S. L. Braunstein and C. M. Caves, "Statistical distance and the geometry of quantum states," *Physical Review Letters*, vol. 72, pp. 3439–3443, May 1994. Number: 22.

[46] M. G. Genoni, L. Lami, and A. Serafini, "Conditional and unconditional Gaussian quantum dynamics," *Contemporary Physics*, vol. 57, pp. 331–349, July 2016. Number: 3 arXiv:1607.02619 [quant-ph].

[47] A. Ferraro, S. Olivares, and M. G. A. Paris, "Gaussian states in continuous variable quantum information," Mar. 2005. Issue: arXiv:quant-ph/0503237 arXiv:quant-ph/0503237.

[48] O. Pinel, J. Fade, D. Braun, P. Jian, N. Treps, and C. Fabre, "Ultimate sensitivity of precision measurements with Gaussian quantum light : a multi-modal approach," *Physical Review A*, vol. 85, p. 010101, Jan. 2012. Number: 1 arXiv:1105.2644 [quant-ph].

[49] S. McMillen, M. Brunelli, M. Carlesso, A. Bassi, H. Ulbricht, M. G. A. Paris, and M. Paternostro, "Quantum-limited estimation of continuous spontaneous localization," *Physical Review A*, vol. 95, p. 012132, Jan. 2017. arXiv:1606.00070 [quant-ph].

[50] G. Adesso and F. Illuminati, "Gaussian measures of entanglement versus negativities: the ordering of two-mode Gaussian states," *Physical Review A*, vol. 72, p. 032334, Sept. 2005. Number: 3 arXiv:quant-ph/0506124.

[51] R. Graham, "Squeezing and Frequency Changes in Harmonic Oscillations," *Journal of Modern Optics*, vol. 34, pp. 873–879, June 1987.

[52] D. Yang, M. Ketkar, K. Audenaert, S. F. Huelga, and M. B. Plenio, "Quantum cramer-rao precision limit of noisy continuous sensing," *arXiv preprint arXiv:2504.12400*, 2025.

[53] D. Yang, S. F. Huelga, and M. B. Plenio, "Efficient information retrieval for sensing via continuous measurement," *Phys. Rev. X*, vol. 13, p. 031012, Jul 2023.

[54] S. Gammelmark and K. Mølmer, "Fisher information and the quantum cramér-rao sensitivity limit of continuous measurements," *Phys. Rev. Lett.*, vol. 112, p. 170401, Apr 2014.

[55] F. Albarelli, M. A. Rossi, D. Tamascelli, and M. G. Genoni, "Restoring heisenberg scaling in noisy quantum metrology by monitoring the environment," *Quantum*, vol. 2, p. 110, 2018.

[56] A. Serafini, *Quantum continuous variables: a primer of theoretical methods.* CRC press, 2023.

[57] M. G. Genoni, "Cramér-rao bound for time-continuous measurements in linear gaussian quantum systems," *Phys. Rev. A*, vol. 95, p. 012116, Jan 2017.

[58] A. Peres, "Separability Criterion for Density Matrices," *Physical Review Letters*, vol. 77, pp. 1413–1415, Aug. 1996.

[59] Q.-G. Lin, "Theoretical development of the image method for a general magnetic source in the presence of a superconducting sphere or a long superconducting cylinder," *Physical Review B*, vol. 74, p. 024510, July 2006.

[60] J. D. Jackson, *Classical Electrodynamics.* New York: Wiley, 3rd ed., 1998.

[61] M. S. Alnaes, J. Blechta, J. Hake, A. Johansson, B. Kehlet, A. Logg, C. N. Richardson, J. Ring, M. E. Rognes, and G. N. Wells, "The FEniCS project version 1.5," *Archive of Numerical Software*, vol. 3, 2015.

[62] O. C. Zienkiewicz, "Achievements and some unsolved problems of the finite element method," *International Journal for Numerical Methods in Engineering*, vol. 47, no. 1-3, pp. 9–28, 2000.

[63] C. Geuzaine and J.-F. Remacle, "Gmsh: A three-dimensional finite element mesh generator with built-in pre- and post-processing facilities," *International Journal for Numerical Methods in Engineering*, vol. 79, no. 11, pp. 1309–1331, 2009.

[64] F. Müller, E. Köse, A. J. Meixner, E. Schäffer, and D. Braun, "Pushing the Boundaries: Interferometric Mass Photometry at the Quantum Limit of Sensitivity," *arXiv:2410.19417*, 2024.

[65] J. Vovrosh, M. Rashid, D. Hempston, J. Bateman, M. Paternostro, and H. Ulbricht, "Parametric Feedback Cooling of Levitated Optomechanics in a Parabolic Mirror Trap," *Journal of the Optical Society of America B*, vol. 34, p. 1421, July 2017. arXiv:1603.02917 [physics, physics:quant-ph].

[66] M. G. Genoni, "Cramér-Rao bound for time-continuous measurements in linear Gaussian quantum systems," *Physical Review A*, vol. 95, p. 012116, Jan. 2017.

[67] M. A. Poggi, A. W. McFarland, J. S. Colton, and L. A. Bottomley, "A Method for Calculating the Spring Constant of Atomic Force Microscopy Cantilevers with a Nonrectangular Cross Section," *Analytical Chemistry*, vol. 77, pp. 1192–1195, Feb. 2005. Publisher: American Chemical Society.

[68] M. Aspelmeyer, T. J. Kippenberg, and F. Marquardt, "Cavity Optomechanics," *Reviews of Modern Physics*, vol. 86, pp. 1391–1452, Dec. 2014. Number: 4 arXiv:1303.0733 [cond-mat, physics:quant-ph].

[69] S. Butera, "Corrections to the Optomechanical Hamiltonian from Quadratic Fluctuations of a Moving Mirror," *Physical Review A*, vol. 111, p. 043524, Apr. 2025. arXiv:2412.07552 [quant-ph].

[70] K. Sala and T. Tufarelli, "Exploring corrections to the Optomechanical Hamiltonian," *Scientific Reports*, vol. 8, p. 9157, June 2018.

[71] P. A. Maia Neto, A. Lambrecht, and S. Reynaud, "Casimir energy between a plane and a sphere in electromagnetic vacuum," *Physical Review A*, vol. 78, p. 012115, July 2008.

[72] J. D. Teufel, T. Donner, D. Li, J. H. Harlow, M. S. Allman, K. Cicak, A. J. Sirois, J. D. Whittaker, K. W. Lehnert, and R. W. Simmonds, "Sideband Cooling Micromechanical Motion to the Quantum Ground State," Mar. 2011. arXiv:1103.2144.

[73] J. Chan, T. P. M. Alegre, A. H. Safavi-Naeini, J. T. Hill, A. Krause, S. Gröblacher, M. Aspelmeyer, and O. Painter, "Laser cooling of a nanomechanical oscillator into its quantum ground state," *Nature*, vol. 478, pp. 89–92, Oct. 2011.

[74] B. Abbott, "Observation of a kilogram-scale oscillator near its quantum ground state," *New Journal of Physics*, vol. 11, no. 7.

[75] A. Youssefi, S. Kono, M. Chegnizadeh, and T. J. Kippenberg, "A squeezed mechanical oscillator with millisecond quantum decoherence," *Nature Physics*, vol. 19, pp. 1697–1702, Nov. 2023.

[76] U. Delić, M. Reisenbauer, K. Dare, D. Grass, V. Vuletić, N. Kiesel, and M. Aspelmeyer, "Cooling of a levitated nanoparticle to the motional quantum ground state," *Science*, vol. 367, pp. 892–895, Feb. 2020.

[77] C. Wang, L. Banniard, K. Børkje, F. Massel, L. Mercier De Lépinay, and M. A. Sillanpää, "Ground-state cooling of a mechanical oscillator by a noisy environment," *Nature Communications*, vol. 15, p. 7395, Aug. 2024.